Numerical Simulation of Unsteady Flows of Physiological Relevance

Evegren, Philip

2009

Document Version:
Publisher's PDF, also known as Version of record

Numerical Simulation of Unsteady Flows of Physiological Relevance

Philip Evegren

October, 2009

Thesis for the Degree of Doctor of Philosophy in Engineering
ISBN 978-91-628-7952-5
ISSN 0282-1990
ISRN LUTMDN/TMHP–09/1067–SE

Division of Fluid Mechanics
Department of Energy Sciences
Faculty of Engineering
Lund University
Box 118
S-221 00 LUND
Sweden

Typeset in LaTeX
Printed by E-husets Tryckeri, October 2009

To my family

Scientific knowledge is a body of statements
of varying degrees of certainty – some most unsure,
some nearly sure, but non absolutely certain.
Richard P. Feynman

Abstract

Pulsatile flows in geometries of physiological relevance have been investigated. Atherosclerotic plaques are (initiated) near junctions and bifurcations in larger arteries. The flow in these regions is characterized by flow separation and unsteadiness, which indicates that local flow conditions contribute to atherogenesis.

Flows in curved and bifurcating pipes have been investigated over many years. However, details of dynamical patterns of pulsating flow, near wall effects, and differential diffusion effects are not well documented. The effect of wall elasticity on the flow has been assumed to be small but no quatification data exist.

There are same basic difficulties in studying physiological flow: The geometries have large inter-individual variations. The mechanical properties of the vessels are unknown. Equally, the boundary conditions (temporal and spatial distribution of the blood velocity) are not know. Additional difficulties arise due to measuring difficulties both in-vivo and in-vitro. The flow itself may be rather complex (time-dependent 3-D, transitional with locally strong effects of viscosity and unsteadiness, leading to variable phase lag between pressure gradient and the local flow).

The aim of this study is to enhance understanding of the time-dependent, physiologically relevant, flow field in bifurcations, and relate that to hypotheses of atherosclerotic disease. Additionally, an FSI-model has been developed with the purpose to model flow through elastic pipes, and to assess the effect of wall elasticity on the flow.

The investigations have shown clear patterns of wall shear stress (WSS) variations. Local regions of temporal and spatial variations of the WSS was found at sites usually referred to as risk-sites of atherosclerosis, but also at locations often referred to as "safe".

Some of the characteristics of the WSS are further related to changes in the secondary flow field. The secondary flow shows similar characteristics for an increased Reynolds number, although unsteady asymmetric patterns appear at peak flow, while a large Womersley number shows more simple secondary flow structures.

It is also shown that the effects of upstream geometrical variations on the flow field itself, are important mainly over one stage of arterial bifurcation. On the other hand, blood components (modeled as passive scalars with different values of

Schmidt numbers) do exhibit upstream effects over a longer range.An important finding is that Schmidt number effects may lead to redistribution of the different scalars. The variations in the concentrations of the scalars are of the same order as the local concentration themselves.

The FSI-model developed combines an Immersed Boundary-Finite Difference code with a shell model for the arterial wall. The shell model is solved on a (surface 2D) using a Finite Element Method (FEM) code. The structural solver is verified against an analytical expression for bending of a thin-walled pipe. The studies with respect to the importance of arterial wall elasticity on the flow, are not yet completed.

Acknowledgements

This project was partially supported by the Swedish Research Council (VR), which is much appreciated. Computational resources were, to a large extent, provided by LUNARC at Lund University.

The work was carried out at the Division of Fluid Mechanics, Department of Energy Sciences, Faculty of Engineering, Lund University, Sweden.

I would like to thank my supervisor Professor Laszlo Fuchs for giving me the opportunity to study this interesting field. I would also like to acknowledge my co-supervisor Dr. Johan Revstedt for taking time answering my questions and Dr. Robert Szasz for fixing my computers over and over again.

My gratitude also goes to all my colleagues (and former colleagues) at the Division of Fluid Mechanics, particularly Asim Jadoon, Changye Liu, Dragos Moroianu, Karl-Johan Nogenmyr, Lisa Prahl, Rixin Yu, Magnus Åberg, for both friendship and valuable discussions. I would also like to thank Dr. Christoffer Norberg for giving some input on the manuscript.

Last, but definitely not least, my thoughts and thanks go to my wife Stina (now you've got title, but no means...yet!), and my daughters Elina and Alicia for your love, support and patience.

Preface

This work concerns the pulsating flow in bifurcating pipe systems, and the modeling of fluid-structure interaction using an immersed boundary - finite difference method, for the fluid, and a finite element method for the solid. The following papers are included in the thesis:

I **Pulsatile Flow in Branching Arteries**, *Philip Evegren & Laszlo Fuchs*, The 3:rd IC-SCCE conference, Athens, 2008.

II **Wall Shear Stress Variations in a 90-degree Bifurcation in 3D Pulsating Flows**, *Philip Evegren, Laszlo Fuchs & Johan Revstedt*, On revision for publication in Medical Engineering & Physics.

III **On the Secondary Flow Through Bifurcating Pipes**, *Philip Evegren, Laszlo Fuchs & Johan Revstedt*, Submitted to Physics of Fluids.

IV **Pulsating Flow & Mass Transfer in an Asymmetric System of Bifurcations**, *Philip Evegren, Johan Revstedt & Laszlo Fuchs*, Submitted to Computers & Fluids.

Contents

Nomenclature

Latin Characters Upper Case

A	coefficient matrix of discretized equations $[-]$
	or amplitude of pressure gradient $[N/m^3]$ or area $[m^2]$
A_p	constant term in velocity distribution of Poiseuille flow $[1/(m \cdot s)]$
$\mathbf{B}$	matrix of differentiated shape functions
$\mathbf{C}$	global damping matrix $[kg/s]$
D	characteristic length scale (pipe diameter) $[m]$
$\mathbf{D}$	constitutive 2D matrix $[Pa]$
D_b	flexural rigidity of shell $[kgm^2/s^2]$
E^s	Young's modulus $[Pa]$
F	force term $[N]$
F_f	force term $[N]$
$F^s_{horizontal}$	horizontal force $[N]$
$F^s_{vertical}$	vertical force $[N]$
F^s_i	force acting on FEM-node $[N]$
G	pressure gradient $[N/m^3]$ or Gauss function
G'	non-dimensional pressure gradient $[-]$
H	discretized convective and diffusive terms
J_0	Bessel function of order zero $[-]$
J_1	Bessel function of first order and first kind $[-]$
$\mathbf{K}$	global stiffness matrix $[kg/s^2]$
L	pipe length or inlet length $[m]$ or Navier-Stokes differenial operator
$\mathbf{M}$	global mass matrix $[kg]$
M_{ij}	Moment around i:th direction and normal in j:th direction $[Nm]$
N_{faces}	number of faces of an element volume
N_{ij}	horizontal force in j:th direction and normal in i:th direction $[N]$
$\mathbf{N}$	matrix of shape functions
P	prolongation operator $[-]$ or radial load/length on cylinder $[kg/s^2]$
Q	volume flow $[m^3/s]$
R	pipe radius $[m]$ or restriction operator $[-]$ or residual
R_c	radius of curvature $[m]$
S	element surface area $[m^2]$
S_e	FEM-element surface area $[m^2]$
T	period $[s]$

U	characteristic velocity (peak inlet velocity or cross-sectional average) $[m/s]$
$\mathbf{U}$	vector of in-plane displacements $[m]$
V	volume $[m^3]$
V_e	FEM-element volume $[m^3]$
V_{ij}	vertical force in j:th direction and normal in i:th direction $[N]$
X	Cartesian x-component $[m]$
Y	Cartesian y-component $[m]$
Z	Cartesian z-component $[m]$

Latin Characters Lower Case

a	pipe radius $[m]$
a_{ij}	components of matrix A
b	vector of constants in discretized equation system
b_i^s	solid body force $[N/m^3]$
c_n	Fourier coefficients
$\mathbf{c}^{(\mathbf{e})\mathbf{i}}$	element damping matrix of part i ($i = 1$ in-plane and $i = 2$ bending) $[kg/s]$
d	residual vector
e_i	Cartesian base vector in direction i $[-]$
$\mathbf{e}_X$	Cartesian base vector in x-direction $[-]$
$\mathbf{e}_Y$	Cartesian base vector in y-direction $[-]$
$\mathbf{e}_Z$	Cartesian base vector in z-direction $[-]$
f	frequency $[1/s]$ or stress function or source term $[N/m^3]$ or general function
h	nearest distance between two FEM-nodes $[m]$
h_i	scale factor of component i $[-]$
$\mathbf{k}^{(\mathbf{e})\mathbf{i}}$	element stiffness matrix of part i ($i = 1$ in-plane and $i = 2$ bending) $[kg/s^2]$
$\mathbf{k}^{(\mathbf{e})\mathbf{tot}}$	total element stiffness matrix $[kg/s^2]$
$\mathbf{k}^{(\mathbf{e})}$	total element stiffness matrix in global coordinates
l	smallest length scale of the flow $[m]$
m	tangential vector $[-]$
$\mathbf{m}^{(\mathbf{e})\mathbf{i}}$	element mass matrix of part i ($i = 1$ in-plane and $i = 2$ bending) $[kg]$
n_i	normal in direction i $[-]$
p	pressure $[Pa]$
p^s	pressure load $[Pa]$
q_i	degree of freedom number i
$\mathbf{q}$	vector of degrees of freedom
r	radial length component $[m]$
$\mathbf{r}$	position vector $[m]$ or vector from cell centroid to face centroid $[m]$
s_i	new coordinate direction i $[m]$
t	time $[s]$
t^s	element thickness $[m]$
t_i	traction vector $[N/m^2]$

u	velocity in x-direction or axial velocity component in curvelinear coordinates $[m/s]$
$\mathbf{u^s_(e)i}$	element displacement vector of part i ($i = 1$ in-plane and $i = 2$ bending)
$\mathbf{u^s_{(e)total}}$	total element displacement vector
u_b	velocity at immersed boundary $[m/s]$
u_0	center line velocity $[m/s]$
u_0^s	center plane deformation in x-direction $[m]$
u_i	Cartesian velocity component in direction i $[m/s]$
u^s	deformation in x-direction $[m]$
u_i^s	deformation in x-direction at local node i $[m]$
v	velocity in y-direction or radial velocity component in curvelinear coordinates $[m/s]$
v^s	deformation in y-direction $[m]$
v_i^s	deformation in y-direction at local node i $[m]$
v_0^s	center plane deformation in y-direction $[m]$
w	velocity in z-direction or azimuthal velocity component in curvelinear coordinates $[m/s]$
w^s	deformation in z-direction $[m]$
w_i^s	deformation in z-direction at local node i $[m]$
x	length component in axial direction (curvelinear coordinates) or x-direction $[m]$
x_i	Cartesian length component in direction i $[m]$
y	y-coordinate $[m]$

Non-dimensional Numbers

$\alpha = \frac{D}{2}\sqrt{\frac{\omega}{\nu}}$	Womersley number
$De = \frac{1}{\sqrt{2}}\sqrt{K}$	Dean number
$K = \frac{2aRe^2}{R_c}$	Dean number (other form)
$Kn = \frac{\lambda}{l}$	Knudsen number
$Re = \frac{UD}{\nu}$	Reynolds number
$St_f = \frac{fD}{U}$	Strouhal number
$St = a/\delta = \alpha/\sqrt{2}$	Stokes number

Greek Characters

$\alpha_{1,\ldots,9}$	polynomial coefficients
β	ratio of through flow over oscillatory flow $[-]$ or relaxation term or constant
δ	curvature ratio $[-]$ or Stokes layer thickness $[m]$
$\delta(x_i)$	Dirac delta distribution (in 3D)
δ_{ij}	Kronecker delta $[-]$
δ_1	boundary layer thickness associated with transient acceleration $[m]$
δ_2	boundary layer thickness associated with convective acceleration $[m]$
Δ_i	gradient in discretized form
ϵ_{ij}	strain rate tensor $[1/s]$
ϵ^s_{ij}	infinitesimal strain tensor $[-]$
$\boldsymbol{\epsilon^s}$	2D strain vector $[-]$
η	local y-coordinate $[m]$
Γ^f	boundary of fluid domain towards solid domain
Γ^s	boundary of solid domain towards fluid domain
ϕ	general parameter or angle of curvature in curvelinear coordinates $[-]$
λ	mean free path between molecules $[m]$ or bulk viscosity $[kg/(m \cdot s)]$
λ_{tot}	total transformation matrix between local- and global-coordinate systems
λ^s	Lame's (first) constant $[N/m^2]$
$\boldsymbol{\Lambda}$	matrix of element base functions
μ	dynamic viscosity $[kg/(m \cdot s)]$
μ^s_l	Lame's (second) constant $[N/m^2]$
μ^s	damping coefficient $[kg/\left(s \cdot m^3\right)]$
ν	kinematic viscosity $[m^2/s]$
ν^s	Poisson ratio $[-]$
ω_i	angular frequency $[1/s]$
Ω^f	fluid domain
Ω^s	solid domain
ψ	correction vector
ρ	fluid density $[kg/m^3]$
ρ^s	solid density $[kg/m^3]$
σ	standard deviation
$\boldsymbol{\sigma^s}$	2D stress vector
σ_{ij}	stress tensor $[N/m^2]$
$\tau_{\theta r}$	WSS-component in azimuthal direction (cylinder coordinates) $[N/m^2]$
τ_{xr}	WSS-component in axial direction (cylinder coordinates) $[N/m^2]$
θ	azimuthal direction (curvelinear coordinates) $[-]$
θ_{xi}	rotation angle around local x-axis at local node i $[-]$
θ_{yi}	rotation angle around local y-axis at local node i $[-]$
θ_{zi}	rotation angle around local z-axis at local node i $[-]$
$\boldsymbol{\Theta}$	vector of polynomial coefficients
ξ	local x-coordinate $[m]$
$\boldsymbol{\Upsilon}$	matrix of base-functions for one node
ζ	r/a $[-]$ or local z-coordinate $[m]$

Super-scripts

c	coarser grid level
$\mathbf{c}$	vector of arbitrary test function coefficients
f	parameter taken from element face or referring to fluid
k	previous iteration level
$k+1$	present iteration level
n	variable at previous time step
s	referring to parameter of solid
$*$	solution after predictor step or non-dimensional number
$**$	solution after corrector step
$'$	quantity of small magnitude

Sub-scripts

ave	average
b	referring to bending part
e	exact solution
$elem$	related to mesh element
ho	high order discretization terms
lo	low order discretization terms
loc	local parameter
nb	neighboring cells
p	cell center value
$plasma$	referring to blood plasma
$n+1$	next point in time

Abbreviations

A-V	Atrio-Ventricular
ALE	Arbitrary Lagrangian-Eulerian
CFD	Computational Fluid Dynamics
CFL	Courant-Friedrichs-Lewy
FAS	Full Approximation Storage
FD	Finite Difference
FEM	Finite Element Method
FFT	Fast Fourier Transform
FSI	Fluid-Structure Interaction
FVM	Finite Volume Method
LDL	Low Density Lipoprotein
HDL	High Density Lipoprotein
IB	Immersed Boundary
PDE	Partial Differential Equation
PDF	Probability Density Function
RHS	Right Hand Side
RMS	Root Mean Square
WSS	Wall Shear Stress

List of Figures

Chapter 1

Introduction

1.1 Context & Motivation

Biomechanics is a growing field of research with strong inter-disciplinary components. Tissue properties of bone, cartilage and soft tissue are analysed with different mathematical models, which often include nonlinear- and visco-elastic effects (c.f. [20, 89, 216]). Bio-fluid mechanics include flow past biological bodies, i.e. aerodynamics of birds or hydrodynamics of fish, and internal flows such as blood flow or airflow in the lungs [32, 49]. In the case of airflow in the lungs, modeling can be used for estimation of drug distribution [219]. Some applications of blood flow simulations include the investigation of the flow past prosthetic heart valves [210], flow through ventricular assisting devices [215], study of the flow field and distribution of wall shear stress (WSS) near bifurcations [50–52], and the study of fluid structure-interaction (FSI) between the blood and the flexible blood vessel wall [26, 137].

One has to emphasize that biological systems exhibit considerable individual variations, which makes the study meaningful (and quantifiable) only in terms of statistical values (averages, RMS, PDF, etc). The inter-individual variation makes it difficult to identify and quantify particular physiological processes that lead to a pathological state. For this reason one may use theoretical and experimental tools to analyse the importance of a hypothetical process. In that sense, the simplifications made in the modeling (as is also done here) are still adequate to qualitatively study certain physiological processes.

This work presents numerical simulations of flow through systems of bifurcating vessels, as well as an FSI-model developed with the purpose of modeling the interaction between the flow through a vessel and its elastic wall. The overall objective of the work presented is to investigate the flow field and its relation to different parameters that are considered to be relevant for blood flow in arteries. In such environments the relevant parameters include compliance effects, effects of other geometrical variations, and flow parameter effects such as the Reynolds-

and Womersley numbers. The flow behavior and in particular the characteristics of the WSS are discussed in terms of their effect on atherogenesis (i.e. the patho-physiological process leading to atherosclerosis).

Cardiovascular diseases are the major cause of death (over 50%) in the western world today, which can be largely attributed to atherosclerosis itself or closely related diseases [114]. Atherosclerosis is a dynamic disease and it is the major contributor to the pathogenesis of myocardial and cerebral infarction [133]. The process of development of an atherosclerotic plaque is not fully understood. However, it has been found that it, at some early stage, involves the accumulation of lipoproteins in the intima (the most inner layer of the artery). One has also observed that an inflammatory process is present. This observation is based on the presence of components of the immune system near the lesion (monocytes and T-lymphocytes that take up the lipid containing lipo-protein macro-molecules). The morphological changes in the wall of the artery lead to a fibro-fatty plaque on the vessel wall, and when the disease process has continued long enough it leads to the obstruction of the lumen [114, 133]. The structure of the plaque is a fatty core covered by a fibrous cap which eventually may burst and thereby initiate thrombosis [39, 208]. The thrombus may then be transported (becoming an embolus) into smaller blood vessels where it may stop the blood flow altogether. Thereby hindering oxygen rich blood from reaching downstream tissue. The result is hypoxia (lack of oxygen) or in the worst case necrosis (i.e. cell and tissue death). The disease usually starts in early life and fatty streaks, which are found in the initial stage, have been detected even during fetal development [31]. A more detailed description of the disease process will be given in a subsequent chapter.

Charakida et al. [31] identify hypercholesterolemia, diabetes, hypertension, smoking, age and gender as conventional risk factors for atherosclerosis. However, conventional risk factors correlate with less than 50 % of the incidences of atherosclerotic disease. Other risk factors have also been suggested; for example, inflammation or infection as initiator, obesity, genetic factors and nutrition. Also, psychological stress may influence the development of atherosclerosis [146]. The large number of hypotheses is a good indicator for the lack of precise knowledge and understanding of the underlying processes.

The plaques (especially early ones) are usually found at specific locations *locus minori*. Such locations are found only in larger arteries near bifurcations and in significant curvature in the arthery [8, 121, 133, 173, 205]. The well defined localization of pathological manifestation of the disease, is the foundation of the theory that local flow conditions are very important parameters for its development. Atherosclerosis is thus a multi-factorial disease, probably affected by both biochemistry and complex nonlinear biomechanics. The complexities of flow in biological tissues make approximations necessary. Such simplifications are often related to the properties of the blood and the tissue composing the arterial tree. In spite of the simplifications it is believed that it is possible to enhance the

understanding of atherogenesis and its possible relation to the surrounding flow field.

1.2 Objectives & Achievements

In this work numerical simulations of the unsteady flow (of blood) in 3D systems of asymmetric bifurcations have been performed. Also, an FSI-modeling approach has been developed with the aim of investigating flow in a deforming vessel.

The main objectives of the simulations have been as follows:

- To enhance the understanding of the pulsatile flow properties in bifurcating pipes.
- To investigate the effects of certain parameters (such as inflow conditions, pulsation rate, geometrical properties) on the flow field.
- To develop an FSI-modeling approach and to apply the model for assessing the effect of a deformable wall on the flow.
- Relate simulation findings to current hypotheses of atherogenesis.

The achievements included in this thesis are:

- Detailed investigation of magnitude and direction of WSS at common sites of atherosclerosis, including comparison with results found in literature.
- Investigation of the characteristics of temporal- and spatial-variations of the WSS.
- Investigation of dynamics of the secondary flow field.
- Determination of the effects of Reynolds- and Womersley-numbers on the velocity field (including secondary vortices) and wall shear stresses.
- Investigation of inlet boundary condition effects on the flow field and on the distribution of a passive scalar.
- Development of an FSI-solver, coupling a Finite Difference-Immersed Boundary approach for the fluid, with a Finite Element Method approach for the solid.

1.3 Outline

In the following, a brief review of the anatomy and physiology of the artery system is given. Thereafter, a short introduction to a biological perspective on the process of atherosclerosis is followed by a section where previously found relations between atherosclerosis and fluid flow is given. After that a review of fluid mechanical aspects relevant for the typical flows considered is included, followed by a description of computational tools used herein. At the end, a summary of results achieved and proposals for future work are followed by the papers, which this thesis is based upon.

Chapter 2

The Cardiovascular System & Atherosclerosis

This chapter describes the components of the cardiovascular system, which is the major flow environment of this work. It also describes theories and suggestions that try to explain and describe the processes that lead to atherosclerosis. The emphasis is naturally on the fluid mechanical aspects of these theories. The content of the following section is mainly taken from Levick [109], Pedley [140] and Tortora and Derrickson [189].

2.1 The Heart & Blood Vessels

The cardiovascular system has several important functions critical and/or essential for life. These include transport of oxygen, nutrients, carbon dioxide and other wastes, immune response, pH- and heat-regulation. All these functions involve blood flow through the arteries and the heart, which is also the device that provides the mechanical energy to the system.

The heart is a muscle that is located in the chest, between the parts of the lung, and between the sternum and the vertebral column. It is of roughly coned shape with the apex to the left, downwards, and its average weight is about 250 g and 300 g for female and male adults, respectively. About two thirds of the mass of the heart lies to the left of the centreline of the body.

The heart contains four chambers, two atria and two ventricles; a sketch of the heart is found in Figure 2.2. The right atrium receives blood from two major veins (i.e. *v. cava superior* and *inferior*) and it is separated from the left atrium by the inter-atrial septum and from the ventricle by the tricuspid valve (which consists of three cusps). The right ventricle is the origin of the pulmonary artery which is separated from the ventricle by the pulmonary valve. The two ventriculi are separated from each other by a thick wall of muscle, i.e. the inter-ventricular septum. The left atrium receives oxygenated blood from the lungs through the

four pulmonary veins. It is separated from the left ventricle by the bicuspid or mitral valve (which has two cusps). The blood flow from the left ventricle is regulated by the aortic valve. This valve opens and closes passively, depending on the flow conditions through it.

Blood flows through the systemic- and pulmonary-veins into the right and the left atria, respectively. The atria are being more or less continuously filled and when the pressures exceed the pressures in the ventricles, the tricuspid- and the mitral-valves open and thereby letting the blood into the ventricles. The filling period of the ventricles of the heart is called diastole. When the ventricles become full of blood the atria contract and eject its content into the ventricles. In the same time as the myocardium (heart muscle) contracts, the atrio-ventricular (A–V) plane moves towards the apex and the tricuspid- and the mitral valves are closed. A volume reduction will result in a quick increase in ventricular pressure, which leads to the opening of the aortic- and the pulmonary-valves. This is followed by a quick ejection of the blood; the ejection phase is called systole. As the ventricles relax, blood starts to re-circulate in the ascending aorta and in the pulmonary artery.

As the pressure in the left ventricle decreases below the aortic pressure, the flow near the walls changes direction immediately, whereas at the central parts of the aorta this happens with some delay. The closure of the aortic valve is quick, yet there is always some back-flow. As part of the sclerotic process, one observes also reduced elasticity of the blades of the aortic valve which leads to increased back-flow. Once the valve calcifies, the valve may be incompetent or leaky, and back-flow may be present throughout diastole. Often there is also a reduction of the open area of the valve, which leads to larger pressure drop during systole, and which in turn implies larger load on the heart.

A difference between the right- and the left-ventricles, is that the pressure that is needed to eject blood through the aortic valve, on the left side, is much larger than for the pulmonary valve, on the right side. This is due to the larger resistance and higher pressure of the systemic system, also resulting in a thicker myocardium on the left side of the heart. The diastolic pressure in the pulmonary artery is normally about 20 mmHg and in the aorta about 80 mmHg. The pressure in the left ventricle rises to about 120 mmHg, while in the pulmonary system it rises to about 25–30 mmHg during systole.

The ventricles eject about 70 ml blood, leaving about 60 ml left behind. Ventricular systole lasts about 0.3 s, and the time it takes for the valves to open is about 10 ms, according to Rosenfeld et al. [120].

The blood vessels consist of several different layers with different characteristics. The arteries[1] are the blood vessels distributing blood from the heart to the other organs[2], and are subject to high and oscillatory pressure. The veins are

[1]Greek: ar = air, ter = to carry, were first believed to carry air [71, 189].

[2]The discovery of the circulation system is traditionally referred to William Harvey [82],

the vessels distributing the blood back to the heart, and are subject to lower and almost constant pressure.

More specifically, arteries are, in adults, of radius in the range of about 1 cm to the order of 0.1 mm, where the aorta is the largest one carrying the blood from the left ventricle of the heart. The ascending aorta is roughly straight for about 3 cm and then it turns almost 180^0, in a 3D way out of plane, continuing down through the chest and abdomen. It has multiple branches that supply blood to the different organs before it bifurcates (in the pelvis) into the two iliac arteries [140, 189]. Most branches and bifurcations are asymmetric and vary when it comes to branching angle. Usually the angles are closer to 90^0, than 0^0 or 180^0, for aortic bifurcations, while they more commonly are smaller in smaller vessels [140]. Downstream of the aorta the total cross-sectional area of all arteries increase drastically, which implies smaller flow rate.

The vessel wall of arteries can be divided into three layers, *tunica interna* or *tunica intima*, *tunica media* and *tunica externa* (Figure 2.1). The tunica intima is the innermost layer closest to the blood in the lumen, and it consists of a layer of simple squamous epithelium called endothelium, a basement membrane and a layer of elastic tissue called internal elastic lamina. The endothelium is lining the innermost vessel wall of all blood vessels and is usually the only cell layer in direct contact with the blood. The tunica media is the thickest of the three layers and has next to the internal elastic lamina a layer of elastic fibres and smooth muscle fibres stretching around the vessel wall. It also has a layer of elastic tissue covering the smooth muscles called external elastic lamina. The tunica media is composed in a large proportion of the very elastic extracellular protein elastin and in a smaller proportion of the strong but much stiffer extracellular protein collagen [109]. The outermost layer of the vessel wall, the tunica externa consists mainly of elastic- and collagen-fibres. The different components give the vessel wall its non-trivial material characteristics [89].

The smooth muscle cells can be stimulated to contract, which reduces the vessel radius (vasoconstriction). The basic tension in the artery wall can not only increase, but it can be reduced by relaxing the smooth muscles (vasodilation). For steady flow conditions (laminar in a straight pipe) the flow can be related to the vessel radius to the power of four, which explains the efficiency of the constrictor/dilator effect as blood distributor. The largest arteries (> 1 cm in diameter) are called elastic arteries due to their high proportion of elastic fibres in the tunica media. They have the function of stretching during systole, due to the pressure pulse caused by the heart's ejection of blood. The expanded wall is relaxed during diastole and the (elastic) potential energy of the wall is transformed into kinetic energy (of the blood), giving a more continuous flow in the arterial system, in contrast to the heart. It has also been shown that the inner vessel wall of arteries move in the longitudinal direction. Measurements by

who realised in 1628 that the blood was circulating.

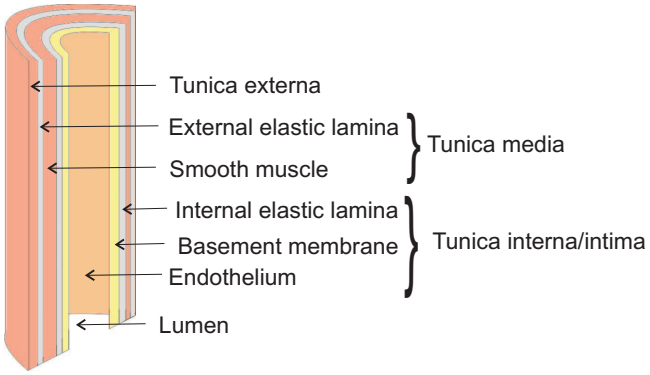

Figure 2.1: Sketch of the different layers of an arterial wall; after Tortora and Derrickson [189].

Cinthio et al. [35] on the common carotid artery show that the movement in the longitudinal direction is of the same order as in the radial direction.

The medium sized arteries, 0.1–10 mm, are usually called muscular arteries because of their relatively high content of smooth muscle fibers in comparison to the elastic arteries. The amount of smooth muscle fibers give them the properties of being constrictors and dilators, which enables a functional distribution of the blood to different parts of the body. The small arteries or arterioles (10–100 μm) are the vessels just upstream of the capillaries. The larger arterioles are similar in composition to the muscular arteries, also being able to constrict and dilate. Arterioles close to the capillaries have a wall which consists of a layer of endothelial cells over which a few smooth muscle fibers are scattered.

The capillaries are connecting the arterioles to the vein system, they have a diameter of 4–10 μm. The body contains a huge amount of capillaries in order to distribute oxygen and nutrients to practically all cells of the body; the organs that are more oxygen and nutrients demanding naturally contains more capillaries. The arterioles, capillaries and venules are usually referred to as the micro-circulation. The capillary wall only consists of the endothelial layer and the basement membrane which make them suitable for their task to exchange oxygen, nutrients and wastes with neighboring cells through the interstitial fluid. The short distance between the cells and the capillaries make diffusion vary rapid [109].

Several capillaries unite forming the venules (10–100 μm) and similarly to the arterioles the smallest venules are composed of the endothelium and a tunica media, composed of a few scattered smooth muscle cells. The larger venules also consist of the tunica externa but without the elastic laminae. The veins (> 0.1 mm) connects the venules to the atria of the heart. The thin walls of the veins consist of the same layers as the arteries, although the two innermost layers are much thinner and contain only few smooth muscle cells and elastic fibers. The

tunica externa is the thickest layer of the veins. They are still distensible but are not made for resisting any higher pressure. The veins may even collapse completely at low blood pressures.

2.2 Properties of Blood

The cardiovascular system consists of three parts that are dependent on each other; those are the heart, the blood vessels and the blood itself. The blood which is a liquid connective tissue has several different functions; transportation of oxygen, carbon dioxide, nutrients and hormones to and from the cells of the body. It also helps regulating pH and temperature, and act as part of the immune response system through phagocytosis and with help of different proteins [189]. The blood has a pH between 7.35–7.45. An adult male has a blood volume of about 5–6 liters, while an adult female has about 4–5 liters, corresponding to about 8 % of the total body weight.

The blood consists of the blood plasma (55 %), which is the extracellular liquid with dissolved and colloidal substances and the formed elements (45 %), cells. The plasma contains to 91.5 % water and 8.5 % solutes of which 7 % are proteins. The proteins are mainly albumins, and other proteins such as Low- and High-Density Lipoproteins (LDL, HDL), immuno-globulins, and fibrinogens. These proteins are responsible to different functions such as carriers of hormones, Ca and fatty acids, immunresponse and blood clotting. Other solutes are electrolytes, nutrients, gases, enzymes, hormones and waste products. The formed elements are divided into red blood cells, white blood cells and platelets, of which 99 % are red blood cells. The volume occupied by red blood cells divided by the total blood volume, expressed in percent, is referred to as hematocrit. The hematocrit for an adult male ranges between 40–54 % and for a female between 38–46 %. The formed elements last over a period (depending on the type of cells) and are continually replaced by new cells mainly produced in the red bone marrow.

The red blood cells, or erythrocytes, are cells without nucleus or organelles containing the oxygen-carrying protein hemoglobin that gives the blood its red color. The cells are shaped like biconcave disks with a diameter of 7–8 μm, a thickness of about 1 μm in the centre and 2–3 μm along the edge [140], and their strong and flexible plasma membrane give them the ability to deform and squeeze through narrow capillaries. The shape also gives them large surface area, which is advantageous for gas diffusion. The blood contains about 5.4 million red blood cells per μl for males, and about 4.8 million for females. One red blood cell contains about 280 million hemoglobin molecules, which each can bind four oxygen molecules [189].

White blood cells, or leukocytes, are of several different types, which all have nuclei but no hemoglobin; the white blood cells are grouped according to their morphology and include neutrophils, eosinophils, basophils, lymphocytes and

monocytes. The sizes range between 6–20 μm in diameter and they are also deformable. There are much fewer white blood cells than red blood cells, only about 5000–10000 cells per μl. Each white blood cell act in different ways as part of the body's defence system against infectious microbes, cancers etc. [189].

Platelets, or thrombocytes, are the last kind of formed elements. A platelet is a disk shaped cell without nucleus, with a diameter ranging between 2–4 μm. Each μl of blood contains about 150000–400000 platelets. A function of platelets is to help stop blood losses from a wound by forming a platelet plug, and by inducing coagulation (blood clotting).

2.3 Atherosclerosis

Cardiovascular related diseases are responsible for more than 50 % of all deaths, including heart-attack and stroke, in the western world. Non-congenital etiology can be attributed mainly to atherosclerosis[3] [133]. In Sweden about two thirds of all days of treatment at medical clinics are related to cardiovascular diagnosis [114].

Atherosclerosis is primarily an intimal disease of large and medium-sized arteries. It is characterized by fibro-fatty plaques at certain local positions of the vessel wall, often obstructing the lumen (stenosis), accompanied by inflammation and fibrosis (scar tissue formation). The disease usually starts in early life and fatty streaks, which are initially found before atherosclerosis, have been detected even during fetal development [31, 205].

Charakida et al. [31] identify hypercholesterolemia, diabetes, hypertension, smoking, age and gender as conventional risk factors for atherosclerosis, but conventional risk factors are correlated to less than 50 % of the incidences. Other discussed more novel risk factors are, inflammation/infection, obesity, genetic factors and nutrition. Also psychological stress may influence the development of atherosclerosis [146]. It seems difficult to correlate complicated plaques with symptoms [125].

Atherosclerosis is thus an evolving process, a dynamic multi-factorial disease, and a comprehensive analysis would probably demand both biochemistry and nonlinear biomechanics, in order to fully understand it.

The process of development of the plaque is not fully understood in all its elements, the last years much attention has been given to the inflammation process in atherosclerosis, which seems to be a critical factor [133]. For natural reasons it is difficult to study the atherogenic process in humans, however, it has been and is studied in animals [114].

The early change in the arterial wall is composed by accumulation of lipoproteins in the intima. Eventually an inflammatory process is initiated, most prob-

[3] *sclerosis* = hardening of tissues with loss of elasticity, i.e. hardening of the arterial wall [189].

ably due to oxidized LDL (low density lipoproteins), resulting in endothelial expression of adhesion molecules and induced chemo-attractant molecules. Leukocytes, mainly monocytes and T-lymphocytes, are entering the vessel wall and the monocytes are transformed into macrophages [160]. The macrophages take up the lipid containing molecules and become, so called "foam cells"; "fatty streaks" can then be observed. Smooth muscle cells start to migrate from the media to the intima and proliferate (cell reproduction) [133]. An extracellular matrix is build up and the fatty streaks evolve into fatty-fibrous lesions. This is followed by fibrosis, sometimes along with cell death, resulting in a relatively cell-free thin fibrous capsule surrounding a lipid-rich core. The cell death is associated with toxic substances derived from oxidized LDL, resulting in that the LDL up-taking macrophages are affected initially. In addition to cell death, for instance, collagen destructive macrophages have been found in the fibrous cap, which also promotes plaque rupture [114, 133]. When rupture of the cap takes place, the core of the plaque is exposed, leading to platelet adhesion and activation, and thus to thrombus formation, which may lead to local (or remote embolus and thereby) ischemia or infarction [39, 208]. Gertz et al. [73], Richardsson et al. [157] and Falk et al. [54] describe different reasons that may be behind plaque rupture.

Other authors describing the process of atherogenesis are, for instance, Stary et al. [174] and Gotto et al. [1] for the different stages in atherosclerosis, Nielsen [134] and Tarbell [184] for a review of the transport of LDL into the arterial wall, and Ross [159, 160] and Fan et al. [55] for more on the role of inflammatory response.

Nichols and O'Rourke [133] list six points on how atherosclerosis may alter arterial blood flow and hemodynamics, as follows:

1. by growing on the lumen and creating localized stenosis;

2. by causing the formation of a localized thrombus that further narrows or occludes the arterial lumen;

3. by formation of thrombus and possible detachment (embolus) which may lead to occlusion of smaller peripheral arteries;

4. by growing into the media, causing destruction and atrophy of structural elements and leading to the formation of aneurysm;

5. by stiffening the artery and altering wave reflection on vessels upstream;

6. by creating an abnormality in vascular mural tension that favours vasoconstriction.

The plaques (especially early ones) are usually locally distributed in larger arteries, such as the internal carotid artery (around the carotid sinus), the coronary

arteries, in the femoral and iliac arteries, the renal arteries, and in the infra-renal part of the abdominal aorta [8, 42, 133, 173, 205]. Figure 2.2 shows typical sites of atherosclerosis. More specifically these are around bifurcations and in major curvatures [121]. The local distribution of the plaques is what has given rise to the suspicion that local hemodynamic conditions are very important parameters behind the disease process, and this is where the fluid mechanics enter into the subject, which will be described more closely below.

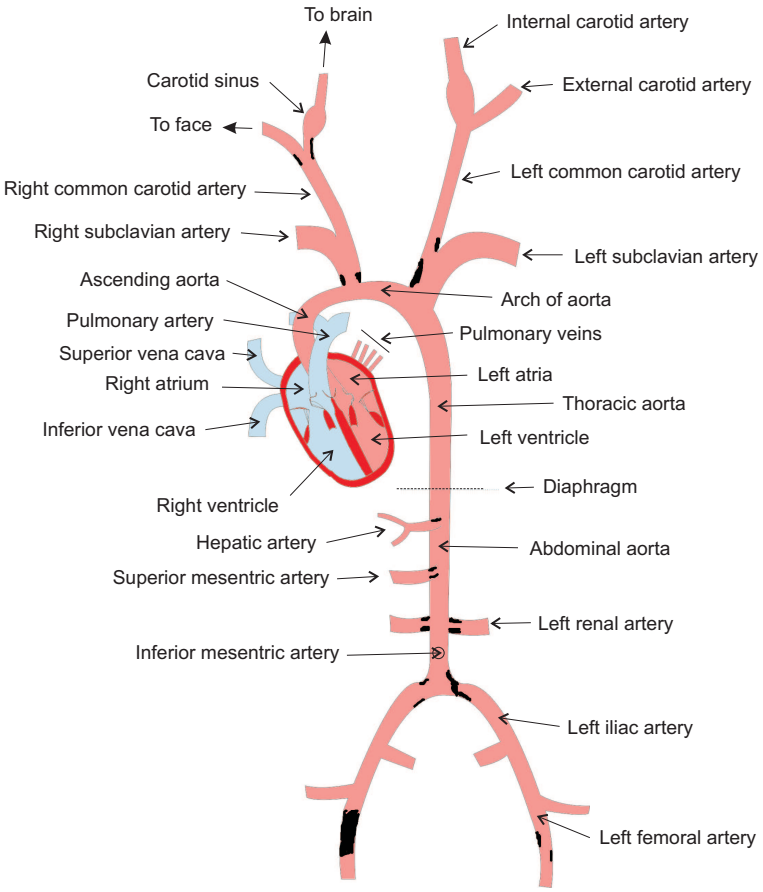

Figure 2.2: Sketch of the heart and blood vessels. The blue region shows where the blood is un-oxygenated and the pink color shows where the blood is oxygenated. The black spots show sites where atherosclerosis is commonly found; after DeBakey et al. [42].

2.4 Arteries, Atherosclerosis & Fluid Mechanics

The relation between atherogenesis and the dynamics of the flow field has been investigated since many years, as hemodynamic has been suspected to influence the pathogen process. It is not known through which mechanism hemodynamic affects atherogenesis. However, there are many indications that suggest the importance of fluid mechanics for atherogenesis.

The typical sites where plaques are found, the carotid artery sinus, the coronary arteries, the abdominal aorta, and the superficial femoral arteries [42, 208] are characterized by disturbed flow, flow unsteadiness and non-uniformities near junctions, or vessel curvature.

Several hypotheses have been proposed throughout the years. The first one to propose a hypothesis was probably Texon [187] who related the lateral pressure difference in the region where separation occurs to the disease. The pressure difference would cause a suction effect on the intima, which would lead to injury. However, the difference is too small to have such an effect.

Fox and Hugh [60] performed blood flow simulations and suggested that boundary layer separation occurs at sites where atherosclerosis is regularly found, with the result of deposition of blood-borne platelets and cholesterol. Later on Fry [67] did experimental studies on the descending thoracic aorta of mongrel dogs. He put a plug in the blood vessels, partially occluding the lumen with the purpose to increase the blood velocity locally in a controlled manner. The part of the lumen which was not plugged was open to the anterior endothelial cells. His results showed that as endothelial cells were exposed to a shear stress below $\sim 37.9\ Pa$, most of them remained normal in the absence of to much turbulence. Levels exceeding this limit showed rapid deterioration of the endothelial surface. These levels have now been shown to be too high to be relevant for a human model.

Caro et al. [27, 28, 57] showed in a more realistic aortic model a correlation between early atheroma and regions subject to low WSS, while the development of lesions seemed to be retarded in regions where the WSS is expected to be high. They suggested that the process of atherosclerosis is associated with shear dependent mass transport.

Friedman et al. [66] did numerical simulations of pulsatile blood flow through a 2D symmetrical branch model, and found spatial and temporal variations in wall shear. The highest values were found at the convex corner on the outer wall of the branch and in the neighborhood of the flow divider tip, while the lowest values were found at the outer wall of the daughter vessels a short distance distal to the corner. They found high shear, low shear and separation in those areas in the branch where lesions usually occur. They also emphasized the importance of transient flow and its disadvantage to the arterial wall. In comparison to Fry's [67] 37.9 Pa they reported the largest calculated value of the WSS to be $\sim 3\ Pa$, but they also mentioned that their results "should not be a firm basis on which

to discount high shear hypotheses of atherogenesis", although it does not support such theory.

Friedman's group continued their work and did experimental measurements in a cast of a human aortic bifurcation and found a negative correlation between intimal thickness and wall shear rate [65]. In [63] they compared measurements on casts from different human aortic bifurcations, and found variations sufficient to cause different hemodynamic properties. Such geometric effects may be a reason behind the variability in location and rate of development of atherosclerosis. In [64] they present numerical simulations which agree to earlier results.

Another study was presented by Bharadvaj et al. [14] who did measurements on a glass model with steady flow at different Reynolds numbers. They emphasize the complex flow field in a bifurcation due to the secondary flow, and state that zones susceptible to atherosclerotic disease experience low or reversed axial flow, or low or oscillatory shear stress. Regions subject to higher shear stress are instead free from disease. In [15] Bahradvaj et al. found peak values of WSS ranging between 2.5 and 5.0 Pa. They also emphasize the presence of oscillating shear stress and that this may disorient the cells of the endothelial layer, which will become more permeable to lipids present in the blood stream.

Ku et al. [104] more strongly emphasize the effect of oscillatory shear stress. The measurements were performed under pulsatile flow in a scale model of the human carotid bifurcation. The results were compared to intimal plaque thickness at corresponding sites of cadavers. Diastolic measurements of WSS and velocities were found to be similar to steady state cases, whereas they oscillated in both magnitude and direction during systole. Along the inner wall maximum WSS was found to be 4.1 Pa during systole, and 1.0 Pa during diastole. Here the WSS was uni-directional during systole. Along the outer wall, where the intimal plaque was thickest the instantaneous shear stress oscillated between -0.7 and 0.4 Pa. The conclusion was a strong correlation between intimal thickness and low time averaged WSS. They also discuss how low mean shear stress and oscillatory shear stress contribute to an increased fluid residence time at the corresponding sites, which may result in a modified mass transport of atherogenic substances between the lumen and the wall, in correspondence to the discussions of Caro et al. [57] and Jou et al. [94].

The most commonly discussed reason behind atherogenesis today is oscillating WSS. Gambillara et al. [72] exposed arteries from a pig to high- and low-uni-directional shear stress as well as oscillating shear stress and found no changes in the endothelial wall for the uni-directional shear stress, but for the oscillating. Their results may also imply that the shear stress may affect the anti-thrombogenic properties of the endothelium. Birchall et al. [16] show in their results a correlation between areas of low averaged shear stress and the formation of atherosclerosis. Other authors also found a correlation between major locations of atherosclerosis and oscillatory shear stresses; c.f. Asakura et al. [2], Zarins et al. [213] and Soulis et al. [172], who found a range of shear stresses between

0.75–2.25 Pa. Gibson et al. [74], Moore et al. [93] and Lee et al. [107] found a correlation between intimal thickness and oscillatory, or low time averaged shear stress.

On the other hand, Lutz et al. [118] who measured the WSS distribution in a rigid plastic cast of a canine artery during steady flow conditions, suggest a correlation between high levels of shear stress, and unstable stress patterns, with sites prone to atherosclerosis. Barbee et al. [6] exposed endothelial cells for flow with a shear stress of 1.2 Pa for 24 hours. The thickness of the intimal cell layer is shown to be significantly reduced. DePaola et al. [45] propose that highly elevated shear stress gradients can induce morphological and functional changes in the endothelium, in regions where the flow is disturbed, and contribute to atherosclerosis.

Friedman et al. [62] conclude from their experiments that the intimal thickness at sites exposed to large shear stresses increases quickly to a certain amount, after which it continues to grow slowly. On the other hand, at sites exposed to low shear stresses the intima grows more slowly, but after longer exposure times it overtakes the thickness of the sites exposed to large shear stress.

Ku [208] suggests that most intimal thickening is where the WSS < 1.0 Pa. Regions of relatively high uni-directional WSS tend to be spared from plaque development [93, 124] and even be protected by biochemical actions due to stimulus [105, 141]. Lee et al. [107] also conclude that the intimal growth tends to decrease the regions of low wall shear stress, resulting in larger velocities and a more even shear stress distribution. The vessel wall therefore seems to try to uphold a certain magnitude in WSS [173]. Ku [208] states in his review article that arteries do adapt to maintain a constant WSS of ~ 1.5 Pa.

For more comprehensive material on fluid mechanics in blood vessels and its relation to atherosclerosis, see [10, 23, 103, 185].

2.4.1 Numerical simulations of arterial blood flow

Although a great amount of both experimental and numerical investigations have been done on the subject there are still uncertainties in the behavior of the flow field, due to the complexities that appear in a multi-bifurcating vessel with compliant walls. As computers have become more efficient it has been possible to perform more accurate calculations that take more parameters into account. A decade ago Friedman et al. [64] performed 2D steady state numerical simulations, and today almost everyone performs 3D simulations. Better computing power resolves better the details of the flow of the idealized problem. Since the boundary properties of the vessel and the inflow/outflow boundary conditions are highly varying (and can even hardly replicate laboratory experiments), there is a major difficulty in applying Computational Fluid Dynamical (CFD) tools for quantitative analysis of physiological flows of ideal fluids. In addition, the rheological properties of the blood cannot be handled without introducing rather

crude models, that limit the validity of the results.

The flow field in the arteries is often simulated in different models; either of patient specific character [16, 64, 116], or in more idealized bifurcation models [34, 96, 128, 142, 145, 181]. These attempts to replicate patient anatomy do not necessarily yield more accurate results, due to natural inter-individual variations and normal variation due to aging.

A multi-factorial flow as the one in the arterial system is difficult to analyze in its whole, therefore several parameters are usually neglected or approximated. Steady state computations are often performed in order to save computational cost, whereas transient computations often give more realistic results and are in some cases necessary.

The investigated parameters vary, and one of them has been flexible walls of the blood vessels and its effect on the flow field, as well as on the distribution of shear stresses and its relation to atherosclerosis. The approaches also vary considerably, Liu et al. [116] and Perktold et al. [142] investigated compliant vessel walls and found a reduction of WSS (up to 25 %, but generally < 10 %), while Pivkin et al. [145] investigated a moving vessel situated on the heart following the heart movement. Other parameters have been related to non-Newtonian effects of the blood flow [33, 136, 142, 201], still many assume Newtonian flow [11, 16, 181], as will be discussed in the following Chapter.

Despite the different approaches most authors conclude that the geometric effects are of great importance for the flow field. As previously mentioned, for *in vivo* flow the geometrical variations are intricate and it is therefore difficult to generalize one case and apply it to another person. Therefore, an idealized model may give as much input (or even more) as a more patient specific model. Also, a large number of results from different kinds of geometries are needed in order to draw more general conclusions.

Chapter 3

Fluid Mechanical Aspects

This chapter describes the governing equations of the flows considered, followed by descriptions of different flow characteristics related to pipe flows and the previously discussed physiological systems.

3.1 Governing Equations

The classic theoretical base of fluid mechanics is the continuum assumption. Matter in general, whether fluid or solid, is built up of molecules or atoms with a certain empty space in between them. This is, however, generally not the common everyday experience, which is that of a continuous media. In continuum theory small scale molecular/atomic effects are neglected and a theory is built on the large scales [106]. Continuum theory assumes that matter properties can be expressed as the ensemble average over the molecules in an infinitesimally small control volume, where each volume is in the neighborhood of other volumes [106]. Such a limit exists if the control volume has a large enough number of molecules on one hand, and that the molecules are in equilibrium. In many applications this is a justified assumption, but not always. A requirement for the continuum assumption to be justifiable is that the mean free path between molecules λ should be much smaller than the smallest length scale of the flow l [149]. This can also be expressed in terms of the Knudsen number, $Kn << 1$, where

$$Kn = \frac{\lambda}{l} \tag{3.1}$$

In the case of blood, the continuum assumption implies that the flow structures have to be much larger than the (blood) cells. In contrast to the small molecules, the Knudsen number for the blood cells may not be small. Additionally, it is not obvious that the blood cells are in an equilibrium in all parts of the blood vessel tree. At the smaller vessels the Kn based on the blood cells are of order unity or larger. Thereby, one may have difficulties in assuming continuum properties for the blood in smaller blood vessels. Even under more optimal

conditions, the presence of cells also implies non-trivial rheological properties of the blood, which is briefly discussed below. In addition to the assumption of continuum, one often assumes that the flow of blood is incompressible.

The governing equations for an incompressible flow consist of the conservation of mass and momentum. Conservation of energy is ensured since the flow is assumed to be isothermal. For Newtonian fluids (as is assumed here) there is a linear relationship between the stress and the strain rate. For non-Newtonian fluids one has to add a model for the constitutive relationship. The system of PDE's (as shown in the following sections) consists of four equations for the four dependent variables; namely the velocity vector and the pressure. The steady state system of PDE's is elliptic in character and therefore requires boundary conditions (equal to the number of space dimensions) on all boundary points. The time-dependent system is classified as partially parabolic (i.e. the momentum equations are parabolic in time, but this is not the property of the continuity equation.) The time-dependent problem requires the same type of boundary conditions as the steady system. However, initial conditions have to be given as well.

The flow at the Reynolds numbers under consideration is laminar or transitional and hence, there is no need for explicit turbulence modeling. On the other hand transitional flows may contain smaller length scales then the corresponding laminar one, and therefore the computational grid should be fine enough to be able to resolve such small scales.

3.1.1 Rheological properties of blood

Viscosity is defined as the property which relates an applied stress to the resulting strain rate, where the strain rate is the rate of average decrease of the angle between two lines which are initially perpendicular in the unstrained state [204]. The strain rate can also be written as

$$\epsilon_{ij} = \frac{1}{2}\left(\frac{\partial u_i}{\partial x_j} + \frac{\partial u_j}{\partial x_i}\right) \tag{3.2}$$

where tensor/indical-notation is used, i.e. u_i is the velocity component in the i:th direction.

For a general fluid one has

$$\sigma_{ij} = f\left(\epsilon_{ij}\right) \tag{3.3}$$

where f is a function of the rate of strain tensor. The relation is valid for all flows, but an illustrative example is a fluid sheared between two plates at a low Reynolds number, shown in Figure 3.1. For regular fluids, such as water, some oils, and gases, the function f is linear, or the fluids are "Newtonian".

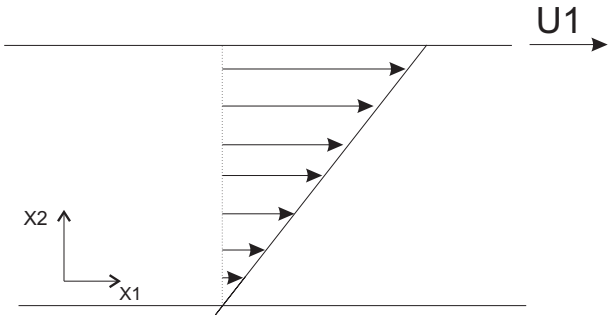

Figure 3.1: Shear flow due to motion of the upper plate.

The flow shown in figure 3.1 only has a constant streamwise velocity component, hence:

$$\sigma_{12} = \mu \frac{du_1}{dx_2} \tag{3.4}$$

where μ is the (coefficient of) dynamic viscosity.

The dynamic viscosity, however, depends on temperature and pressure and is therefore a thermodynamic property. In cases like this, where the flow is isothermal and the fluid is assumed to be of Newtonian character, the constant viscosity assumption is valid [9]. When (3.3) is non-linear the fluid is non-Newtonian.

Stokes [175] was the first who investigated the relation between stress and strain rate, in analogy with the Hookean relation in solid mechanics. He proposed three postulates as outlined by White [204] as:

1. The fluid is continuous, and its stress tensor σ_{ij} is at most a linear function of the strain rate ϵ_{ij}.

2. The fluid is isotropic, i.e., its properties are independent of direction, and therefore the deformation law is independent of the coordinate axes in which it is expressed.

3. When the strain rates are zero, the deformation law must reduce to the hydrostatic pressure condition, $\sigma_{ij} = -p\delta_{ij}$, where δ_{ij} is the Kronecker delta function.

Based on these three postulates the following general formulation for the stresses of a Newtonian flow may be obtained:

$$\sigma_{ij} = -p\delta_{ij} + \mu \left(\frac{\partial u_i}{\partial x_j} + \frac{\partial u_j}{\partial x_i} \right) + \delta_{ij} \lambda \frac{\partial u_i}{\partial x_i} \tag{3.5}$$

where λ is the (coefficient of) bulk viscosity. In the case of an incompressible fluid, the last term in (3.5) disappears and it is not treated any further. However,

more information about the coefficient of bulk viscosity is found in for example [106, 204].

Blood is a suspension containing different cells, with elastic characteristics, and molecules of largely varying sizes. Hence, blood should therefore be treated as a visco-elastic substance, affected by parameters such as plasma viscosity (probably affected by macro-molecular orientation), local red blood cell concentration and deformability and blood cell aggregation [133]. This reality gives the blood its non-Newtonian properties and the blood can not generally be considered as homogeneous. In smaller blood vessels where the size of the vessels are relatively small in comparison to the blood cells (i.e. large cell Knudsen number) the rheological properties of the blood are highly different from that in large vessels. Here, the non-Newtonian, or rheological, characteristics of the blood give the effect of reduced apparent viscosity [56]. The apparent viscosity is defined as the viscosity computed from Poiseuille's law (shown later) when the flow rate and pressure drop are measured [70].

The concentration of blood cells is higher towards the center of the vessel, as compared to near walls. This effect is the result of the motion of the cells subject to the shear in the blood. The phenomenon is often referred to as the Fåhraeus-Lindquist effect. The distribution of the particles towards the axis of the pipe is partly due to forces in a shear layer, as described by Saffmann [161, 162]. At small Reynolds numbers this effect is fairly small, and therefore this simple explanation is not adequate [70, 113].

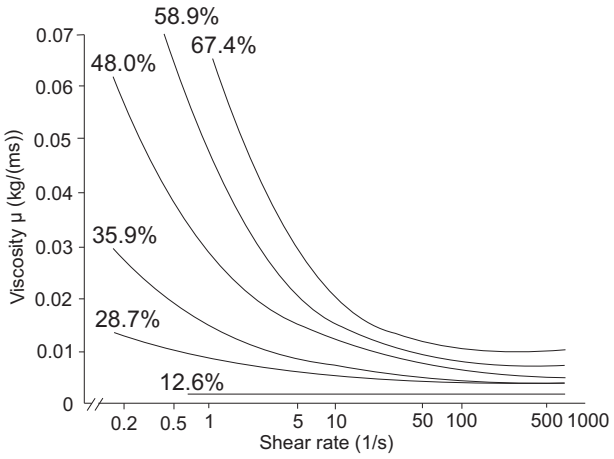

Figure 3.2: Viscosity as function of strain rate for various hematocrit levels, i.e. the concentration of red blood cells, which is about 45 % in normal individuals (after Brooks et al. [25]).

In larger vessels, as compared to blood cell diameter, blood is often considered as homogeneous [70]. In these vessels the shear rates are usually large enough in order to also consider the blood as a Newtonian fluid [133, 140]. However,

it should not be forgotten that the flow is pulsating, particularly in the large arteries, and the shear rates will therefore vary during the cycle.

Brooks et al. [25] examined the dependence of viscosity on shear rate and hematocrit, and found that whole blood behaves in a Newtonian manner up to a hematocrit level of about 12%. For larger hematocrit levels the viscosity increased, but as the shear rate increased the viscosity decreased again reaching an asymptotic value above shear rates of approximately 100 s^{-1}, i.e. shear thinning character (Figure 3.2).

Soulis [172] et al. investigated non-Newtonian viscosity models for flow through the left coronary artery and concluded that the Newtonian model is a good approximation at medium- and high-shear rates.

When the blood is considered as Newtonian and homogeneous, it has a density of about $\rho = 1.05 \cdot 10^3\ kg \cdot m^{-3}$ and an apparent dynamic viscosity of about four times that of water (at 20^0C) $\mu = 0.004\ kg \cdot m^{-1}s^{-1}$ [140]. The viscosity of the blood plasma alone is about 1.7 times that of water, i.e. $\mu_{plasma} \approx 0.0017$ $kg \cdot m^{-1}s^{-1}$. The plasma is usually considered to behave in a Newtonian way [133]. In the plasma the largest component length scale is for the albumin and the fibrinogen molecules (the latter is about $50nm$), which is only about one percent of the size of the capillaries. Therefore, those molecules are generally believed not to affect the flow in the way the much larger cells do [133, 200].

3.1.2 Continuity equation

The continuity equation for a fluid reads

$$\frac{\partial \rho}{\partial t} + \frac{\partial \rho u_i}{\partial x_i} = 0 \tag{3.6}$$

Thus, with the assumption of incompressibility the equation reduces to

$$\frac{\partial u_i}{\partial x_i} = 0 \tag{3.7}$$

3.1.3 Momentum equation

The momentum equation can be expressed as

$$\rho \frac{\partial u_i}{\partial t} + \rho u_j \frac{\partial u_i}{\partial x_j} = \frac{\partial \sigma_{ij}}{\partial x_j} \tag{3.8}$$

where the terms on the left hand side is density times transient- and convective-acceleration. The term on the right hand side is the total force per unit volume. Taking the divergence of (3.5) one has

$$\frac{\partial \sigma_{ij}}{\partial x_j} = -\frac{\partial p}{\partial x_i} + \mu \frac{\partial^2 u_i}{\partial x_j \partial x_j} \tag{3.9}$$

where the contributions of the stress tensor has been divided into its two components (i.e. the pressure and the viscous stress).

The form of the momentum equations for a Newtonian incompressible flow, usually referred to as the Navier-Stokes equations, is as follows.

$$\rho\frac{\partial u_i}{\partial t}+\rho u_j\frac{\partial u_i}{\partial x_j}=-\frac{\partial p}{\partial x_i}+\mu\frac{\partial^2 u_i}{\partial x_j\partial x_j} \tag{3.10}$$

3.2 Similarity

The Navier-Stokes equations (3.10) describe the balance of forces on a fluid element. These can be expressed, per unit volume, by words as:

$$\begin{gathered}\text{Transient inertia} + \text{Convective inertia} = \\ \text{Pressure on sides} + \text{Viscous forces on sides}\end{gathered} \tag{3.11}$$

It may be convenient to rewrite the equations on non-dimensional form, which is done by introducing a characteristic velocity U, a characteristic (angular) frequency ω and a characteristic length scale D. Using these characteristic parameters the equations will be non-dimensionalized by introducing the following non-dimensional terms.

$$\begin{gathered}x_i^*=\tfrac{x_i}{D}\quad u_i^*=\tfrac{u_i}{U}\\ p^*=\tfrac{p}{\rho U^2}\quad t^*=\omega t\end{gathered} \tag{3.12}$$

The expressions in (3.12) are substituted into (3.10) and the resulting expression is divided by $\frac{\rho U^2}{D}$. What follows, after some algebraic manipulations is an expression for the Navier-Stokes equations in non-dimensional form

$$\frac{\omega D}{U}\frac{\partial u_i^*}{\partial t^*}+u_j^*\frac{\partial u_i^*}{\partial x_j^*}=-\frac{\partial p^*}{\partial x_i^*}+\frac{\nu}{DU}\frac{\partial^2 u_i^*}{\partial x_j^{*2}} \tag{3.13}$$

where $\nu=\mu/\rho$ is the kinematic viscosity. The coefficient of the first term is recognized as a Strouhal number, $2\pi\cdot St_f=\frac{\omega D}{U}=\frac{\text{Transient term}}{\text{Convective term}}$. However, in a pulsating flow (laminar in a straight pipe) the relation between transient forces and viscous forces is more relevant. Therefore, traditionally, the non-dimensional numbers, Reynolds number, Re, and the Womersley number, α, are identified.

$$Re=\rho\frac{UD}{\mu}=\frac{\text{Convective inertia}}{\text{Viscous forces}} \tag{3.14}$$

$$\alpha=\frac{D}{2}\sqrt{\frac{\omega}{\nu}}=\left(\frac{\text{Transient inertia}}{\text{Viscous forces}}\right)^{1/2} \tag{3.15}$$

The Navier-Stokes equations can then be written as

$$4\frac{\alpha^2}{Re}\frac{\partial u_i^*}{\partial t^*} + u_j^*\frac{\partial u_i^*}{\partial x_j^*} = -\frac{\partial p^*}{\partial x_i^*} + \frac{1}{Re}\frac{\partial^2 u_i^*}{\partial x_j^{*2}} \tag{3.16}$$

The number 4 in the first term of (3.16) comes from the use of Womersley's [206] definition of α, based on the radius.

If one has two geometrically similar bodies, i.e. similar relative measures of the body, but not necessarily similar in absolute size, and if the Reynolds- and the Womersley-numbers are similar for the two cases, the solution will be the same; this is due to the non-dimensional form of (3.16). Thus, a time dependent flow is governed by two dimensionless numbers. Two different geometrically similar flows with the same Reynolds- and Womersley-numbers then satisfy dynamic similarity.

A large Womersley number, (3.15), indicates that the transient- or oscillatory-inertia forces dominate, and of course a low Womersley number indicates dominating viscous forces. The same is valid for the Reynolds number, but then as described by (3.14), the convective inertial forces are related to the viscous forces. Different levels of the Womersley- and the Reynolds-numbers in arteries are given in Table 3.1. The effect of these numbers on the flow field (of flow in a straight pipe) was described by Reynolds [155] and Womersley [206] respectively; this will be investigated more carefully in the following sections.

	Dog (20 kg)			Man (70 kg)		
Blood Vessel	*Velocity (cm/s)*	*Re*	α	*Velocity (cm/s)*	*Re*	α
Ascending aorta	15.8 (89/0)[a]	870 (4900)[b]	16	18 (112/0)[a]	1500 (9400)[b]	21
Abdominal aorta	12 (60/0)	370 (1870)	9	14 (75/0)	640 (3600)	12
Renal artery	41 (74/26)	440 (800)	3	40 (73/26)	700 (1300)	4
Femoral artery	10 (42/1)	130 (580)	4	12 (52/2)	200 (860)	4
Superior vena cava	8 (20/0)	320 (790)	10	9 (23/0)	550 (1400)	15
Inferior vena cava	19 (40/0)	800 (1800)	11	21 (46/0)	1400 (3000)	17

Table 3.1: Flow data of different blood vessels, after Bronzino [24]. [a] means (*systolic/diastolic*) and [b] means (*peak*).

3.3 Pipe Flows

3.3.1 Steady flow in a straight pipe

The flow through circular pipes is common in several fields of engineering. Applications may be cooling pipes in a nuclear reactor, flow in heat exchangers, ventilation systems, cardiovascular flow, etc. Viscous flow in pipes is often reported to first have been studied by Hagen (1839) [79] and Poiseuille (1840/1841) [147, 148]. Hagen was an engineer and Poiseuille was a physician studying blood flow. They obtained, by experiment, the famous relation now known as the Hagen-Poiseuille law, which reads

$$Q = -\frac{\pi a^4}{8\mu}\frac{dp}{dx} = -\frac{\pi a^4}{8\mu}\frac{\Delta p}{L} \tag{3.17}$$

where a is the pipe radius. The pressure gradient is constant over the entire length of the pipe, which motivates the last equality in the expression. The expression was derived mathematically by Stokes in 1845 as an application of the Navier-Stokes equations. However, Stokes did not publish the results, because he was unsure of the boundary condition at the tube wall. Instead the first derivation of the Poiseuille law from the Navier-Stokes equations is usually awarded to Hagenbach 1860 [178].

The continuity equation and the Navier-Stokes equations are written in cylinder coordinates as

$$\frac{\partial v}{\partial r} + \frac{v}{r} + \frac{1}{r}\frac{\partial w}{\partial \theta} + \frac{\partial u}{\partial x} = 0 \tag{3.18}$$

$$\frac{\partial u}{\partial t} + v\frac{\partial u}{\partial r} + \frac{w}{r}\frac{\partial u}{\partial \theta} + u\frac{\partial u}{\partial x} = -\frac{1}{\rho}\frac{\partial p}{\partial x} + \nu\left(\frac{\partial^2 u}{\partial r^2} + \frac{1}{r}\frac{\partial u}{\partial r} + \frac{1}{r^2}\frac{\partial^2 u}{\partial \theta^2} + \frac{\partial^2 u}{\partial x^2}\right) \tag{3.19}$$

$$\begin{aligned}\frac{\partial v}{\partial t} + v\frac{\partial v}{\partial r} + \frac{w}{r}\frac{\partial v}{\partial \theta} - \frac{w^2}{r} + u\frac{\partial v}{\partial x} = \\ -\frac{1}{\rho}\frac{\partial p}{\partial r} + \nu\left(\frac{\partial^2 v}{\partial r^2} + \frac{1}{r}\frac{\partial v}{\partial r} - \frac{v}{r^2} + \frac{1}{r^2}\frac{\partial^2 v}{\partial \theta^2} - \frac{2}{r^2}\frac{\partial w}{\partial \theta} + \frac{\partial^2 v}{\partial x^2}\right)\end{aligned} \tag{3.20}$$

$$\begin{aligned}\frac{\partial w}{\partial t} + v\frac{\partial w}{\partial r} + \frac{w}{r}\frac{\partial w}{\partial \theta} + \frac{vw}{r} + u\frac{\partial w}{\partial x} = \\ -\frac{1}{\rho r}\frac{\partial p}{\partial \theta} + \nu\left(\frac{\partial^2 w}{\partial r^2} + \frac{1}{r}\frac{\partial w}{\partial r} - \frac{w}{r^2} + \frac{1}{r^2}\frac{\partial^2 w}{\partial \theta^2} + \frac{2}{r^2}\frac{\partial v}{\partial \theta} + \frac{\partial^2 w}{\partial x^2}\right)\end{aligned} \tag{3.21}$$

where (x, r, θ) are in the axial-, radial-, and azimuthal-directions, with the velocity components (u, v, w), respectively.

The Poiseuille formula can be derived by, assuming laminar, steady and fully developed flow in a straight pipe. Then, $v = w = 0$, $\frac{\partial}{\partial t} = 0$, and $\frac{\partial u}{\partial \theta} = \frac{\partial u}{\partial x} = 0$. Applying these conditions to (3.18)-(3.21) reveals through the continuity equation that $v = 0$, the radial momentum equation gives that the pressure is constant over a cross-section. The flow is therefore fully specified by the momentum equation in the axial direction. After simplification (3.19) is written as

$$\frac{dp}{dx} = \frac{\mu}{r}\frac{d}{dr}\left(r\frac{du}{dr}\right) \tag{3.22}$$

Integrating (3.22) twice and applying the boundary conditions $u(r = a) = 0$, where a is the pipe radius (at the wall), and $\frac{du(r=0)}{dr} = 0$, the following expression is obtained for the axial velocity:

$$u(r) = -\frac{dp}{dx}\frac{1}{4\mu}\left(a^2 - r^2\right) \tag{3.23}$$

The volume flow through the pipe is given by integrating (3.23) as

$$Q = \int udA = \int_0^a u(r)2\pi r dr = -\frac{\pi a^4}{8\mu}\frac{dp}{dx} \tag{3.24}$$

and the relation is recognized.

This expression is often found in text books on physiology when the flow of blood in blood vessels is to be described. The Poiseuille law should, however, be used with precaution. The expression is restricted to fully developed steady and laminar flow in a very long straight pipe with rigid walls. This situation is naturally seldom found in a real biological application, where the flow even may be turbulent in the larger arteries, not least at pathological conditions such as a stenosis [19, 140]. Poiseuille's law may still give some valuable information, not least in the smaller blood vessels where the flow is laminar. According to (3.17) the flow is proportional to the radius to the power of four. This reveals that the vasoconstriction/vasodilation function, that changes the vessel radius in order to direct the blood to a particular site or increase blood pressure, of the blood vessels is very efficient [71].

3.3.2 Pulsating flow in a straight pipe

A Poiseuille flow is based on steady flow assumptions and naturally deviations from the parabolic solution is to be expected in an unsteady flow. In the case of a large Womersley number in a straight pipe of laminar flow, transient inertial effects are dominating over viscous effects. In the central part of the pipe, where the velocity is high, the transient forces are balanced by pressure forces, like in an inviscid case. In Poiseuille flow the pressure forces are instead balanced by viscous forces in the central parts, as well as close to the pipe wall [71]. In pulsating

flow the slowly moving fluid near the wall, i.e. with small momentum, responds quicker to changes in the pressure gradient than the high velocity fluid in the center. The unsteady profile at large Womersley numbers is therefore expected to be blunt in the central core of the pipe. This phenomenon has been described by Womersley [206] and others [167], but the dimensionless group describing the oscillations is usually referred to as the Womersley number as above. However, it is sometimes also referred to as the Stokes number, St, due to the development of the Stokes layer in Stokes flow. Note that this number should not be mixed with the Stokes number as it is defined for a particle moving in a fluid. The Stokes layer thickness is given by $\delta = (2\nu/\omega)^{1/2}$. Comparing δ with α in (3.15), it follows that $St = a/\delta = \alpha/\sqrt{2}$. Hence, the Stokes number (and Womersley number) can be seen as a measure of pipe radius over Stokes layer thickness.

Following Womersley's treatment we start from the momentum equation in the axial direction in cylinder coordinates, (3.19). The same assumptions regarding the flow as for Poiseuille are made, with the exception that the time derivative is kept. The governing equation is now expressed as

$$\rho\frac{\partial u}{\partial t} = -\frac{\partial p}{\partial x} + \mu\left(\frac{\partial^2 u}{\partial r^2} + \frac{1}{r}\frac{\partial u}{\partial r}\right) \tag{3.25}$$

The pressure gradient may then be expressed as a Fourier series function $\frac{\partial p}{\partial x}(t) = \sum_{i=-\infty}^{\infty} c_n e^{\omega_n t}$. However, since (3.25) is linear in u one may solve for only one term at a time, and then add up the individual solutions. Therefore, the pressure gradient is expressed as $\frac{\partial p}{\partial x} = Ae^{i\omega t}$, which after some rearrangement yields

$$\frac{\partial^2 u}{\partial r^2} + \frac{1}{r}\frac{\partial u}{\partial r} - \frac{1}{\nu}\frac{\partial u}{\partial t} = -\frac{A}{\mu}e^{i\omega t} \tag{3.26}$$

where u is the velocity in the axial direction. A is constant since at each point in time the pressure gradient is assumed constant, in relation to Poiseuille flow. Now, also u is expressed as a complex periodic function in the anzats $u(r,t) = B(r)e^{i\omega t}$, and after re-arranging one has

$$\frac{d^2 B}{dr^2} + \frac{1}{r}\frac{dB}{dr} + \frac{i^3\omega}{\nu}B = -\frac{A}{\mu} \tag{3.27}$$

This equation is a form of Bessel equation and has the following solution, where the boundary conditions $B(a) = 0$ and $|B(0)| < \infty$ have been implemented.

$$B = \frac{A}{\rho}\frac{1}{i\omega}\left\{1 - \frac{J_0\left(r\sqrt{\frac{\omega}{\nu}}i^{3/2}\right)}{J_0\left(a\sqrt{\frac{\omega}{\nu}}i^{3/2}\right)}\right\} \tag{3.28}$$

where $J_0\left(xi^{3/2}\right)$ is the Bessel function of order zero, a is the radius of the pipe. Now, $a\sqrt{\frac{\omega}{\nu}} = \alpha$ is the Womersley number, and $y = \frac{r}{a}$. The solution of (3.26) is

then written as

$$u = \frac{A}{\rho}\frac{1}{i\omega}\left\{1 - \frac{J_0\left(\alpha y i^{3/2}\right)}{J_0\left(\alpha i^{3/2}\right)}\right\} e^{i\omega t} \tag{3.29}$$

The real- and imaginary-parts of the pressure gradient, $Ae^{i\omega t}$, correspond to the real- and imaginary-parts of the solution, respectively. A more detailed treatment of the solution procedure, as well as tables of Bessel functions, are given by Zamir [212]. McDonald [123] also presents the basic ideas and several informative figures on this topic. The first term in (3.29) is just a constant, the second term (in brackets) describes the cross-sectional distribution of the velocity, and the third exponential term describes the variation of velocity with time. Integrating (3.29) over the cross-section gives the flow as function of time

$$Q(t) = \int_0^a u(r,t)2\pi r dr = \frac{A}{\rho}\frac{\pi a^2}{i\omega}\left\{1 - \frac{2\alpha i^{3/2}}{i^3\alpha^2}\frac{J_1\left(\alpha i^{3/2}\right)}{J_0\left(\alpha i^{3/2}\right)}\right\} e^{i\omega t} \tag{3.30}$$

where J_1 is the Bessel function of first order and first kind. Womersley [206] shows that as α goes to zero the flow goes towards the Poiseuille solution. As α increases the solution quickly moves away from the Poiseuille solution, and finally the peak flow goes asymptotically to some value of about 10 % of the Poiseuille solution. Due to the inertia of the fluid, as α increases, the flow will eventually lag about 90^0 behind the pressure gradient, which is the driving force of the flow. Integrating (3.30) over a period shows that the net flow in this oscillating flow is zero [212].

Figures 3.3(a) and 3.3(b) show the characteristics of the axial velocity at two different Womersley numbers. The larger Womersley number profiles show slightly decreased magnitude in the center, but with more flat distributions. There is also earlier and more back flow near the walls, due to the larger acceleration.

3.3.3 Flow in curved pipes

It is a well known fact that a curved pipe induces secondary motion. Dean [40, 41] describes the phenomenon theoretically for a laminar case with small curvature ratio a/R_c, where a is the radius of the pipe and R_c is the radius of curvature. As the fluid in a pipe follows a curved path, the fluid towards the center-line of the pipe with larger velocity experience larger inertial force (centrifugal force) as compared to the fluid in the boundary layer near the wall. In order to counteract the increased inertial force, a lateral pressure gradient is built up. However, because the pressure is approximately constant across transversal lines above the outer wall of curvature, and that the flow in the wall boundary layer has less momentum than in the core, a force imbalance appears near the wall. Hence, near the wall the pressure force is larger than the inertial and viscous forces, which

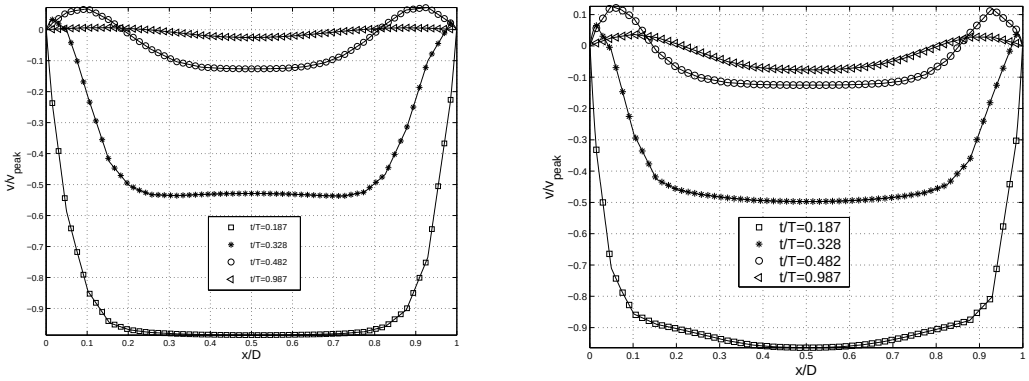

(a) $\alpha = 6.75$ (b) $\alpha = 11.75$

Figure 3.3: Velocity profiles at different Womersley numbers.

induces a motion along the wall. These secondary streams meet at the inner wall of curvature where they merge and by continuity they result in a central stream towards the outer wall. These vortices are then stretched by the downstream flow. Curvature effects are found in both laminar and turbulent flows, although it has been reported that the influence of curvature is less pronounced in a turbulent case [167].

By taking the curl of the Navier-Stokes equations (3.10) one gets the vorticity equations:

$$\frac{\partial \omega_i}{\partial t} + u_j \frac{\partial \omega_i}{\partial \omega_j} = \omega_j \frac{\partial u_i}{\partial x_j} + \nu \frac{\partial^2 \omega_i}{\partial x_j \partial x_j} \tag{3.31}$$

These equations describe the transport of vorticity $\left(\omega_i = \epsilon_{ijk} \frac{\partial u_k}{\partial x_j}\right)$ in the flow field. The terms on the left are transient and convective transport of vortex lines, and the terms on the right describe intensification of vorticity when the vortex lines are stretched, and diffusion of vorticity. The equations do not have any source terms in incompressible flow, and therefore the vorticity can not be created by the flow field itself, only transported within it. Instead the vorticity is again induced through the boundary conditions, here the wall, as previously described; cf. Batchelor [9].

A steady fully developed flow in a curved pipe can be described by introducing a curvlinear orthogonal coordinate system, according to Figure 3.4.

The position vector is described by

$$\begin{aligned} \mathbf{r}(x, r, \theta) &= X\mathbf{e}_X + Y\mathbf{e}_Y + Z\mathbf{e}_Z \\ &= ((R_c + r sin\theta)\, sin\phi, (R_c + r sin\theta)\, cos\phi, r cos\theta) \end{aligned} \tag{3.32}$$

where $\mathbf{e}_X$, $\mathbf{e}_Y$, $\mathbf{e}_Z$ are the cartesian base vectors, $x = R_c\phi$ is the axial component, r is the radial component and θ is the azimuthal component. As described by

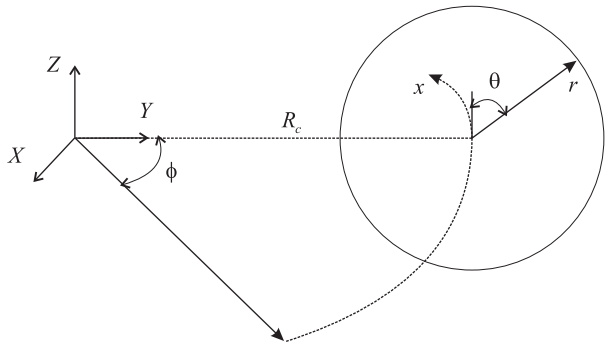

Figure 3.4: Coordinate system for flow through a curved pipe.

Ramgard [151] the new set of base vectors are defined as

$$e_i = \frac{1}{h_i}\frac{\partial \mathbf{r}}{\partial s_i} \tag{3.33}$$

where $h_i = \left|\frac{\partial \mathbf{r}}{\partial s_i}\right|$ are the scale factors, and $(s_1, s_2, s_3) = (x, r, \theta)$. Computing the scale factors give $h_x = 1 + \frac{r}{R_c} sin\theta$, $h_r = 1$, and $h_\theta = r$. Here, the velocity components in the (x, r, θ) direction are given by (u, v, w).

Using these parameters one can express the velocity components, gradients and divergence fields of the continuity and the Navier-Stokes equations in the new basis [151]. The equations are given in (3.34)-(3.37).

$$\frac{R_c}{(R_c + rsin\theta)}\frac{\partial u}{\partial x} + \frac{\partial v}{\partial r} + \frac{1}{r}\frac{\partial w}{\partial \theta} + \frac{v}{r} + \frac{vsin\theta + wcos\theta}{R_c + rsin\theta} = 0 \tag{3.34}$$

$$\begin{aligned}
&\frac{\partial u}{\partial t} + \frac{R_c}{(R_c + rsin\theta)}u\frac{\partial u}{\partial x} + v\frac{\partial u}{\partial r} + \frac{w}{r}\frac{\partial u}{\partial \theta} + \frac{u\,(vsin\theta + wcos\theta)}{R_c + rsin\theta} \\
&\quad = \frac{1}{\rho}\left[\frac{R_c}{R_c + rsin\theta}\left(-\frac{\partial p}{\partial x}\right) + \mu\left\{\frac{R_c^2}{(R_c + rsin\theta)^2}\frac{\partial^2 u}{\partial x^2} + \frac{\partial^2 u}{\partial r^2} + \frac{1}{r^2}\frac{\partial^2 u}{\partial \theta^2}\right.\right. \\
&\qquad - \frac{u}{(R_c + rsin\theta)^2} + \frac{1}{r}\frac{\partial u}{\partial r} + \frac{1}{(R_c + rsin\theta)}\left[sin\theta\frac{\partial u}{\partial r} + \frac{cos\theta}{r}\frac{\partial u}{\partial \theta}\right] \\
&\qquad\qquad \left.\left. + \frac{2R_c}{(R_c + rsin\theta)^2}\left[cos\theta\frac{\partial w}{\partial x} + sin\theta\frac{\partial v}{\partial x}\right]\right\}\right]
\end{aligned} \tag{3.35}$$

$$\frac{\partial v}{\partial t}+\frac{uR_c}{(R_c+rsin\theta)}\frac{\partial v}{\partial x}+v\frac{\partial v}{\partial r}+\frac{w}{r}\frac{\partial v}{\partial \theta}-\frac{w^2}{r}-\frac{u^2sin\theta}{R_c+rsin\theta}$$
$$=\frac{1}{\rho}\left[-\frac{\partial p}{\partial r}+\mu\left\{\frac{R_c^2}{(R_c+rsin\theta)^2}\frac{\partial^2 v}{\partial x^2}+\frac{\partial^2 v}{\partial r^2}+\frac{1}{r}\frac{\partial v}{\partial r}-\frac{v}{r^2}\right.\right.$$
$$+\frac{1}{r^2}\frac{\partial^2 v}{\partial \theta^2}-\frac{2}{r^2}\frac{\partial w}{\partial \theta}+\frac{1}{(R_c+rsin\theta)}\left[sin\theta\frac{\partial v}{\partial r}+\frac{cos\theta}{r}\frac{\partial v}{\partial \theta}-\frac{wcos\theta}{r}\right]$$
$$\left.\left.-\frac{2R_csin\theta}{(R_c+rsin\theta)^2}\frac{\partial u}{\partial x}-\frac{sin\theta}{(R_c+rsin\theta)^2}\left[vsin\theta+wcos\theta\right]\right\}\right] \quad (3.36)$$

$$\frac{\partial w}{\partial t}+\frac{uR_c}{(R_c+rsin\theta)}\frac{\partial w}{\partial x}+v\frac{\partial w}{\partial r}+\frac{w}{r}\frac{\partial w}{\partial \theta}+\frac{vw}{r}-\frac{u^2cos\theta}{R_c+rsin\theta}$$
$$=\frac{1}{\rho}\left[-\frac{1}{r}\frac{\partial p}{\partial \theta}+\mu\left\{\frac{R_c^2}{(R_c+rsin\theta)^2}\frac{\partial^2 w}{\partial x^2}+\frac{\partial^2 w}{\partial r^2}+\frac{1}{r}\frac{\partial w}{\partial r}-\frac{w}{r^2}\right.\right.$$
$$+\frac{1}{r^2}\frac{\partial^2 w}{\partial \theta^2}+\frac{2}{r^2}\frac{\partial v}{\partial \theta}+\frac{sin\theta}{(R_c+rsin\theta)}\frac{\partial w}{\partial r}+\frac{cos\theta}{(R_c+rsin\theta)}\left[\frac{1}{r}\frac{\partial w}{\partial \theta}+\frac{v}{r}\right]$$
$$\left.\left.-\frac{2R_ccos\theta}{(R_c+rsin\theta)^2}\frac{\partial u}{\partial x}-\frac{cos\theta}{(R_c+rsin\theta)^2}\left[vsin\theta+wcos\theta\right]\right\}\right] \quad (3.37)$$

The following analysis is based on Dean's [40, 41] papers, although the notation is taken from Ward-Smith [199]. The flow is now considered to be steady and fully developed, i.e. $\frac{\partial}{\partial t}=\frac{\partial}{\partial x}=0$. The equations (3.34)–(3.37) are simplified and rewritten on a similar form as presented by Dean [40].

$$\frac{\partial v}{\partial r}+\frac{1}{r}\frac{\partial w}{\partial \theta}+\frac{v}{r}+\frac{vsin\theta+wcos\theta}{R_c+rsin\theta}=0 \quad (3.38)$$

$$v\frac{\partial u}{\partial r}+\frac{w}{r}\frac{\partial u}{\partial \theta}+\frac{u\left(vsin\theta+wcos\theta\right)}{R_c+rsin\theta}=-\frac{R_c}{R_c+rsin\theta}\frac{\partial}{\partial x}\left(\frac{p}{\rho}\right)$$
$$+\nu\left[\left(\frac{\partial}{\partial r}+\frac{1}{r}\right)\left(\frac{\partial u}{\partial r}+\frac{usin\theta}{R_c+rsin\theta}\right)+\frac{1}{r}\frac{\partial}{\partial \theta}\left(\frac{1}{r}\frac{\partial u}{\partial \theta}+\frac{ucos\theta}{R_c+rsin\theta}\right)\right] \quad (3.39)$$

$$v\frac{\partial v}{\partial r}+\frac{w}{r}\frac{\partial v}{\partial \theta}-\frac{w^2}{r}-\frac{u^2sin\theta}{R_c+rsin\theta}=-\frac{\partial}{\partial r}\left(\frac{p}{\rho}\right)$$
$$-\nu\left[\left(\frac{1}{r}\frac{\partial}{\partial \theta}+\frac{cos\theta}{R_c+rsin\theta}\right)\left(\frac{\partial w}{\partial r}+\frac{w}{r}-\frac{1}{r}\frac{\partial v}{\partial \theta}\right)\right] \quad (3.40)$$

$$v\frac{\partial w}{\partial r}+\frac{w}{r}\frac{\partial w}{\partial \theta}+\frac{vw}{r}-\frac{u^2 cos\theta}{R_c+rsin\theta}=-\frac{1}{r}\frac{\partial}{\partial\theta}\left(\frac{p}{\rho}\right)$$
$$+\nu\left[\left(\frac{\partial}{\partial r}+\frac{sin\theta}{R_c+rsin\theta}\right)\left(\frac{\partial w}{\partial r}+\frac{w}{r}-\frac{1}{r}\frac{\partial v}{\partial\theta}\right)\right] \quad (3.41)$$

If one then assumes that $a/R_c << 1$ the motion may be considered as a perturbation of Poiseuille flow. For Poiseuille flow we have, as shown before, $u = A_p\left(a^2-r^2\right)$, where $A_p = -\frac{dp}{dx}\frac{1}{4\mu}$, $v = w = 0$, and $p/\rho = C_p x$, where C_p is a constant. By the assumption of small perturbations the following solution is proposed: $u = A_p\left(a^2-r^2\right)+u_1$, $v = v_1$, $w = w_1$, and $p/\rho = C_p x + p_1/\rho$; u_1, v_1, w_1, and p_1 are all small of order a/R_c. These assumptions, and ignoring all terms larger than order a/r_c equations (3.38)–(3.41) become

$$\frac{\partial v_1}{\partial r}+\frac{1}{r}\frac{\partial w_1}{\partial\theta}+\frac{v_1}{r}=0 \quad (3.42)$$

$$-2A_p r v_1 = -\left(1-\frac{rsin\theta}{R_c}\right)\frac{\partial}{\partial x}\left(C_p x+\frac{p_1}{\rho}\right)$$
$$+\nu\left[\left(\frac{\partial^2}{\partial r^2}+\frac{1}{r}\frac{\partial}{\partial r}+\frac{1}{r}\frac{\partial^2}{\partial\theta^2}\right)\left(A_p\left(a^2-r^2\right)+u_1\right)\right.$$
$$\left.+\left(\frac{\partial}{\partial r}+\frac{1}{r}\right)\left(\frac{A_p\left(a^2-r^2\right)sin\theta}{R_c}\right)+\frac{1}{r}\frac{\partial}{\partial\theta}\frac{A_p\left(a^2-r^2\right)cos\theta}{R_c}\right] \quad (3.43)$$

$$-\frac{A_p^2\left(a^2-r^2\right)^2}{R_c}sin\theta=-\frac{\partial}{\partial r}\left(\frac{p}{\rho}\right)-\frac{\nu}{r}\frac{\partial}{\partial\theta}\left(\frac{\partial w_1}{\partial r}+\frac{w_1}{r}-\frac{1}{r}\frac{\partial v_1}{\partial\theta}\right) \quad (3.44)$$

$$-\frac{A_p^2\left(a^2-r^2\right)^2}{R_c}cos\theta=-\frac{1}{r}\frac{\partial}{\partial\theta}\left(\frac{p}{\rho}\right)+\nu\frac{\partial}{\partial r}\left(\frac{\partial w_1}{\partial r}+\frac{w_1}{r}-\frac{1}{r}\frac{\partial v_1}{\partial\theta}\right) \quad (3.45)$$

Ignoring small terms of (3.43), what is left is $C_p = -4\nu A_p$, which is the relation between pressure gradient and axial velocity in a straight circular pipe. Equation (3.43) can then be simplified into

$$-2Arv_1=-\frac{\partial}{\partial x}\left(\frac{p_1}{\rho}\right)-\frac{6\nu Arsin\theta}{R_c}+\nu\left(\frac{\partial^2 u_1}{\partial r^2}+\frac{1}{r}\frac{\partial u_1}{\partial r}+\frac{1}{r^2}\frac{\partial^2 u_1}{\partial\theta^2}\right) \quad (3.46)$$

If one then writes the variables as

$$\begin{aligned} u_1 &= u'(r)sin\theta \\ v_1 &= v'(r)sin\theta \\ w_1 &= w'(r)cos\theta \\ \frac{p_1}{\rho} &= p'sin\theta \end{aligned} \quad (3.47)$$

where the primed variables depend only on r, and substitute these into (3.44)–(3.46) four new quite similar expressions, but with primed variables, are obtained. By integrating those equations and using proper boundary conditions (cf. Dean [40] for details), and introducing the Reynolds number the following solutions are obtained.

$$\frac{u}{U} = 2\left(1-\zeta^2\right)\left[1 - \frac{3}{4}\frac{a}{R_c}\zeta sin\theta + \frac{Re^2 a}{11520R_c}\zeta sin\theta\{19 - 21\zeta^2 + 9\zeta^4 - \zeta^6\}\right] \tag{3.48}$$

$$v/U = \frac{Rea}{144R_c} sin\theta\left(1-\zeta^2\right)^2\left(4-\zeta^2\right) \tag{3.49}$$

$$w/U = \frac{Rea}{144R_c} cos\theta\left(1-\zeta^2\right)\left(4-23\zeta^2+7\zeta^4\right) \tag{3.50}$$

Here, $U = u_0/2 = Aa^2/2$, $\zeta = r/a$, $Re = Aa^3/\nu = 2Ua/\nu$, and u_0 is the axial velocity at the center line. The solution is plotted in Figure 3.5, where the secondary flow is illustrated with vectors and the axial flow with countours. As shown in the figure the smaller curvature ratio solution has a more symmetric parabolic axial velocity distribution, as compared to the figure with larger curvature ratio. There the profile is skewed towards the outer wall of the bend.

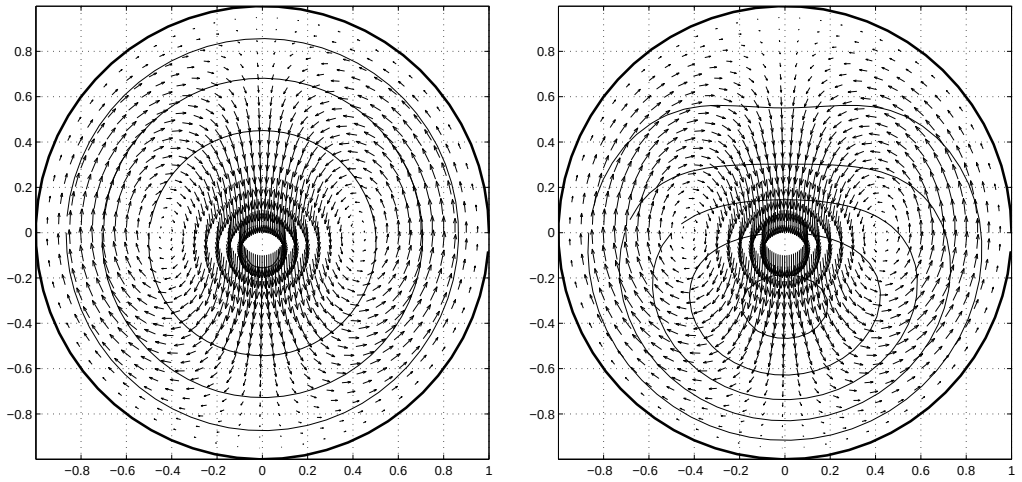

(a) $a/R_c = 0.0001$ (b) $a/R_c = 0.001$

Figure 3.5: Solution of the velocity field in a curved pipe accordig to Dean [40]. The larger curvature ratio solution shows an axial velocity distribution more skewed towards the outer wall of the bend. 2D velocity vectors show the secondary flow.

One can identify the components of the Dean number, $De = Re\sqrt{\delta}$ and $\delta = a/R_c$, in (3.48)–(3.50) as parameters that determines the solution. The Dean

number is a measure of centrifugal forces over pressure forces, which are the forces determining the secondary flow. In this first order approximation $p_1 = 0$, i.e. the pressure gradient is similar to what is found in Poiseuille flow. As curved pipe flow experience larger pressure drop than straight pipe flow, this is incorrect and a higher order approximation is needed, which Dean also did in another work [41].

Going back to equations (3.38)–(3.41), and assuming again that $R_c >> a$, so that $(R_c + rsin\theta)$ can be replaced by R_c, the equations can be simplified into

$$\frac{\partial v}{\partial r} + \frac{v}{r} + \frac{1}{r}\frac{\partial w}{\partial \theta} = 0 \tag{3.51}$$

$$v\frac{\partial u}{\partial r} + \frac{w}{r}\frac{\partial u}{\partial \theta} = -\frac{\partial}{\partial x}\left(\frac{p}{\rho}\right) + \nu\left[\frac{\partial^2 u}{\partial r^2} + \frac{1}{r}\frac{\partial u}{\partial r} + \frac{1}{r^2}\frac{\partial^2 u}{\partial \theta^2}\right] \tag{3.52}$$

$$v\frac{\partial v}{\partial r} + \frac{w}{r}\frac{\partial v}{\partial \theta} - \frac{w^2}{r} - \frac{u^2 sin\theta}{R_c} = -\frac{\partial}{\partial r}\left(\frac{p}{\rho}\right) - \frac{\nu}{r}\frac{\partial}{\partial \theta}\left(\frac{\partial w}{\partial r} + \frac{w}{r} - \frac{1}{r}\frac{\partial v}{\partial \theta}\right) \tag{3.53}$$

$$v\frac{\partial w}{\partial r} + \frac{w}{r}\frac{\partial w}{\partial \theta} + \frac{vw}{r} - \frac{u^2 cos\theta}{R_c} = -\frac{1}{r}\frac{\partial}{\partial \theta}\left(\frac{p}{\rho}\right) + \nu\frac{\partial}{\partial r}\left(\frac{\partial w}{\partial r} + \frac{w}{r} - \frac{1}{r}\frac{\partial v}{\partial \theta}\right) \tag{3.54}$$

These equations are recognized as the continuity- and Navier-Stokes-equations in cylinder coordinates, with the addition of centrifugal force terms (the fourth terms on the left hand side of (3.53) and (3.54)). They clearly illustrate the effect of a bend pipe as compared to a straight. Dean [41] further introduces a secondary stream function and then makes the equations non-dimensional. Two dimensionless groups appear, $G' = Ga^2/(\mu u_0)$ and $K = 2u_0^2 a^3/(\nu^2 R_c)$. u_0 is the center line velocity, and G is the axial pressure gradient. If the Reynolds number $Re = \frac{UD}{\nu}$, where U is the mean flow velocity and D the diameter, is approximately similar to $Re = \frac{au_0}{\nu}$, the parameter $K = \frac{2aRe^2}{R_c}$, which is one form of what is usually referred to as a Dean number. The Dean number defined above is related to K as

$$De = \frac{1}{\sqrt{2}}\sqrt{K} \tag{3.55}$$

It can be shown, by introducing a certain set of non-dimensional parameters, that for small enough Dean numbers ($K < 576$ or $De < 16.97$) the flow is approximately determined by the Dean number alone [199], which is rather small. A Reynolds number of $Re = 2000$ and a curvature ratio of $\delta = 0.1$, which is not that large, give a Dean number $De \approx 632$. Still the classical Dean solutions present important phenomena, present at large Dean numbers as well. For a review over asymptotic solutions of these equations, as well as unsteady cases, cf. Pedley [140].

Since Dean, several investigations of curved pipe flow and the resulting secondary flow have been carried out. For example, Horlock [87] investigated the secondary flow through a pipe with sinusoidal shaped centerline. He found that in such a geometry the secondary flow may be enhanced or weakened along the pipe. The secondary flow could also be reduced by a consecutive bend, yet the flow field could not be fully restored. Barua [7] examined curved tubes at a large Dean number and found fair agreement between theory and experiments. Lyne [119] took unsteadiness into account and found that for a large Womersley number the secondary flow in the interior of the pipe is in the opposite direction to that predicted for a steady pressure gradient. The flow along the wall from outside to inside in the Stokes layer, returns through the more central parts of the Stokes layer. This draws the fluid in the core around in the opposite direction as compared to the steady state solution. Smith [170] described flows at different (secondary) Reynolds-, Womersley-, and Dean-numbers. He examined limits of these numbers, such as purely steady, purely oscillatory and intermediate limits. A proposal was given for a path of development from steady to pulsating flow, in which the secondary flow first is steady, then undergoes an unsteady period, and finally becomes steady again. He also suggests the existence of a line in the Womersley-, Dean-number parameter space which separates outward moving secondary flow from partly inward moving.

Dennis [44] found that for a large enough Dean number a two vortex solution exists. Talbot and Gong [182] did experiments on the entrance flow into a curved pipe. They found two vortex pairs in parallel at about the same height at one instant in time, and separation was found where the boundary layers merge at the inner side. Chang and Tarbell [30] did numerical simulations of Talbot and Gongs experiments, and also computations for two more physiological pulses. They observed the presence of complex vortical structures.

Snyder et al. [171] show that downstream development of the skewed axial velocity component can not be characterized by a single dimensionless parameter. In loosely coiled pipes ($\delta < 1/140$) the growth of axial skew depends strongly on the pipe curvature through the Dean number, while in more tightly coiled pipes the skewness does not depend on curvature. Instead a formula depending on Reynolds number, pipe radius and entrance length is presented. Hamakiotes et al. [81] examined the effect of the Womersley- and the Reynolds- number on the flow through a curved pipe. At small Re Dean vortices (single) appear for all times at all α. For larger Re Lyne-type vortices were observed and always appeared during the acceleration part of the period.

Rindt et al. [158] used finite elements for computing the entrance region in sinusoidally varying flow. A reversed axial flow region was found along the inner wall, and the axial profile was affected and skewed towards the outer wall. A large value of the Womersley parameter resulted in a steady secondary flow field and Lyne-type vortices. Also, a more physiological flow rate was used and they found that the influence of the diastolic phase on flow phenomena in the systolic

phase is of minor importance.

Sudo et al. [176] did measurements and numerical simulations on the oscillating flows through a curved channel at various Dean- and Womersley-numbers. They found five categories for the secondary flow: 1) Dean circulation type, 2) deformed Dean circulation, 3) intermediate circulation between Dean and Lyne, 4) deformed Lyne circulation, and 5) Lyne circulation. Tada et al. [180] did numerical simulations of pulsatile flow at various Womersley- and Dean-numbers, as well as various β (amplitude ratio or ratio between through flow and oscillatory flow). They classified the secondary flow patterns into three base groups (all combinations may also appear): viscosity dominated type, inertia dominated type and convection dominated type. When the amplitude ratio of the volumetric flow rate was equal to one, four to six vortices of the secondary flow appeared at a large Dean number. Lyne-type flow patterns disappeared for $\beta \geq 0.5$. Komai and Tanishita [102] simulated fully developed flow through a curved tube using a physiological pulse at a Dean-number $De = 393$, and various Womersley numbers and curvature ratios. They found that the secondary flow did not dissipate before the next period which gave effect on the flow of the next period. At small intermittency parameter (ratio of systolic time/period time) additional vortices were formed near the inner wall.

Boiron et al. [17] examined numerically and experimentally the starting effect on the secondary flow in a bend at various Womersley- and Dean-numbers. The velocity profiles and secondary flow patterns, and their dependence on the initial hydrodynamic conditions were examined.

Siggers and Waters [168] investigated the character of the secondary flow in a curved pipe with pulsatile flow. For a sinusoidal pressure gradient they identified three classes of stable solutions that are either periodic symmetric, periodic asymmetric or asymmetric solutions, depending on the secondary Reynolds number. The transition between solutions is dependent on the curvature. When the Dean number increases a solution can go through an unstable phase to find a new stable solution.

Thus, complex vortical structures appear more often in pulsating flows than the regular Dean vortex structure. These flows are also relevant in physiological systems and measurements have been done by several researchers. Clark and Schultz [36] show skewed velocity profiles in the axial direction from measurements in the aorta. Similar results was shown by Nerem et. al. [129], from measurements in the aorta of a horse. Motomiya and Karino [127] also show patterns of secondary motion.

3.3.4 Flow in bifurcations

The flow through a pipe bifurcation has much of the characteristics in common with the flow through a bent pipe. In the case of a 90-degree bifurcation the streamlines are bent in a similar way as in a 90-degree curved pipe. Therefore similar secondary flow features in the daughter branch are expected as in a developing flow through a curved pipe. However, the flow field is also, to some extent, subject to effects from the other branches.

Figure 3.6 shows a sketch of the flow field in a bifurcating pipe. Vortex containing separation bubbles and secondary counter rotating vortices are expected in this kind of bifurcation. The region to the opposite side of the daughter branch may not be separated as soon as the region inside the daughter branch, however, a skewed distribution of axial velocity towards the daughter branch is still expected.

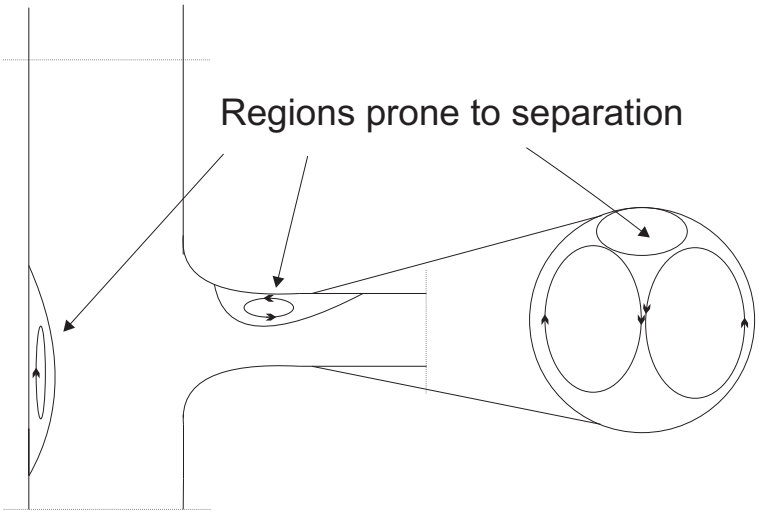

Figure 3.6: Sketch of expected regions of separation and secondary counter rotating vortices; partly after Pedley [140].

The cardiovascular system naturally contains a large amount of bifurcations of which most are asymmetric; asymmetry due to different cross-sectional areas of daughter vessels, different branching angles, and different flow conditions [140]. The only well known symmetric bifurcation is where the aorta bifurcates into the two iliac arteries [132, 140, 189]. Therefore, a deep understanding of the effects of bifurcations, symmetric or asymmetric, is essential. Data about the secondary flow through bifurcations, such as a T-junction, is sparse. In a biomechanical context focus has often been on WSS distributions rather than what in the flow field is the cause of the characteristics of the WSS.

Balshazy et al. [5] did numerical simulations of flow through two different bifurcations, one with sharp edges and one with blended edges of a more physiological character. The model with blended edges showed reduced skewness of the

flow profiles in the daughter branches, smaller secondary velocity components, and regions of reversed flow in the vicinity of the carina. Comer et al. [38] made a detailed description of the steady flow through a three generation symmetric bifurcation tree at Reynolds numbers $500 - 2000$. They also considered particle distribution in the geometry in a second paper [37]. Zhang et al. [214] studied a 3D three generation symmetric bifurcating flow at Re ranging between 200-1600 for steady flow with either parabolic or uniform inlet velocity distribution. They found skewed velocity profiles, as well as unbalanced mass flow rate ratios between the branches.

Tadjafar [181] studied the influence of local geometric parameters on the flow. Investigated parameters were bifurcation area ratio, bifurcation angle, inlet flow Re (steady), and asymmetric outlet pressure boundary conditions. It was found that the area ratio had the greatest influence on the flow within the physiologically relevant regime.

Moyle et al. [128] investigated the effect of adding secondary flow to the inlet velocity profiles on the WSS and on an oscillatory shear index (OSI). The test was done for three realistic models of a carotid bifurcation, where curvature and helical pitch was added to the entrance vessels. They found that the effects of secondary flow on the WSS break down within a few diameters of the inlet. Fresconi [61] investigated secondary flow fields in a multiple (3 generation) symmetric bifurcation model of an airway at $6 < Re < 350$ and Womersley numbers $0 < \alpha < 1$. They found that for the larger Re the secondary flow did not have enough time to develop before the subsequent bifurcation. They also found that flow patterns in the oscillatory case were similar to the steady state cases at the corresponding Re, which is not very surprising due to the small α [139].

Samagio and Vlachos [164] performed steady numerical simulations of the flow through a rectangular T-junction and found regions of secondary flow. Two recirculation zones were also found, one in the main branch, opposite to the trailing edge of the daughter branch, and one in the daughter branch at the inner wall. The axial velocity profile was skewed towards the daughter branch. Schinas and Mathioulakis [166] investigated pulsating flow in a 90-degree bifurcation of a square duct using LDV. They examined separation dynamics, and during acceleration the flow was attached, but close to peak flow separation was initiated at both branches. Nikolaidis and Mathioulakis [135] did measurements in a 90-degree bifurcation under pulsating conditions, also in a square duct, at different Reynolds- and Womersley-numbers. During acceleration phase all recirculation zones and vortices were washed out and new Dean vortices were created. At one instant, at $\alpha = 9.42$ and $Re = 412$, four vortices were found. An example of a multiple vortex structure in pulsating flow through a 90-degree bifurcation at $Re = 1450$, and $\alpha = 6.75$ is shown in Figure 3.7. Two vortex pairs of different structure are found in (a) and (b), respectively.

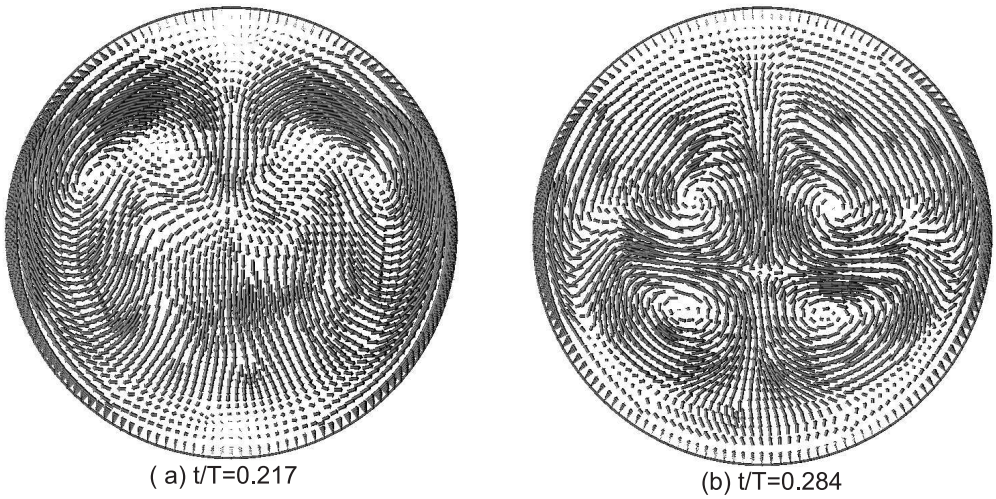

Figure 3.7: Multiple vortices at different times in pulsating flow; (a) near peak flow phase; and (b) at inlet flow deceleration phase.

3.3.5 Entrance flow

Another cause of secondary flow is an entrance region. Due to the no-slip condition at the wall the velocity there is small and, hence, the flow rate is larger at the central parts of the pipe. For a straight pipe, a parabolic profile develops if the flow is laminar. Every branch (if it is large enough) affects the flow downstream of it, since the flow is strongly disturbed, and if the distance to the next branch is not too large, one would not observe a fully developed profile.

The inlet length is usually referred to the distance (in a steady flow) from the entry section to where the center line velocity is less than 1 % from the corresponding velocity in a parabolic profile; this definition was proposed by Boussinesq in 1891, who suggested the relation $L/D = 0.065Re$, where D is the tube diameter and Re the Reynolds number [47]. Other authors have suggested other relations, and Lew and Fung [110] conclude that, $L/D = 0.08Re$, is quite good for Reynolds numbers greater than 50. They also show that as the Reynolds number goes to 0 the inlet length goes to about $L/D = 0.65$. Durst et al. [47] propose the relation $L/D = [(0.619)^{1.6} + (0.0567Re)^{1.6}]^{1/1.6}$. On the other hand, Schlichting [167] reports an inlet length of $x/D =$ 50-100 for laminar steady flow and $x/D =$ 25-40 for turbulent flows.

For an unsteady flow the boundary layer is affected by both convective and transient accelerations. Fung [71] suggests that when $\delta_1 = \delta_2$, where $\delta_1 = 6.5\left(\frac{\nu}{\omega}\right)^{1/2}$ is boundary layer thickness due to inertial forces, associated with transient accelerations, and $\delta_2 = 4\left(\nu x/U\right)^{1/2}$ is the boundary layer thickness associated with convective accelerations, $L = 2.64\frac{U}{\omega}$; U is a characteristic velocity and

ω is the angular frequency. For $x < L$, $\delta_1 > \delta_2$ and transient accelerations tend to dominate, whereas when $x > L$, $\delta_1 < \delta_2$ and convective accelerations tend to dominate.

3.3.6 Pressure wave in tubes with extensible walls

The pressure wave induced by the heart ejection of blood into the aorta, travels along the aortic wall and is also transmitted and reflected at each bifurcation. This pulse increases the radius of the vessel and also works as a help pump by storing potential energy, which is then converted to kinetic energy when the vessel radius decrease again during diastole. This is due to the elastic fibres, as was discussed in a previous Chapter. At simplified conditions the propagating wave can be described by a wave equation, cf. [71, 112, 140, 212] for more comprehensive analyses. The ratio between peak velocity and the vessel wall wave speed is about $u_{max}/c = 0.20 - 0.25$ in the thoracic aorta of a normal dog, and is expected to be similar for humans. The ratio decreases as the arteries become smaller [140]. It has to be pointed out that the propagation speed depends primarily on the mechanical properties of the arteries. The more severe atherosclerosis is, the stiffer are the walls and the higher the speed of pressure wave propagation. Arterial compliance and the stiffness depend on mean blood pressure, aging and rate of ventricular ejection. The aging usually implies stiffening due to arteriosclerosis, and the visco-elastic properties of the vessel wall influence the dependence on rate of ejection. Usually the pressure pulse travels at a speed of about 4–5 m/s in young people, while in elderly it travels at a speed of about 10–15 m/s [109].

3.3.7 Transition to turbulence in pipe flows

Table 3.1 presents characteristic data from the cardiovascular system of both a dog and a human. For a man the Reynolds number ranges between 200 in the femoral artery, to 9400 in the ascending aorta at peak flow. Osborne Reynolds [155, 156] found in his experiments (published 1883), when he introduced dye into the entrance of a circular pipe, that at low speed $Re < 1900$ the flow remained laminar and the dye did not mix by convection. However, when the flow velocity was increased to a Re over approximately 2000, depending on the entrance conditions, the dye was mixed and convected over the whole cross section. Less initial disturbances have been shown to raise the transitional Reynolds number significantly. Schlichting [167] reports that a transition Reynolds number as high as approximately $40 \cdot 10^3$ has been obtained in steady flow. Fully developed turbulence is otherwise generally considered to be found around $Re = 3000$ [149], but as stated the local properties are very significant for when to expect transition.

White [204] presents a list of parameters influencing transition to turbulent flow. The following may be relevant here (with point four added):

1. Pressure gradient
2. Free-stream turbulence
3. Wall roughness
4. Inlet conditions

The pressure gradient is favourable during the accelerating phase of the pulse which reduces the risk of early transition, however, at the decelerating phase the pressure gradient will temporarily be adverse. Initial disturbances that might trigger transition may exist in the case of arterial flow, since the heart is not standing still, and since the fluid has little time to settle before it is being ejected from the heart. Also, the flow passes through the aortic valve, which may induce some secondary motion. However, as the flow is accelerating during the first half of systole, disturbances will be damped to some extent.

Lefebvre et al. [108] reports transition at $Re \approx 10^6$, in accelerating flows, where the Reynolds number is based on instantaneous velocity and pipe diameter. However, during the decelerating part of the pulse Nerem et al. [130, 131] noted high frequency disturbances in the aorta of dogs. They found that at a peak Reynolds number of $Re = 250\alpha$ (for $5 < \alpha < 20$) there is an approximate line separating the laminar flow from disturbed flow (eventually turbulent); where α is the Womersley number based on the radius of the aorta. This may be expected due to that the small disturbances need a certain amount of time in order to develop. For larger species, including humans, turbulent flow, or at least transitional flow, may be expected in larger arteries (Table 3.1).

One instability mechanism present in a periodic flow, is naturally the point of inflection of the velocity profile during deceleration, if it is strong enough; fast deceleration has been shown to decrease the critical Reynolds number drastically [80, 140].

When it comes to pulsatile flow in circular pipes at transitional Reynolds numbers, there are several experimental and numerical studies. Yellin [209] investigated pulsatile flow in a pipe. He found that classical stability concepts, such as point of inflection and Reynolds number requires modification in a pulsating flow. He recognizes three other criteria for transition: a source of disturbance, relaxation time (i.e. time period of small velocity), and distance from the fluid under observation to the source of disturbance. Flows with a low frequency and a large amplitude of the oscillating component shows a reduced disturbance growth rate as compared to a steady flow of similar steady component. He suggests that systolic acceleration may be laminar despite the large systolic velocity, whereas diastolic deceleration probably produces disturbed but not turbulent flow.

Sarpkaya [165] examined pulsating pipe flow. He found that pulsating flow is more stable than steady Poiseuille flow. The critical Reynolds number is determined by the Womersley number and the ratio of pulsating velocity amplitude

over total mean velocity. Despite points of inflection disturbances may not grow. For a certain velocity ratio the critical Reynolds number is decreasing for increasing Womersley numbers between 4–7.8, i.e. in contrast to Nerem [131]. For increasing oscillations amplitude the critical Reynolds number is increasing to a certain limit, whereafter it rapidly decreases again. An $\alpha = 6.5$ has a maximum critical Re of approximately 3300. The critical Reynolds number for non-harmonic oscillations were smaller.

Hino et al. [85] did experiments on the transition to turbulence in purely oscillating pipe flows at $105 \leq Re \leq 5830$, based on oscillating mean velocity amplitude, and for Womersley numbers $1.9 \leq \alpha \leq 8.75$. They identified three different regimes, 1) weakly turbulent flow, 2) conditionally turbulent flow, and 3) fully turbulent flow. The critical Reynolds number of the first transition decreased as the Womersley number increased. In the conditionally turbulent flow, transition was identified during the decelerating part of the pulse, while it relaminarized during the next accelerating part; also at $Re = 5830$ if the Womersley number was large enough.

Eckmann et al. [48] did measurements of oscillating flow in a straight circular pipe, at $9 < \alpha < 33$ and $389 < Re < 47 \cdot 10^3$. They report laminar flow for $Re < 23 \cdot 10^3$ and $8.9 \leq \alpha \leq 32.2$ (where the velocity scale of the Reynolds number is based on the stroke distance $d = V_T/\pi a^2$, as $U = \omega d$. If the velocity instead is based on distance over period time the Re should be divided by π, i.e. $Re < 7.3 \cdot 10^3$.). At measured $Re > 23 \cdot 10^3$ the core remained laminar while the Stokes layer became unstable during the deceleration phase.

Lodahl et al. [117] examined combined oscillatory and steady (pulsatile) flow through a circular pipe. The investigated ranges were $0 \leq Re \leq 1.6 \cdot 10^5$, $0 \leq Re_w \leq 7 \cdot 10^6$, and $4.2 \leq \alpha \leq 75$, where $Re_w = aU_m/\nu$ is the oscillatory flow boundary layer Reynolds number, and Re is the Reynolds number based on the steady flow component. U_m is the peak of the oscillatory flow and $a = U_m/\omega$. Re_w is related to Re_{w_D}, which is based on pipe radius as $Re_{w_D} = \sqrt{4\alpha^2 Re_w}$. Transition was detected at $Re > 2000$, depending on Re_w and α, and it was found that the flow can be laminarized by the superimposed oscillatory flow component. For the pure oscillatory flow below $\alpha = 10$, transition came at smaller Re_w for smaller α. At very large α, Re_w reaches the asymptotic value $Re_w = 1.5 \cdot 10^5$, which is a known value from plane oscillatory flow. The critical Re increases as Re_w increases to a certain limit, whereafter the oscillatory flow has become turbulent itself. Then, the combined flow also becomes transitional. However, although a smaller α has a larger critical Re_w, the large α has a larger critical Re, but the oscillatory component needs to be of an optimal magnitude. The simple relation by Nerem [131] thus seems to neglect important parameter dependencies.

Tuzi et al. [192] obtained qualitatively similar results as Lodahl et al. [117] by doing numerical simulations, although their transitional Re is larger, which is suggested as depending on the small perturbations in the numerical simulations as compared to the experiments. They also found that as turbulence is present,

the dynamics are similar to the steady case. A log-law layer can be found in both the pure oscillating and the pulsating case. They suggest a classification of the flow into four different regimes: 1) "laminar regime", 2) small amplitude perturbation regime called the "disturbed laminar regime", 3) the flow where turbulent bursts are found during the decelerating phase of the cycle, called the "intermittently turbulent regime", and 4) turbulence throughout the whole cycle called the "fully turbulent regime". They introduced wall imperfections of sinusoidal variation and amplitude $\epsilon/\delta = 0.005$, where δ is the Stokes layer thickness. The wall imperfections should trigger transition, and lower the critical Re to numbers obtained in laboratory experiments (as mentioned above that was not really obtained). It was found that the different wall imperfections influenced the small amplitude perturbations at laminar flow, but had no influence on the transition process, and the turbulence structure, at Re far above the critical value.

A review of pulsatile pipe flows is given by Carpinlioglu et al. [29].

Geometrical variations (leading to adverse pressure gradients) may have a more severe impact on transition into turbulence, especially at pathological constrictions, such as a stenosis, which may drastically increase the velocity, inducing Kelvin-Helmholtz like instabilities [19].

White [202] and Taylor [186] experimentally showed that curvature has a stabilizing effect on the flow field. They showed that transition into turbulence, for flow in a curved pipe, was delayed to a Reynolds number approximately three times higher than that described by Osborne Reynolds [155]; thus, secondary flow seems to have a stabilizing effect on the flow field.

Chapter 4

Fluid-Structure Interaction

Fluid-Structure Interaction (FSI) is the name for problems where a fluid domain Ω^f and a solid domain Ω^s interacts through their common boundary, Γ^f on the fluid side and Γ^s on the solid side. The fluid affects the solid by the stress it imposes on its boundary, i.e. it creates a traction boundary condition for the solid. This causes the solid to deform Ω^s and Ω^f (depending on the computational approach used), and the fluid domain gets new wall boundary conditions to adapt to.

These kinds of problems are found in various fields of science and engineering. In aero-elasticity the fluid induce forces on the solid, such as wings [97], bridges [21], buildings [22], and hard disk drives [100] that causes structural motion and deformation. In some cases that may lead to aerodynamic flutter, and even structural failure. In the human body, FSI is utilized in the sensory parts of the auditory systems (so called hair cells), in the peristaltic motion of the intestinum and the axons of the nerve cells. In these physiological systems, FSI is an important beneficial factor. Also, the expansion of the arteries during systole in young individuals is physiological, and it helps maintaining lower blood pressure. During systole arteries experience deformations in both the radial- and axial-directions due to the flow [35]. Veins, on the other hand, in particular in the upper part of the body, may collapse as the back-pressure becomes low [140, 189]. Calo et al. [26] used FSI for estimation of drug delivery in different coronary artery models. Fukui et al. [69] studied the effect of longitudinal and axial wall motion on the distribution of WSS. Kock et al. [101] used FSI for studying plaque rupture in carotid arteries. Valencia et al. [193] studied stenotic flows using an FSI-formulation. Oscuii et al. [137] studied the effect of wall stiffness on flow and WSS, also using FSI-modeling.

The field equations governing the fluid flow and deformation of a solid are closely related. Historically, the two fields have been developed in parallel, with the Finite Element Method (FEM) being used in structural flow analyses, and different discretization methods (e.g. FEM, Finite Differences, finite-volumes) have been used in fluid analyses. In recent years, due to the needs in many

engineering fields there have been several attempts to merge the two approaches. In the following a review of some of these approaches will be given followed by a description of the FSI-implementation used here.

4.1 Computational Approaches

The different computational approaches used are often categorized into different categories of solution procedure (Note that this categorization terminology is not unique [218].). In the *monolithic* approach the fluid- and the solid-systems of equations, including interaction boundary conditions, are solved for simultaneously [88, 92], whereas in the *partitioned* approach the systems of equations are solved for sequentially [95, 144, 195, 207]. In the monolithic approach one obtains the solution for each time step immediately, however, the system of equations may be large and so is the computational time. Recently, it has been argued that the monolithic approach is still competitive, even for large scale problems [43, 84]. Also, by using the monolithic approach, in contrast to the partitioned approach, the most common solvers for fluid- and structural-mechanics can not be used. Thus, in general the monolithic approach is considered more stable and accurate, while the partitioned approach gives more flexibility [88].

In the partitioned approach it is possible to use different time steps for the fluid and solid, respectively, that may be optimized for computational cost and capturing the different time scales of the two domains [144]. The partitioned approach is often referred to as weakly- or strongly-coupled. *Weak coupling* is usually referred to as where the fluid and the solid are only solved for once per time step. *Strong coupling*, on the other hand, is when an iterative procedure is made for each time step, where finally both the fluid and the solid solver has converged to the specified accuracy [195, 207].

The algorithm developed here is illustrated in Figure 4.1, which is a weak coupling approach. A strong coupling procedure would add additional inner loops of steps 1 through 8. Then after the solid deformation, the flow field would be computed again, giving rise to a modified flow field, which is applied to the structural solver, but where the old displacements are used again as initial data. The sub-iterations are continued until convergence, whereafter a step forward in time is taken.

The weak method often requires a smaller time step for numerical stability as compared to the strong coupling approach [122]. Many authors prefer the strong coupling due to its often better stability characteristics. However, under the right conditions the weak coupling approach is also usable. Recently, Beulen et al. [13] found satisfying convergence characteristics for weakly coupled FSI for flow through pipes.

The treatment of the fluid- and the solid-domains, and their interaction, can also be done using different approaches. Traditionally, fluid domains are treated

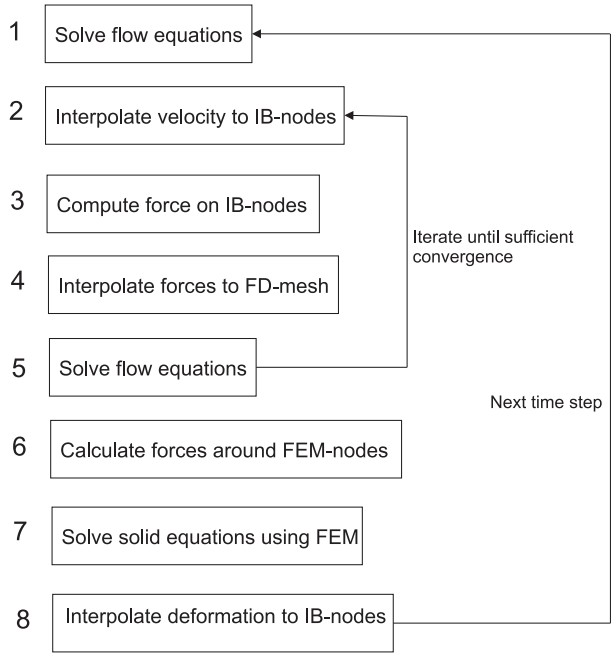

Figure 4.1: Solution procedure.

using Eulerian (fixed) meshes, while the solid mesh is Lagrangian, i.e. it deforms with the material deformation. Different ways of combining Lagrangian deforming meshes and an Eulerian description of the fluid have been proposed. Two approaches are the *Arbitrary Lagrangian-Eulerian (ALE)* formulation and the *Immersed Boundary (IB)* family of formulations; the latter one has been used here.

In the ALE formulation mesh-motion is taken into account in the Eulerian description of mass- and momentum-conservation, i.e. a more arbitrary description is considered [86]. In an FSI-context the fluid domain deforms according to the deformation of the structural domain [46].

The boundary between fluid and solid is well defined using the ALE formulation, however, at large deformations and rotations the fluid mesh elements may become badly shaped, resulting in reduced accuracy. One possibility is then to re-discretize the mesh, which naturally takes computational time. Also, the interpolation to the new mesh may cause new errors.

Van Loon et al. [194] compared the performance of an ALE formulation and some different fictitious domain methods. They solved both fluid and solid equations using finite element formulations. The ALE formulation was preferred as long as no remeshing was required, due to the high precision, since in their case the fluid and solid mesh-nodes coincided at the boundary-interface. However, as deformations, displacements, or rotations of the solid body become large, they suggest that a fictitious domain method might be a good choice, since mesh

generation is only required prior to computation, and the fluid and solid meshes can be generated separately.

Another way of relating the fluid- and solid-domains is by using a variant from the Immersed Boundary (IB) family of methods. The basic idea is that the fluid domain is represented by a fixed Eulerian mesh, wherein the solid domain is represented by a set of source terms that simulate an arbitrary wall boundary, by forcing the wanted boundary condition. When the right boundary condition is obtained at the right position the solution has converged. In the context of FSI, another mesh of Lagrangian movable character is created which represents the solid body and deforms according to theories of solid mechanics. Again, the deformations, and deformation velocities are transferred to the fluid solver, where the boundary sources are moved accordingly.

Different ways of treating the immersed (or virtual) boundary have been proposed through the years. Peskin [143] proposed probably the first IB method with application to a deforming (2-D) heart valve. The geometry is determined by a Lagrangian arbitrary mesh on which forces are specified. The forces are distributed to the fluid mesh using an approximate Dirac δ-distribution that is slightly spread out on the fluid mesh, since the boundary at most times does not coincide with a fluid mesh-node.

Goldstein et al. [77] used the ideas of Peskin [143], but suggested to compute the force field on the boundary using a feedback loop, similar to a PI-regulator from control theory, instead of Peskin's more complex idea of lines of tension and their deformation that determines the force. The draw-back of the control theory approach is that one needs to determine the coefficients of the two terms of the regulator.

Glowinski et al. [75, 76] suggested another way of specifying the geometrical boundary on a simple mesh using Lagrange multipliers. The method is called a "fictitious domain method" and they obtained second order accuracy.

Saiki et al. [163] used the method of Goldstein et al. [77] of using a feedback forcing term added to the momentum equation, in order to model the IB-interface. However, they use a high order finite difference method for the Eulerian fixed mesh, instead of the spectral method used by Goldstein et al., which suppress some numerical oscillations.

Mohd-Yusof [126] estimated the force terms needed to model the IB by applying the Navier-Stokes equations at the boundary, where the velocity time-derivative is estimated using the wanted and the present velocities.

Fadlun et al. [53] compared the force term computational methods of Goldstein et al. [77] and Mohd-Yusof [126], and found the latter more efficient because a larger CFL-number could be used. They also combined the IB-method with LES modeling. Three different methods for transferring the force to the fluid mesh were used: 1) stepwise geometry, the nearest cell is assumed to be the boundary, 2) volume fraction weighting of the force, and 3) linear interpolation to nearest cell where the boundary is supposed to have the right velocity. The

force is then computed in a similar way as Mohd-Yusof [126]. The third approach gives the best results and is estimated to second order accurate.

Kim et al. [99] used the methodology of Fadlun et al. [53], however, in contrast to Fadlun they only added momentum inside the body or on the boundary of the body. They also added mass sources/sinks in order to correct continuity errors over the immersed boundary, which is shown to be significant for the method. Silva et al. [169] used a similar method as Fadlun et al. [53] for estimating the force field on the boundary, however, here the different components of distance $< 2\Delta x$ from the IB are interpolated from surrounding points in the fluid domain. For points on the IB, cells inside the IB-domain were also taken into account. The method is called "the physical virtual method". Zhang et al. [217] proposed an "Immersed finite element method", using finite elements for both the Eulerian fluid mesh, and the deformation of the Lagrangian mesh. The forces were distributed onto the fluid mesh using an approximate Dirac delta function.

Other methods, similar to those discussed above, have been introduced by Bertrand et al. [12], Tseng et al. [190], Wang et al. [198], Ikeno et al. [90], and Vos et al. [197], also in the context of FSI [3, 98, 198, 211, 220].

A disadvantage of IB-methods is that the boundary of the solid does not coincide with nodes of the fluid mesh cells (when using a staggered fluid mesh coincidence of all variables is naturally impossible). Therefore, interpolation between the Cartesian and the boundary mesh is necessary. Also, the highest resolution of the fluid mesh is needed near a solid boundary at high Re. In the case of deforming boundaries, re-meshing would possibly be needed, and in that case one of the advantages with the method is gone. However, higher order methods, up to fourth order, have been suggested, such as the "immersed interface methods" by Li et al. [111], Linnick et al. [115] and Bonfigli [18], where the finite difference scheme is corrected near the IB.

Other alternatives to IB and ALE are, for instance, high order wall treatment, using cell blocking and interpolation or extrapolation of variables [78], or overlapping grid techniques, where interpolation takes place in overlap regions [191].

4.2 Gaussian Immersed Boundary Method

The IB-method developed here has partially been described by Revstedt et al. [153, 154].

The IB is represented by a 2D Lagrangian surface mesh. This mesh geometrically describes the surface of a 3D body. The fluid may flow inside or around this object. The fluid flow is handled using a Finite Difference scheme on a Cartesian 3D mesh; the FD-solver is further described in Chapter 5.

As described above the basic idea, using an IB-method, is to model the body by introducing source terms into the flow field. These momentum source terms

force the flow field to fulfill the preset boundary conditions; a moving or steady wall. Since the IB-mesh and the fluid mesh generally do not coincide some method is needed to estimate the actual velocity at the boundary surface, as well as distributing the resulting force field.

The solution procedure, excluding the structural solver, can be divided into the following steps.

1. Compute the flow field of the fluid mesh, including boundary conditions.
2. Determine the three velocity components at the IB-nodes.
3. Compute the IB-forces based on the velocity defect between wanted and actual velocity.
4. Distribute the force field onto the fluid mesh.
5. Solve the flow field with the new forces, and go back to 2.

The process is iterated until sufficient convergence for each time step.

The velocity components at the IB-nodes are estimated using the same Gaussian distributed weights, as when the IB-forces are distributed back onto the fluid mesh. A velocity component u_b at the IB-node at location $x_i = X_i$ can, using theory of distributions, be expressed as

$$u_b\left(X_i,t\right) = \int_{\Omega^f} u\left(x_i,t\right)\delta\left(x_i - X_i\right)dV \tag{4.1}$$

where x_i are the coordinates, and $u\left(x_i,t\right)$ is a velocity component of the fluid domain Ω^f. $\delta(x_i)$ is the Dirac δ-distribution in three dimensions, with the properties

$$\int_{-\infty}^{\infty}\delta\left(x_i\right)dV = 1 \tag{4.2}$$

$$\delta\left(x_i\right) = \begin{cases} 0 & , x_i \neq 0 \\ \infty & , x_i = 0 \end{cases} \tag{4.3}$$

Expression (4.1) holds if $u\left(x_i,t\right)$ is a continuous function over Ω^f, which it is not, since we are dealing with a discretized domain. Instead, one may use a Gaussian distribution with a sufficiently large standard deviation, σ, that spreads the distribution function over a few cells of the fluid mesh. The Gaussian distribution is expressed as

$$G\left(X_i\right) = \frac{1}{\left(\sigma\sqrt{2\pi}\right)^3} exp\left(\frac{-\left(\xi^2+\eta^2+\zeta^2\right)}{2\sigma^2}\right) \tag{4.4}$$

$$\int_{-\infty}^{\infty}\int_{-\infty}^{\infty}\int_{-\infty}^{\infty} G\left(X_i\right)dV = 1 \tag{4.5}$$

where $\xi = x_1 - X_1$, $\eta = x_2 - X_2$, and $\zeta = x_3 - X_3$.

In the limit $\sigma \to 0$, $G(X_i) = 0$ if $x_i \neq X_i$, and $G(X_i) = \infty$ if $x_i = X_i$. Thus, the Gaussian distribution can be seen as an approximation to the δ-distribution.

In discrete form, using the Gaussian distribution a velocity component u_b is determined as

$$u_b(X_i, t) = \sum_{l=h-1}^{h+1} \sum_{m=j-1}^{j+1} \sum_{n=k-1}^{k+1} G(X_i)\, u\left(x_1^l, x_2^m, x_3^n, t\right) \tag{4.6}$$

Here l, m, n represent indices of cells in the mesh near X_i in directions x, y, z. Point (h, j, k) corresponds to the fluid cell most near the IB-node X_i. Hence, the summation is done over the two nearest neighbors in each direction of the point (h, j, k). The sum is normalized in order to satisfy the condition of (4.5). Figure 4.2 illustrates the active nodes of summation in a plane. Note that staggering is not considered in the illustration.

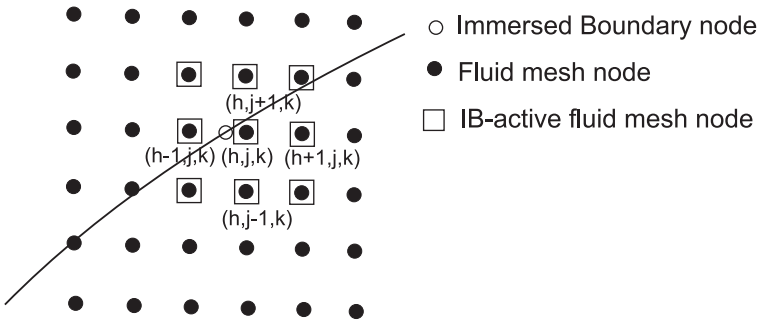

Figure 4.2: Immersed Boundary surface crossing the fluid mesh. Active fluid mesh-nodes are indicated by a square.

The next step is to estimate the force needed in order to satisfy the boundary condition. The discretized Navier-Stokes equations, including forcing terms may be written as

$$\frac{u_i^{n+1} - u_i^n}{\Delta t} = RHS_i^n + f_i^n \tag{4.7}$$

where RHS_i consists of the convective-, pressure-, and diffusive-terms, and where n indicates the old value from the previous iteration. A certain velocity v_i is wanted at the boundary. As RHS_i is already known, the f_i that is needed in order to obtain the v_i on the boundary at the next point in "time" (or pseudo-time, since several subiterations are done for each time step) is

$$f_i^{n+1} = -RHS_i^n + \frac{v_i^{n+1} - u_i^n}{\Delta t} \tag{4.8}$$

Here, the RHS-term has been dropped, since it does not improve convergence much, and instead a coefficient has been added before the time derivative, as well

as the force from the previous iteration. The force correcting the velocity defect is then given by

$$f_i^{n+1} = f_i^n + \alpha \frac{v_i^{n+1} - u_i^n}{\Delta t} \tag{4.9}$$

where $\alpha = \beta Re$. Re is the Reynolds number, and β is a relaxation term that is set for best performance. A large β gives faster adaptation to the boundary condition, but more oscillations. Increasing β to much leads to divergence, since even the smallest velocity defect causes large force terms, as compared to the other terms of the Navier-Stokes equations.

After the force has been estimated for each node it is transferred back to the same cells of the fluid mesh that the velocity was taken from, using the same Gauss distributed weights as in (4.6). However, since the IB-mesh is rather dense, many fluid cells will have contributions from more than one IB-node. Therefore, the force terms of the fluid mesh (F_f) are finally divided by the amount of contributions N, i.e. the force is expressed as

$$F(x_i, t) = \frac{1}{N} \sum_{s=1}^{N} F_f(x_i, t) \tag{4.10}$$

This force is then used for solving the system of equtaions of the fluid domain. The process is repeated several times for each time step, as described above.

The method of Gaussian weighted averaging gives a first order accurate solution, as shown by Revstedt et al. [154]. They also used a Lagrangian interpolation method for estimating the velocity at the IB-nodes. The results show approximately second order accuracy, however, the Gaussian average gave faster and more stable convergence, and the differences when comparing some relevant parameters were small. Therefore, the Gaussian method has been used here. Revstedt [153] also introduced a multi-grid method into the IB-force solver. He found substantial convergence acceleration for steady flows, and flows with rapid changes in the boundary conditions. For time dependent flows with stationary boundaries, the multi-grid solver only gave effect during the initial phase of the simulation. Here, a multi-grid solver has not been taken into account.

4.3 Solid Mechanics of Kirchhoff Plates

The second part of the FSI-solver is the structural solver, which is here implemented using the Finite Element Method (FEM). This section describes the solid mechanics theory used, and the derivation of the governing equations in weak form, used in the finite element formulation later. The FEM is further described in Chapter 5.

Since the aim with the implementation of the structural solver is to model FSI in and around pipes of small wall-thickness to radius ratio, such as in blood

vessels, the geometry is assumed to behave as a thin shell. In the finite element formulation the shell is built up of a set of Kirchhoff plates, which also have an in-plane stress state in the center-plane of each plate.

4.3.1 Governing equations

In Kirchhoff's plate theory (see Ottosen et al. [138] and Sundström [177]) the total deformation is determined by the deformation of the center plane of a plate of thickness t^s. Material points laying on a normal to the center plane, continue to lay on a normal line after deformation. Shear deformation is therefore neglected.

A coordinate system is introduced with the x–y-plane in the center plane and the z-axis normal to this surface. Figure 4.3 illustrates the plate with introduced vertical forces and moments. The plate is assumed to be loaded in the normal direction with the load p^s, and the resulting deflection w^s is positive in the positive z-direction. The superscript ^{s} means that the variable is referred to the solid, where similar letters are used for the fluid domain.

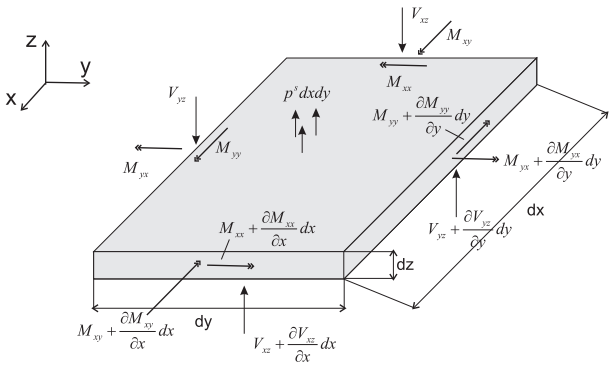

Figure 4.3: Plate with vertical forces, and moments.

The forces and moments per unit length are estimated as

$$V_{xz} = \int_{-t^s/2}^{t^s/2} \sigma^s_{xz} dz \tag{4.11}$$

$$V_{yz} = \int_{-t^s/2}^{t^s/2} \sigma^s_{yz} dz \tag{4.12}$$

$$N_{xx} = \int_{-t^s/2}^{t^s/2} \sigma^s_{xx} dz \tag{4.13}$$

$$N_{yy} = \int_{-t^s/2}^{t^s/2} \sigma^s_{yy} dz \tag{4.14}$$

$$N_{xy} = \int_{-t^s/2}^{t^s/2} \sigma_{xy}^s dz \tag{4.15}$$

$$M_{xx} = \int_{-t^s/2}^{t^s/2} z\sigma_{xx}^s dz \tag{4.16}$$

$$M_{yy} = \int_{-t^s/2}^{t^s/2} z\sigma_{yy}^s dz \tag{4.17}$$

$$M_{xy} = M_{yx} = \int_{-t^s/2}^{t^s/2} z\sigma_{xy}^s dz \tag{4.18}$$

Here a static description is made. Time derivatives will be added later.

Since the plate is assumed to be loaded in the transverse plane only, horizontal equilibrium requires $N_{xx} = N_{yy} = N_{xy} = 0$. Vertical equilibrium then requires

$$\frac{\partial V_{xz}}{\partial x} + \frac{\partial V_{yz}}{\partial y} + p^s = 0 \tag{4.19}$$

Moment equilibrium around lines parallell to the x- and y-axes, and where small quantities are neglected give

$$\frac{\partial M_{xy}}{\partial x} + \frac{\partial M_{yy}}{\partial y} = V_{yz} \tag{4.20}$$

$$\frac{\partial M_{xx}}{\partial x} + \frac{\partial M_{xy}}{\partial y} = V_{xz} \tag{4.21}$$

Differentiate (4.20) with respect to y and (4.21) with respect to x, and eliminate V_{xz} and V_{yz}. Combining the equations and cancelling small terms give

$$\frac{\partial^2 M_{xx}}{\partial x^2} + 2\frac{\partial^2 M_{xy}}{\partial x \partial y} + \frac{\partial^2 M_{yy}}{\partial y^2} + p^s = 0 \tag{4.22}$$

Consider a small displacement of one side of the plate, see Figure 4.4. Assuming neglected shear deformations, small deformations, and thereof small angles, and doing it similarly in the y-direction, the displacements in the x- and y-directions are

$$u^s = u_0^s - z\frac{dw^s}{dx} \tag{4.23}$$

$$v^s = v_0^s - z\frac{dw^s}{dy} \tag{4.24}$$

where $u_0^s(x, y)$, and $v_0^s(x, y)$ are the displacements of the center plane in the x- and y-directions, respectively, due to bending, and $w^s = w^s(x, y)$ is assumed to

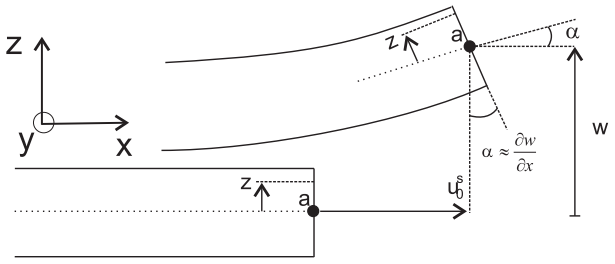

Figure 4.4: A plate subject to bending.

be independent of z. Assuming small deformations [106], the infinitesimal strain tensor is determined as

$$\epsilon_{ij}^s = \frac{1}{2}\left(\frac{\partial u_i^s}{\partial x_j} + \frac{\partial u_j^s}{\partial x_i}\right) \tag{4.25}$$

Expressing the components of (4.25), using (4.23) and (4.24), one has

$$\epsilon_{xx}^s = \frac{\partial u_0^s}{\partial x} - z\frac{\partial^2 w}{\partial x^2} \tag{4.26}$$

$$\epsilon_{yy}^s = \frac{\partial v_0^s}{\partial y} - z\frac{\partial^2 w}{\partial y^2} \tag{4.27}$$

$$\epsilon_{xy}^s = \frac{\partial u_0^s}{\partial y} + \frac{\partial v_0^s}{\partial x} - 2z\frac{\partial^2 w}{\partial x \partial y} \tag{4.28}$$

$\epsilon_{zz}^s = \epsilon_{xz}^s = \epsilon_{yz}^s = 0$, due to the previous assumptions.

It is further assumed that Hooks law is valid as constitutive relation of the material, as well as that the assumption of plane stress is applicable. The last assumption is valid because the plate is thin and σ_{xz}^s and σ_{yz}^s are small as compared to the other components, and therefore neglected. The constitutive equation is expressed as

$$\sigma_{ij}^s = C_{ijkl}\epsilon_{ij}^s \tag{4.29}$$

The fourth order tensor C_{ijkl} is for a linearly isotropic elastic solid reduced to two independent terms, λ^s and μ_l^s, which are the Lame's constants [106]. The stress tensor can then instead be expressed as

$$\sigma_{ij}^s = \lambda^s \epsilon_{kk}^s \delta_{ij} + 2\mu_l^s \epsilon_{ij}^s \tag{4.30}$$

The Lames constants are related to the more frequently used Young's modulus E^s, and the Poisson ratio ν^s as

$$E^s = \frac{\mu^s\left(3\lambda^s + 2\mu^s\right)}{\lambda^s + \mu^s} \tag{4.31}$$

$$\nu^s = \frac{\lambda^s}{2\left(\lambda^s + \mu^s\right)} \tag{4.32}$$

Assuming plane stress and using E^s and ν^s, the constitutive relation can be expressed in matrix form as $\sigma^{\mathbf{s}} = \mathbf{D}\epsilon^{\mathbf{s}}$, which corresponds to

$$\begin{pmatrix} \sigma^s_{xx} \\ \sigma^s_{yy} \\ \sigma^s_{xy} \end{pmatrix} = \frac{E^s}{1-\nu^{s2}} \begin{pmatrix} 1 & \nu^s & 0 \\ \nu^s & 1 & 0 \\ 0 & 0 & 1/2\left(1-\nu^s\right) \end{pmatrix} \begin{pmatrix} \epsilon^s_{xx} \\ \epsilon^s_{yy} \\ \epsilon^s_{xy} \end{pmatrix} \tag{4.33}$$

Under these assumptions it can be shown that there is no straining of the mid-plane, and therefore all terms on the RHS of (4.26)–(4.28), except the last term in each equation, are equal to zero. It can also be shown that the bending is driven by the vertical force, while the in-plane strain of the center plane, if present, is driven by the horizontal forces. Thus, the inplane deformation of the center plane, and the deformation due to bending are uncoupled, which makes it possible to superpose an independent plane stress deformation onto the center plane, as will be done here later.

Taking the center plane no-straining property into account and substituting (4.26)–(4.28) into (4.33), and the resulting stresses into (4.16)–(4.18), integrating and substituting into (4.22), one has

$$\frac{\partial^4 w^s}{\partial x^4} + 2\frac{\partial^4 w^s}{\partial x^2 \partial y^2} + \frac{\partial^4 w^s}{\partial y^4} = \frac{12\left(1-\nu^{s2}\right)}{E^s t^{s3}} p^s \tag{4.34}$$

This is a biharmonic equation that governs the deformation due to the normal load p^s. The expression

$$\frac{E^s t^{s3}}{12\left(1-\nu^{s2}\right)} \tag{4.35}$$

is often referred to as the bending stiffness, due to its correspondence to the bending stiffness of a beam (EI).

Now, the forces in the center plane will be considered. Force equilibrium of a continuum gives

$$\frac{\partial \sigma^s_{ij}}{\partial x_j} + b^s_i = 0 \tag{4.36}$$

Again, the plane stress assumption is made, so that $\sigma^s_{xz} = \sigma^s_{yz} = \sigma^s_{zz} = 0$, and that nothing depends on the z-coordinate. Therefore, forces are located in the x-y–plane, or more specifically in the center plane of the Kirchhoff plate. Once again infinitesimal deformations are assumed, as well as an isotropic- and elastic-material, and therefore (4.25) and (4.33) are valid also here. Thus, combining these equations would give a second order differential equation of the deformation components u^s and v^s.

4.3.2 Weak formulation

The governing equations may be written on a weak form. The advantage of writing the equations on weak form is that the order of spatial derivatives is reduced, i.e. the requirements on the approximation functions in the FEM-formulation are weaker. A consequence of this, as will be seen below, is that the test function needs to be differentiated instead. The weak form makes discontinuities easier to handle, and in combination with the Galerkin method the weak form yields a symmetric set of matrices in the finite element formulation, similar to when a variational approach is used [138, 152].

Now starting with (4.36) for the inplane motion. An arbitrary vector test or weight function v_i is multiplied to the expression (4.36), followed by integration over the volume V. As a dynamic problem will be considered here, time derivatives corresponding to acceleration and damping force are added to the expression. One thus has

$$\int_V v_i \frac{\partial \sigma_{ij}^s}{\partial x_j} dV + \int_V v_i b_i^s dV = \int_V v_i \rho^s \frac{\partial^2 u_i^s}{\partial t^2} dV + \int_V v_i \mu^s \frac{\partial u_i^s}{\partial t} dV \tag{4.37}$$

where μ^s is the damping coefficient of the material of interest, and b_i^s are body forces.

Due to the fact that for the general variables ϕ and q_i

$$\frac{\partial}{\partial x_i}(\phi q_i) = \phi \frac{\partial q_i}{\partial x_i} + q_i \frac{\partial \phi}{\partial x_i} \tag{4.38}$$

in combination with Gauss theorem, where S is the surface of the volume V and n_i is the normal to the surface,

$$\int_V \frac{\partial \phi}{\partial x_i} dV = \int_S \phi n_i dS \tag{4.39}$$

the Green-Gauss theorem is given by

$$\int_V \phi \frac{\partial q_i}{\partial x_i} dV = \int_S \phi q_i n_i dS - \int_V q_i \frac{\partial \phi}{\partial x_i} dV \tag{4.40}$$

Applying (4.40) to (4.37) one has

$$\int_V \sigma_{ij}^s \frac{\partial v_i}{\partial x_j} dV + \int_V v_i \rho^s \frac{\partial^2 u_i^s}{\partial t^2} dV + \int_V v_i \mu^s \frac{\partial u_i^s}{\partial t} dV = \int_V v_i b_i dV + \int_S v_i \sigma_{ij}^s n_j dS \tag{4.41}$$

As the problem here considered thin plates of constant thickness t^s, and where the variables are independent of z, one can integrate over the thickness of the

plate, i.e. from $-t^s/2$ to $t^s/2$, and have the expression in two dimensions. Since the traction vector $t_i^s = \sigma_{ij}^s n_j$, the expression for the plate center-case is

$$\int_S \sigma_{ij}^s \frac{\partial v_i}{\partial x_j} t^s dS + \int_S v_i \rho^s \frac{\partial^2 u_i^s}{\partial t^2} t^s dS + \int_S v_i \mu^s \frac{\partial u_i^s}{\partial t} t^s dS = \int_S v_i b_i^s t^s dS + \oint_L v_i t_i^s t^s dL \tag{4.42}$$

where L is the boundary around the center of the plate. The last term in (4.42) describes the natural- or Neumann-boundary conditions of the domain. The Essential- or Dirichlet-boundary conditions are applied later in the finite element formulation.

A similar procedure is applied to the plate bending equation (4.22), which is multiplied by the arbitrary test function $v = v(x, y)$ and integrated over the plate surface S. Time derivatives are added as well, however, the time derivative terms related to (4.20)–(4.21) are considered small in comparison to the time derivative terms related to (4.19), and therefore neglected. The angular velocities are still computed in the finite element solution, as spatial derivatives of w^s.

$$\begin{aligned}\int_S v \frac{\partial}{\partial x}\frac{\partial M_{xx}}{\partial x} dS + \int_S v \frac{\partial}{\partial x}\frac{\partial M_{xy}}{\partial y} dS + \int_S v \frac{\partial}{\partial y}\frac{\partial M_{xy}}{\partial x} dS \\ + \int_S v \frac{\partial}{\partial y}\frac{\partial M_{yy}}{\partial y} dS + \int_S v p dS = \int_V v \rho^s \frac{\partial^2 w^s}{\partial t^2} dV + \int_V v \mu^s \frac{\partial w^s}{\partial t} dV\end{aligned} \tag{4.43}$$

The time derivative terms are integrated over the volume, since vertical equilibrium requires integration over the thickness of the plate for the temporal terms.

By using the Green-Gauss theorem (4.40) twise and the relations (4.11), (4.12), (4.16)–(4.18), (4.20), (4.21), (4.43) can be expressed as (see Ottosen et al. [138] for details)

$$\begin{aligned}\int_S \left(\frac{\partial^2 v}{\partial x^2} M_{xx} + \frac{\partial^2 v}{\partial y^2} M_{yy} + 2 \frac{\partial^2 v}{\partial x \partial y} M_{xy} \right) dS - \int_V v \rho^s \frac{\partial^2 w^s}{\partial t^2} dV - \int_V v \mu^s \frac{\partial w^s}{\partial t} dV \\ = \oint_L \frac{dv}{dn} M_{nn} dL - \oint_L v \left(V_{nz} + \frac{dM_{nm}}{dm} \right) dL - \int_S v p dS\end{aligned} \tag{4.44}$$

where $\frac{d\phi}{dn} = \frac{\partial \phi}{\partial x_i} n_i$, and n and m are the normal and tangential unit vectors, respectively. The natural boundary conditions are therefore given by M_{nn} and $V_{nz} + \frac{dM_{nm}}{dm}$.

4.4 Coupling

The solution algorithm of the method chosen here can be divided into four parts:

1. solid solver
2. coupling: transfer of boundary data to fluid boundary
3. fluid solver
4. coupling: transfer of boundary data to solid boundary

The boundary conditions that are subject to the transfer process are the IB-motion, determined by the solid deformation, and the forces on the wall determined by the fluid flow. Mathematically the boundary conditions can be expressed as

$$t_i = \sigma^s_{ij} n_j = \sigma_{ij} n_j, \quad t_i \in \Gamma^s, \quad \sigma_{ij} \in \Gamma^f \tag{4.45}$$

$$\frac{\partial u^s_i}{\partial t} = u_i, \quad u^s_i \in \Gamma^s, \quad u_i \in \Gamma^f \tag{4.46}$$

where σ_{ij} is the fluid stress tensor, n_j is the boundary normal into the fluid domain, t^s_i is the traction vector on the solid boundary, σ^s_{ij} is the solid stress tensor, u^s_i is the displacement of the solid boundary, and u_i is the velocity boundary condition that the fluid near the wall must adapt to.

As the structural mesh is coarser than the IB-mesh, the velocities obtained by the solid solver need to be interpolated to the IB-nodes. First an algorithm identifies which IB-node belongs to which finite element. Then the velocity data from the finite elements is linearly interpolated to all IB-nodes belonging to each particular finite element, respectively. Hence, v^{n+1}, is updated for all nodes and solved for.

The forces to be transferred to the solid boundary are determined from the force source terms F_i. The rationale is that the force needed to uphold the wall boundary condition, is the force a solid wall would experience. Therefore, the shortest distance h between two adjacent finite element nodes is estimated. Thereafter, all force (source) terms of the fluid mesh, in a sphere with radius $r < h/2$ around each finite element node, are integrated . This directly gives the contribution of all three force components to the boundary forces of each finite element node. Hence, the force experienced by a finite element node is expressed as

$$F^s_i = \int_{r<h/2} F_i dV \tag{4.47}$$

where F^s_i is the force component i used as load force in the solid solver.

Chapter 5

Numerical Methods

The governing equations of fluid mechanics are non-linear and the range of flows that they describe is very wide and highly different (e.g. laminar or turbulent, steady or unsteady, etc.) The system of PDE's has a closed analytical solution only for a few simple cases and where the non-linearity effects are negligible. Examples of these kind of flows are Stokes flow, Couette flow and Poiseuille flow. These flows are not considered here, but are easily found in any undergraduate text on fluid mechanics [203]. At the flow regimes that are considered here, the non-linear effects are important and hence no analytical solutions can be found.

Numerical methods can handle non-linear problems almost as easily as linear ones. Numerical schemes for solving the Navier-Stokes equations under very different conditions are available and nowadays these methods are efficient. The improvement of computational power enables one to obtain results with better resolution, and enabling a better assessment of the accuracy of the numerical computations. However, there are inherent uncertainties associated with flow computations. A major issue is always setting relevant (or accurate) boundary conditions. In particular if the numerical results are to be compared to experimental data, the boundary conditions have to be the same as those in the experiments. Otherwise, such comparisons are of qualitative value and this is the reason for the large number of "validation" projects. Nevertheless, one can state that there are generally "valid" computational codes, though the level of accuracy may depend on the particular case and the level of detail in the discrete approximations. Another issue is related to modeling of certain phenomena such as turbulence, rheological properties of the fluid, etc. These models introduce new errors (modeling errors) that should not be mixed with the other two mentioned first (i.e. the discretization errors and the uncertainties in boundary conditions).

The uncertainties in the computational set-up lead to the need of experimental support to the computations. In addition to direct comparison with experiments, it is important that one carries out multiple computations to assess the sensitivity of the results to different parameters; numerical (resolution), geometrical (shape and size) and physical (Re, α, and boundary conditions).

5.1 Computational Fluid Dynamics, CFD

In numerical simulations, or as it is being referred to in the context of fluid mechanics, Computational Fluid Dynamics (CFD), the governing equations of fluid mechanics, the Navier-Stokes equations and the continuity equation, are solved numerically. Thus, the system of PDE's is discretized in space (and time) on a discrete number of points. Thereby the continuous system of partial differential equations becomes a system of algebraic equations of finite size. The number of dependent variables in the algebraic system equals the number of points in space times the number of dependent variables in the original system. The algebraic equations are solved through an appropriate computational algorithm.

The major components of the most common CFD-approaches are:

- The computational domain is divided into a large number of small volumes. The size of the computational volumes determine the spatial resolution of the computed results. The shape of the small volumes may vary. Most often one uses hexahedral or tetrahedral shaped (control) volumes. Other shapes can equally be used. The total set of control volumes form a mesh (or grid). If only spatial discretisation is done, one obtains a set of ordinary differential equation (in time), which has to be integrated. Alternatively, one also discretize with respect to time.

- The derivatives in space (and time) of all variables are then discretized on the grid using an approximation scheme of a certain order. Higher order schemes require that a larger number of grid points are involved. This forms a discrete system of equations.

- The discrete system of equations is then solved with an appropriate numerical scheme.

The most common discretization schemes used in engineering are Finite Volumes (FVM), Finite Elements (FEM), and Finite Differences (FD). All these approaches have been used in this work and are described shortly in the following.

5.2 Discretizing the Flow Equations

The Navier-Stokes equations and the continuity equation are discretized by either finite-differences or finite-volumes. In some cases (Cartesian grids and certain central differences) these two schemes are identical.

5.2.1 Finite difference method

For the fluid part of the FSI-solver a Finite Difference (FD) scheme has been used in combination with an Immersed Boundary (IB) solver. The IB-method has been described in Chapter 4.

In the FD-method the derivatives of the continuity- (3.7), and the Navier-Stokes-equations (3.10), are discretized directly on a structured mesh; here a fixed Cartesian mesh is used. The discretization process results in an algebraic system of equations, which is then solved using a suitable method.

The solver uses a staggered grid-formulation. The velocity components are specified on the cell-surfaces with normals in the direction of each velocity component, respectively. The same staggered grid formulation is used for the distribution of forces. The pressure term is specified in the cell center. Figure 5.1 illustrates the locations of the different components in each cell. A staggered grid avoids un-physical pressure oscillations in the solution [58]. A Cartesian grid has the advantages that it is rather easy to apply discretization schemes, it is easier to achieve high accuracy, and that the computational cost is lower as compared to a curvelinear or unstructured grid [58]. A disadvantage is that it may be difficult to represent complex boundaries accurately.

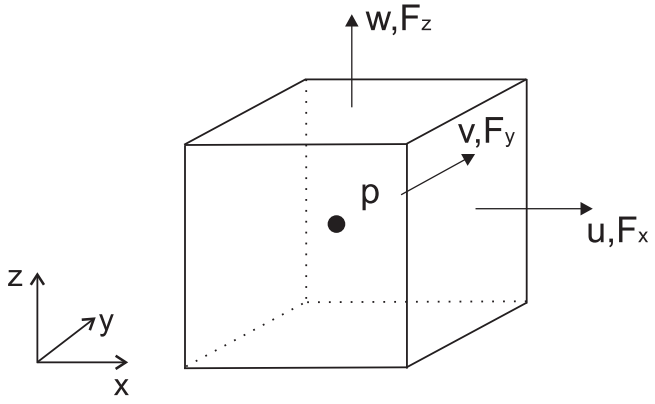

Figure 5.1: Discretized components on staggered grid.

Discretization schemes

A three level second order backward (implicit) scheme is used for the time derivatives [4], and given by

$$\frac{\partial \phi}{\partial t} \approx \frac{3\phi^{n+1} - 4\phi^n + \phi^{n-1}}{2\Delta t} \tag{5.1}$$

For the diffusive terms a fourth order central difference scheme is employed, the pressure gradient is discretized using a fourth order forward difference scheme. The convective terms are discretized using a third-order upwind scheme, as proposed by Rai and Moin [150], and given by

$$u_i \frac{\partial \phi}{\partial x} \approx \begin{cases} u_i \frac{2\phi_{i+1}+3\phi_i-6\phi_{i-1}+\phi_{i-2}}{6h}, & u_i > 0 \\ u_i \frac{2\phi_{i-1}-3\phi_i+6\phi_{i+1}-\phi_{i+2}}{6h}, & u_i < 0 \end{cases} \tag{5.2}$$

Solver

The solver is using a multi-grid approach and a Gauss-Seidel scheme as smoother. Pressure corrections are obtained from a Poisson equation, also relaxed using a Gauss-Seidel iteration scheme. The grids used for the multi-grid acceleration are successively finer, where the cell size for each generation of grids is reduced by one half.

As Revstedt and Fuchs [154] showed the combined FD-IB solver is mainly limited in accuracy by the IB-part of the solution proceedure, where also the method used here was shown to be first order accurate.

Directly applying a high order discretization scheme may lead to a less robust and less efficient solver. Instead, introducing a single step defect correction algorithm, where lower order discretizations are combined with higher order, improves the accuracy to that of the higher order schemes. Here the high order schemes are given in the previous section, while the lower order schemes are a first order forward scheme for the pressure term, first order upwind for the convective terms, and a second order central scheme for the diffusive terms. The defect correction approach takes advantage of the accuracy of the high order schemes and the stability of the more diffusive first order schemes. It also converges faster as compared to applying a high order scheme directly [78].

The problem to be solved is

$$L\phi = f \tag{5.3}$$

where L is the operator representing the derivatives of the Navier-Stokes equations, ϕ is the solution and f a source term. Given ϕ^n, one solves for ϕ^{n+1} as

$$L_{lo}\phi^{n+1} = f + L_{lo}\phi^n - L_{ho}\phi^n \tag{5.4}$$

where L_{ho} denotes the high order discretized derivatives of the Navier-Stokes equations. The superscript ^{n} gives the iteration number and $\phi = \phi(u, v, w, p)$. The iteration process is repeated until the difference $L_{lo}\phi^{n+1} - L_{lo}\phi^n$ is sufficiently

small. Then the solution for the high order discretization problem $L_{ho}\phi = f$ is achieved. For more on defect correction, see Gullbrand et al. [78].

5.2.2 Finite volume method

Using the finite volume method the governing equations are integrated over each element. The momentum equations become then:

$$\int_V \rho\frac{\partial u_i}{\partial t}dV + \int_V \rho\frac{\partial}{\partial x_j}u_i u_j dV = -\int_V \frac{\partial p}{\partial x_i}dV + \int_V \mu\frac{\partial^2 u_i}{\partial x_j \partial x_j}dV \tag{5.5}$$

Applying Gauss divergence theorem to (5.5) yields

$$\int_V \rho\frac{\partial u_i}{\partial t}dV + \int_S \rho u_i u_j n_j dS = -\int_S p n_i dS + \int_S \mu\frac{\partial u_i}{\partial x_j}n_j dS \tag{5.6}$$

V is the volume of each element, S is the surface enclosing the volume and n_i is the outward pointing normal.

In a similar manner the continuity equation is given by

$$\int_S u_i n_i dS = 0 \tag{5.7}$$

The equations are then discretized into the following two expressions, where superscript ^{f} shows that a parameter is taken from a face of the element.

$$\rho\frac{\partial u_i}{\partial t}V_{elem} + \sum_{f=1}^{N_{faces}} \rho u_i^f u_j^f n_j^f S^f = -\sum_{f=1}^{N_{faces}} p^f n_i^f S^f + \sum_{f=1}^{N_{faces}} \mu\frac{\partial u_i}{\partial x_j}n_j^f S^f \tag{5.8}$$

$$\sum_{f=1}^{N_{faces}} u_i^f n_i^f S^f = 0 \tag{5.9}$$

V_{elem} is the element volume, and N_{faces} is the number of faces enclosing an element.

Here a collocated grid scheme is used. Thereby all dependent variables and parameters are given at the same location (5.8) and (5.9).

The discretization in time may be of different types; here an implicit second order accurate scheme is used, which is given in equation (5.16). The discrete set of algebraic equation has to be solved in each time step. The marching in time leads finally to a temporally resolved solution. Different approaches may be adopted when solving the non-linear problem in each time-step. One may solve all the linearized equations at once, or using a Newton method in the non-linear case [58]. Another (so called segregated) approach is to solve each of

the governing equations in turn. This approach may require re-visiting some of the equations before adequate accuracy (to ensure convergence of the iterative process) is attained. Here, a segregated solution method is used (in each time-step), which means that the governing equations are solved sequentially. Further details are given below.

Convection and pressure terms

The convection terms, as shown in (5.8), contain cell face parameters and interpolation is therefore needed. The software offers different kinds of upwind schemes for this task. Here a second order upwind scheme is chosen (or in some cases the Quick scheme [59]), and it is given by

$$\phi^f = \phi + \nabla\phi \cdot \mathbf{r} \tag{5.10}$$

where ϕ and $\nabla\phi$ are cell centre values from the upstream cell, and $\mathbf{r}$ is the displacement vector from the upstream cell centroid to the face centroid.

The gradient of parameter ϕ can according to the divergence theorem be written as

$$\nabla\phi = \lim_{\Delta V \to 0} \frac{1}{\Delta V} \int_S \phi n dS \tag{5.11}$$

which in discrete form yields

$$\nabla\phi = \frac{1}{V_{elem}} \sum_{f=1}^{N_{faces}} \phi_{ave}^f S^f \tag{5.12}$$

where ϕ_{ave}^f is the average of ϕ from the two cells adjacent to the face. This is the general method used for computing gradients in the FVM-solver used [59].

The QUICK scheme is based on a weighted average of a second order upwind scheme and a second order central scheme. If ϕ is wanted on face e, between cell E and P and downstream of cell P and W, we have

$$\begin{aligned} \phi_e = \theta \left[\tfrac{S_E}{S_E+S_P}\phi_P + \tfrac{S_P}{S_E+S_P}\phi_E \right] + \\ (1-\theta) \left[\tfrac{S_W+2S_P}{S_W+S_P}\phi_P - \tfrac{S_P}{S_W+S_P}\phi_W \right] \end{aligned} \tag{5.13}$$

where S_i is the length of element i and θ is a constant varying between 0–1. When $\theta = 1$ (5.13) corresponds to a second order central difference scheme, and when $\theta = 0$ it corresponds to a second order upwind scheme. In the software θ varies depending on the characteristics of the solution.

Diffusion terms

For the diffusion terms a central difference scheme has been used, which is second order accurate. The face value of, say, parameter ϕ^f is given by

$$\phi^f = \frac{1}{2}(\phi_0 + \phi_1) + \frac{1}{2}(\nabla\phi_0 \cdot \mathbf{r}_0 + \nabla\phi_1 \cdot \mathbf{r}_1) \tag{5.14}$$

where the indices 0 and 1 are the two cells sharing the face f and $\mathbf{r}$ is the vector from the cell centroid to the face centroid.

Temporal terms

The temporal terms are discretized using a second order backward scheme. If the equation for one variable ϕ is written as

$$\frac{\partial\phi}{\partial t} = F(\phi) \tag{5.15}$$

the discretized form can be written as

$$\frac{3\phi^{n+1} - 4\phi^n + \phi^{n-1}}{2\Delta t} = F(\phi) \tag{5.16}$$

where $n+1$ is the value at $t + \Delta t$, n at t and $n-1$ at $t - \Delta t$. The time level used for the spatial terms, i.e. in $F(\phi)$, decides whether the method is explicit or implicit. Here an implicit formulation has been chosen, so the equation can be written as

$$\phi^i = 4/3\phi^n - 1/3\phi^{n-1} + 2/3\Delta t F\left(\phi^i\right) \tag{5.17}$$

This equation is then being solved iteratively, and once convergence is reached ϕ^i is set equal to ϕ^{n+1}. Implicit formulation gives an unconditionally stable method with respect to time step size, however, we are still limited by physical constraints. The CFL number is defined as $CFL = \frac{u_{loc}\Delta t}{\Delta x}$, where u_{loc} is the local speed at the particular element of interest, Δt is the time step size and Δx is the element size. For a CFL number above one the propagation length $u_{loc}\Delta t$ is larger than the element length Δx, which means that the numerics might miss information about the flow.

Another restriction is the limitation of the grid to resolve a periodic motion of period T. If u_{loc} is the local flow speed and Δx the distance between two grid points, the smallest period that can be resolved is $T = \frac{2\Delta x}{u_{loc}}$, since at least three points are needed in order to resolve a sinusoidal fluctuation. A time step smaller than T is then required in order to resolve this frequency.

Solver

The non-linear part of the equations are linearized, resulting in a system of linear equations with one equation for each cell in the domain. A Gauss-Seidel solver (smoother) is then used in conjunction with a multi-grid method to solve the system of equations. One may use a non-linear solver in conjunction with the multi-grid solver by using the so called Full Approximation Storage (FAS) [68].

5.2.3 Gauss-Seidel method

The Gauss-Seidel method is an iterative way of solving system of equations. Applied to a general system $Ax = b$ the Gauss-Seidel scheme can be written as

$$x_i^{k+1} = \frac{1}{a_{ii}} \left(b_i - \sum_{j=1}^{i-1} a_{ij} x_j^{k+1} - \sum_{j=i+1}^{n} a_{ij} x_j^k \right) \tag{5.18}$$

where super-script ^{k} refers to the previous iteration level and $^{k+1}$ to the same level, for those terms that have already been estimated [83]. The method requires that the matrix of the system of equations is diagonally dominant. Tannehill et al. [183] describe the solution procedure as:

1. Make initial guess for all unknowns (not needed for one value, which is given from the other values).

2. Solve each equation for the unknown, whose coefficient is largest in magnitude, using guessed values initially and the most recently computed values thereafter.

3. Repeat this procedure iteratively until sufficient convergence is attained.

5.2.4 Multi-grid method

The multi-grid method is used to accelerate the solver, which otherwise becomes very slow at a large number of elements. The Gauss-Seidel scheme efficiently reduces the local high frequency errors in the solution, while the more global low frequency errors are reduced at a rate inversely related to the number of cells [59, 83, 91]. Therefore, such an iterative scheme is often referred to, and used as, a smoother.

The idea with the multi-grid technique is that the solution, usually after some smoothing iterations, still contains low frequency errors. The residual is then mapped (*restriction*) to and used in the smoothing on a coarser grid, where the previous low frequency error now, relative to the larger element size, is a high frequency error. The Gauss-Seidel scheme is then used at the coarser level to eliminate these errors. The process continues for a sufficient amount of coarser

grids. When the coarsest grid is reached the solution on that is mapped back (*prolongation*) to a finer grid, where more relaxation takes place, again using the Gauss-Seidel scheme. When we finally end up at the initial grid again a converged solution is hopefully reached, otherwise another sequence is initiated [59, 183].

The process is described mathematically as follows: The discretized equation is given by

$$A\phi_e + b = 0 \tag{5.19}$$

where A is the coefficient matrix, ϕ_e is the exact solution and b are constants. The approximate solution ϕ will contain a residual d and is given by

$$A\phi + b = d \tag{5.20}$$

A correction ψ to ϕ yields $\phi_e = \phi + \psi$, and with (5.19) and (5.20) we have

$$\begin{gathered} A(\phi + \psi) + b = 0 \\ A\psi + A\phi + b = 0 \\ A\psi + d = 0 \end{gathered} \tag{5.21}$$

The correction is then given by the initial coefficient matrix A, and the residual is given after the initial sweeps, that reduced high frequency errors. In order to solve for the correction term, containing more low frequency errors, the residual is interpolated to a coarser level (*restriction*), where now the relation is expressed as

$$A^c\psi^c + Rd = 0 \tag{5.22}$$

where A^c is the coefficient matrix of the coarser level, ψ^c will be the solution on the coarser level after smoothing, and R is the restriction operator. After a sufficient amount of coarse grid levels, the process changes direction and the solution on the coarser level is transferred to a finer level (*prolongation*), which can be expressed as

$$\phi^{new} = \phi + P\psi^c \tag{5.23}$$

where P is the prolongation operator, and where some more smoothing take place. There are several different commonly used cycles of the multi-grid process. Two of them are the V and the W cycle, which are shown in Figure 5.2.

In the case of a non-linear problem the Full Approximation Storage (FAS) approach is considered instead, where also the approximate solution needs to be restricted onto coarser grids [58].

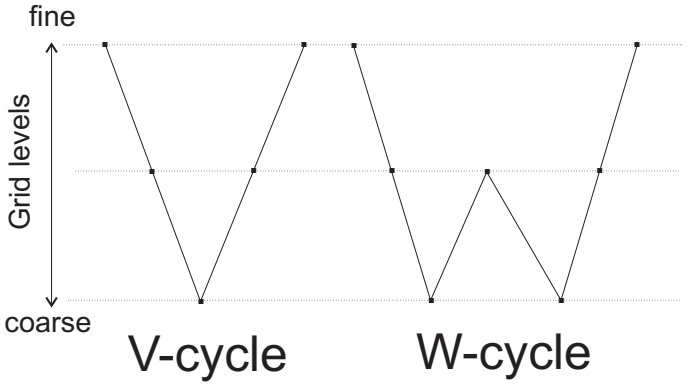

Figure 5.2: Examples of multigrid cycles; the V-cycle to the left and the W-cycle to the right. After Heath [83].

5.2.5 Pressure-velocity coupling using PISO

Due to the usage of a segregated approach the computed dependent variables do not satisfy both the momentum- and the continuity-equations, just after updating the momentum equations. In order to compensate for this error, a pressure-correction scheme is used. The momentum equations are first solved using an estimated pressure, and if the resulting velocity field does not satisfy continuity, pressure is also updated so that the continuity equation is satisfied, while the approximation of the momentum equation remains un-affected [183]. The procedure is initiated with the predictor step as

$$\frac{\rho}{\Delta t}\left(u_i^* - u_i^n\right) = H\left(u_i^*\right) - \Delta_i p^n \tag{5.24}$$

where p^n and u_i^n are the values at the previous time level, or the initial pressure and velocity field, respectively. The operator H is the convective and diffusive terms in discretized form, and Δ_i is the gradient in discretized form. Generally, continuity will not be satisfied after this *predictor* step, so this is followed by a *corrector* step, which reads

$$\frac{\rho}{\Delta t}\left(u_i^{**} - u_i^n\right) = H\left(u_i^*\right) - \Delta_i p^* \tag{5.25}$$

In this step continuity, $\Delta_i u_i^{**}$, is required, and both the pressure p^* and the revised velocity u_i^{**} is sought. Now, taking the divergence of (5.25) we have

$$\Delta_i^2 p^* = \Delta_i H\left(u_i^*\right) + \frac{\rho}{\Delta t}\Delta_i u_i^n \tag{5.26}$$

which is a discretized Poisson equation. Solving this equation yields p^*, which then is put into (5.25) and which gives u_i^{**}. By definition this satisfies the continuity equation. Several re-corrector steps may then also be performed by doing the same correction procedure again, depending on the requirements on convergence.

It should be pointed out that different versions of pressure-velocity coupling schemes exist, depending on the flow character that is often used to guide in making an assumption on the behavior of the pressure-velocity correction.

5.3 Finite Element Method for Solid Deformation

The equations governing the structural deformations were given in Chapter 4, and are repeated here, for convenience, in their weak forms as

$$\int_S \sigma_{ij}^s \frac{\partial v_i}{\partial x_j} t^s dS + \int_S v_i \rho^s \frac{\partial^2 u_i^s}{\partial t^2} t^s dS + \int_S v_i \mu^s \frac{\partial u_i^s}{\partial t} t^s dS = F_{horizontal}^s \tag{5.27}$$

$$\int_S \left(\frac{\partial^2 v}{\partial x^2} M_{xx} + \frac{\partial^2 v}{\partial y^2} M_{yy} + 2 \frac{\partial^2 v}{\partial x \partial y} M_{xy} \right) dS - \int_V v \rho^s \frac{\partial^2 w^s}{\partial t^2} dV - \int_V v \mu^s \frac{\partial w^s}{\partial t} dV = F_{vertical}^s \tag{5.28}$$

where $F_{horizontal}^s$ and $F_{vertical}^s$ act in the tangential plane, and normal, to the element in question, respectively.

In the Finite Element Method (FEM) the field variables are approximated using some kind of piecewise approximation function, usually polynomials, over each element. The order of the polynomial is determined by the element shape, the number of nodes of the element, and the number of degrees of freedom per node. Also, the order of the polynomial determines, if it is complete, the order of accuracy of the discretization. For an incomplete polynomial, i.e. where not all terms of a specific order are included, the truncation error is determined by the lowest order term. The polynomial is chosen so that each point inside each element can be expressed as a function of the values of the nodes, respectively.

Here, the FEM has been used for solving the structural deformation of the cylindrical geometry, whereas an FD approach (described later) has been used for the fluid part of the FSI-problem considered.

The idea of the finite element formulation is to find a solution of a problem that minimizes the total potential energy functional, using a variational formulation, or to find a weight function v that minimizes the integral of the residual of the approximate solution of a system of equations. The latter approach is termed the Weighted Residual approach, and it has been used here.

The weight function can be expressed as a linear combination of base functions, $v = \sum_{i=1}^{N} c_i \psi_i$, where N is the number of base functions used. The Galerkin method states that the weight function that minimizes the integral of the residual of the system of equations has the same set of base functions as the base

which is used for the approximation of the field variables. Mathematically this can generally be expressed in one dimension as

$$\int_a^b \psi_i e dx = 0, \quad i = 1, ..., N \tag{5.29}$$

where ψ_i is the base also chosen for the approximation function, and e is the error of the differential equation. It is now rather obvious why the weak formulation is very convenient for formulating the finite element description. For other minimization methods, see Ottosen et al. [138] or Rao [152].

With that given, the rest of the process of building the finite element description chosen, and computing the solution follows as:

1. Define the element, the degrees of freedom and the approximating polynomials for the in-plane-, as well as the bending-descriptions.

2. Substitute the approximation into each weak formulation of the problem, respectively, and build the system matrices.

3. Assemble the local matrices into the global system matrices after coordinate transformation.

4. Apply the Essential or Dirichlet boundary conditions to the global system matrices.

5. Solve the resulting system of (ordinary differential) equations.

As the finite element method uses a set of "finite elements" to describe a geometry, the thin walled geometry here has been chosen to be described by a set of Kirchhoff plates, including center in-plane deformation for shear forces. The solid mechanics theory of Kirchhoff plates was described in a previous chapter.

For simplicity, simple triangular elements have been chosen for approximation. A sketch of a triangular element with its degrees of freedom for the in-plane, and bending descriptions, is shown in Figure 5.3. The formulation is first described for the in-plane motion, followed by the description of the bending motion.

5.3.1 Plane stress of triangular element

A coordinate system is defined as shown in Figure 5.3, this is a local coordinate system valid for all finite elements, related to the global coordinate system through a matrix of direction cosines [152]. For the in-plane formulation there are three nodes and two degrees of freedom per node, i.e. six unknowns. Therefore, 2D linear approximation polynomials, with six unknown constants, are used and written as

$$u^s(x, y) = \alpha_1 + \alpha_2 x + \alpha_3 y \tag{5.30}$$

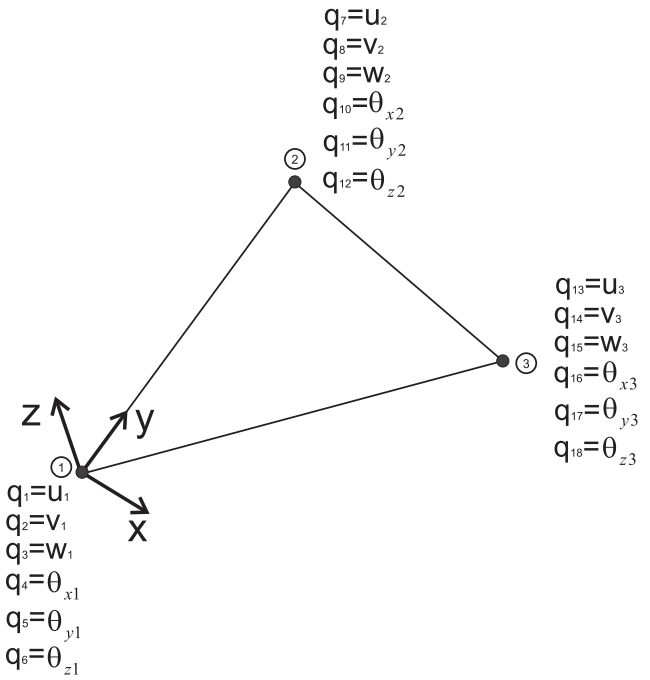

Figure 5.3: Triangular element.

$$v^s(x,y) = \alpha_4 + \alpha_5 x + \alpha_6 y \tag{5.31}$$

The six degrees of freedom q_i are given by:

$$u_1^s = q_1 \quad v_1^s = q_2 \tag{5.32}$$
$$u_2^s = q_3 \quad v_2^s = q_4 \tag{5.33}$$
$$u_3^s = q_5 \quad v_1^s = q_6 \tag{5.34}$$

where the subscript of u^s now referrers to the local node number. Each node is also given a unique global node number, that is used later for the global assembling process.

The expressions of (5.30)–(5.34) can now be written in matrix form as

$$\mathbf{U} = \begin{pmatrix} u^s(x,y) \\ v^s(x,y) \end{pmatrix} = \boldsymbol{\Upsilon}\boldsymbol{\Theta} \tag{5.35}$$

Hence, $\boldsymbol{\Upsilon}$ is the matrix of the base functions

$$\boldsymbol{\Upsilon} = \begin{pmatrix} 1 & x & y & 0 & 0 & 0 \\ 0 & 0 & 0 & 1 & x & y \end{pmatrix} \tag{5.36}$$

and $\boldsymbol{\Theta}$ is the vector of unknown coefficients

$$\boldsymbol{\Theta} = \begin{pmatrix} \alpha_1 \\ \vdots \\ \alpha_6 \end{pmatrix} \tag{5.37}$$

Using the fact that in the nodes one has (5.32)–(5.34), so that

$$\mathbf{q} = \mathbf{\Lambda\Theta} \tag{5.38}$$

where

$$\mathbf{\Lambda} = \begin{pmatrix} \mathbf{\Upsilon_1} \\ \mathbf{\Upsilon_2} \\ \mathbf{\Upsilon_3} \end{pmatrix} \tag{5.39}$$

$$\mathbf{q} = \begin{pmatrix} q_1 \\ \vdots \\ q_6 \end{pmatrix} \tag{5.40}$$

and where the subscript on $\mathbf{\Upsilon}$ states the local nodenumber, one has

$$\mathbf{U} = \begin{pmatrix} u^s(x,y) \\ v^s(x,y) \end{pmatrix} = \mathbf{\Upsilon\Lambda^{-1}q} = \mathbf{Nq} \tag{5.41}$$

$\mathbf{N}$ is the matrix of shape functions, i.e. the polynomial approximations of the field variables over the element are now related to the unknown degrees of freedom of each node.

The strain tensor is given by (4.25). By reducing to two dimensions the strain relations may be expressed as

$$\epsilon^{\mathbf{s}} = \begin{pmatrix} \epsilon_{xx} \\ \epsilon_{yy} \\ \epsilon_{xy} \end{pmatrix} = \begin{pmatrix} \partial u^s/\partial x \\ \partial v^s/\partial y \\ \partial u^s/\partial y + \partial v^s/\partial x \end{pmatrix} \tag{5.42}$$

Using (5.41) and performing the derivations on the shape functions the strain can be expressed as

$$\epsilon_{2D} = \mathbf{Bq} \tag{5.43}$$

where $\mathbf{B}$ contains the differentiated shape functions.

Further, $\sigma^s = \mathbf{D}\epsilon^s = \mathbf{DBq}$, where $\mathbf{D}$ is given in (4.33), and the use of the Galerkin formulation suggests that the arbitrary test functions are expressed as $v_i = \mathbf{Nc}$, where $\mathbf{c}$ is arbitrary. Using these relations in (4.42), where $\mathbf{c}$ will cancel, give

$$\mathbf{k^{(e)_1}} = t^s \iint_{S^e} \mathbf{B^T DB} dS \tag{5.44}$$

$$\mathbf{m^{(e)_1}} = t^s \rho^s \iint_{S^e} \mathbf{N^T N} dS \tag{5.45}$$

$$\mathbf{c^{(e)_1}} = t^s \mu^s \iint_{S^e} \mathbf{N^T N} dS \tag{5.46}$$

The force terms on the RHS of (4.42) do not need to be considered. Instead of having a traction field and/or a body force field and integrate those functions over the boundary and domain, to distribute the forces to the nodes, the force vector is estimated directly at each node, respectively. This procedure is described in Chapter 4, and indicated in (5.27). From a three dimensional perspective all nodes are boundary nodes, and one then would have only boundary forces. Although, viewing the axial-azimuthal plane in two dimensions, the top and bottom of the cylinder are boundaries, while the other nodes are internal. Then the force field can be seen as consisting of both boundary- and body-forces. In practise this does not matter, the resulting force field is here the same given by (4.47).

5.3.2 Triangular plate bending element

When it comes to the bending part of the problem the process of obtaining the finite element description is rather similar to what was described in the previous section. The largest difference is that a higher order polynomial is used, as there are more degrees of freedom, and as there are higher order derivatives in the governing equations (compare (4.42) and (4.44)).

There are three degrees of freedom in each node, which give nine degrees of freedom in total per element; these are also shown in Figure 5.3. The polynomial therefore has nine constants and is given by

$$w^s(x,y) = \alpha_1 + \alpha_2 x + \alpha_3 y + \alpha_4 x^2 + \alpha_5 xy + \alpha_6 y^2 + \alpha_7 x^3 + \alpha_8 \left(x^2 y + xy^2\right) + \alpha_9 y^3 \tag{5.47}$$

The base of the eighth term assures completeness and symmetry of the expression.

As before the expression above can be written on matrix form as $\mathbf{\Upsilon_b \Theta_b}$. The subscript $_b$ referres to the bending part of the FEM-formulation.

$$\mathbf{\Upsilon_b} = \begin{pmatrix} 1 & x & y & x^2 & xy & y^2 & x^3 & (x^2y + xy^2) & y^3 \end{pmatrix} \tag{5.48}$$

$$\mathbf{\Theta_b} = \begin{pmatrix} \alpha_1 \\ \vdots \\ \alpha_9 \end{pmatrix} \tag{5.49}$$

The degrees of freedom are further expressed as

$$w_1^s = q_1 \quad \frac{\partial w_1^s}{\partial y} = \theta_{x_1} = q_2 \quad -\frac{\partial w_1^s}{\partial x} = \theta_{y_1} = q_3 \tag{5.50}$$

$$w_2^s = q_4 \quad \frac{\partial w_2^s}{\partial y} = \theta_{x_2} = q_5 \quad -\frac{\partial w_2^s}{\partial x} = \theta_{y_2} = q_6 \tag{5.51}$$

$$w_3^s = q_7 \quad \frac{\partial w_3^s}{\partial y} = \theta_{x_3} = q_8 \quad -\frac{\partial w_3^s}{\partial x} = \theta_{y_3} = q_9 \tag{5.52}$$

where the angular deformations θ_x and θ_y are rotations around the x- and y-axes, respectively. The negative sign before the rotations around the y-axis is to make sure that a positive movement in the x-direction corresponds to a positive displacement of w^s. The angular deformations may be referred to as generalized deformations, and similarly their corresponding moments may be referred to as generalized forces. The subscript number referrers to the local node number.

The procedure of (5.38)–(5.41) also applies to the formulation of the bending of the plate; only that the matrices with subscript $_b$ are used where it applies. The corresponding expression for (5.41) is here (where the out of plane horizontal deformation due to bending is neglected)

$$w^s(x,y) = \mathbf{\Upsilon_b \Lambda_b^{-1} q_b} = \mathbf{N_b q_b} \tag{5.53}$$

Further, since there are no resulting in-plane forces in the bending part of the description, (4.26)–(4.28) can be written as

$$\epsilon_b^s = z \begin{pmatrix} -\frac{\partial^2 w}{\partial x^2} \\ -\frac{\partial^2 w}{\partial y^2} \\ -2\frac{\partial^2 w}{\partial x \partial y} \end{pmatrix} \tag{5.54}$$

Substituing (5.53) into (5.54) and doing the differentiations, the strains may be expressed as

$$\epsilon_b^s = z\mathbf{B_b q_b} \tag{5.55}$$

where $\mathbf{B_b}$ contains the differentiated shape functions.

Further, substituting (5.55) into (4.33), one gets expressions for the stresses. These are then integrated using (4.16)–(4.18), before they can be put into (5.28).

The test function v is here written as $v = \mathbf{c_b N_b}$, and again $\mathbf{c_b}$ cancels.

Substituting these expressions into (5.28) the expressions for the stiffness, mass, and damping matrices are

$$\mathbf{k^{(e)_2}} = \frac{t^{s3}}{12} \iint\limits_{S^e} \mathbf{B_b^T D B_b} dS \tag{5.56}$$

$$\mathbf{m^{(e)_2}} = \rho^s \iiint\limits_{V^e} \mathbf{N_b^T N_b} dV = \rho^s t^s \iint\limits_{S^e} \mathbf{N_b^T N_b} dS \tag{5.57}$$

$$\mathbf{c^{(e)_2}} = \mu^s \iiint\limits_{V^e} \mathbf{N_b^T N_b} dV = \mu^s t^s \iint\limits_{S^e} \mathbf{N_b^T N_b} dS \tag{5.58}$$

As before the RHS terms of (4.44) are neglected, and instead the force field is computed from (4.47).

All integrations are analytically evaluated before implemented into the code.

5.3.3 Assembling

When the FEM-formulations for both in-plane- and bending-deformations are settled, the two contributions are assembled into total element matrices.

The local stiffness matrix of (5.56) can be expressed as

$$\mathbf{k}^{(\mathbf{e})_1}_{\mathbf{6x6}} = \begin{bmatrix} k^{(e)_1}_{11_{2x2}} & k^{(e)_1}_{12_{2x2}} & k^{(e)_1}_{13_{2x2}} \\ k^{(e)_1}_{21_{2x2}} & k^{(e)_1}_{22_{2x2}} & k^{(e)_1}_{23_{2x2}} \\ k^{(e)_1}_{31_{2x2}} & k^{(e)_1}_{32_{2x2}} & k^{(e)_1}_{33_{2x2}} \end{bmatrix} \tag{5.59}$$

with corresponding deformations

$$\mathbf{u}^{\mathbf{s}}_{(\mathbf{e})_1} = \mathbf{q} = \begin{bmatrix} u^s_1 \\ v^s_1 \\ u^s_2 \\ v^s_2 \\ u^s_3 \\ v^s_3 \end{bmatrix} \tag{5.60}$$

Similarly for the bending part

$$\mathbf{k}^{(\mathbf{e})_2}_{\mathbf{9x9}} = \begin{bmatrix} k^{(e)_2}_{11_{3x3}} & k^{(e)_2}_{12_{3x3}} & k^{(e)_2}_{13_{3x3}} \\ k^{(e)_2}_{21_{3x3}} & k^{(e)_2}_{22_{3x3}} & k^{(e)_2}_{23_{3x3}} \\ k^{(e)_2}_{31_{3x3}} & k^{(e)_2}_{32_{3x3}} & k^{(e)_2}_{33_{3x3}} \end{bmatrix} \tag{5.61}$$

with corresponding deformations

$$\mathbf{u}^{\mathbf{s}}_{(\mathbf{e})_2} = \mathbf{q_b} = \begin{bmatrix} w^s_1 \\ \theta_{x_1} \\ -\theta_{y_1} \\ w^s_2 \\ \theta_{x_2} \\ -\theta_{y_2} \\ w^s_3 \\ \theta_{x_3} \\ -\theta_{y_3} \end{bmatrix} \tag{5.62}$$

The two contributions are then assembled into a total element matrix as

$$\mathbf{k}^{(\mathbf{e})_{\mathbf{tot}}}_{\mathbf{18x18}} = \begin{bmatrix} k^{(e)_1}_{11_{2x2}} & \mathbf{0}_{2x3} & \mathbf{0}_{2x1} & k^{(e)_1}_{12_{2x2}} & \mathbf{0}_{2x3} & \mathbf{0}_{2x1} & k^{(e)_1}_{13_{2x2}} & \mathbf{0}_{2x3} & \mathbf{0}_{2x1} \\ \mathbf{0}_{3x2} & k^{(e)_2}_{11_{3x3}} & \mathbf{0}_{3x1} & \mathbf{0}_{3x2} & k^{(e)_2}_{12_{3x3}} & \mathbf{0}_{3x1} & \mathbf{0}_{3x2} & k^{(e)_2}_{13_{3x3}} & \mathbf{0}_{3x1} \\ \mathbf{0}_{1x2} & \mathbf{0}_{1x3} & \mathbf{0}_{1x1} & \mathbf{0}_{1x2} & \mathbf{0}_{1x3} & \mathbf{0}_{1x1} & \mathbf{0}_{1x2} & \mathbf{0}_{1x3} & \mathbf{0}_{1x1} \\ k^{(e)_1}_{21_{2x2}} & \mathbf{0}_{2x3} & \mathbf{0}_{2x1} & k^{(e)_1}_{22_{2x2}} & \mathbf{0}_{2x3} & \mathbf{0}_{2x1} & k^{(e)_1}_{23_{2x2}} & \mathbf{0}_{2x3} & \mathbf{0}_{2x1} \\ \mathbf{0}_{3x2} & k^{(e)_2}_{21_{3x3}} & \mathbf{0}_{3x1} & \mathbf{0}_{3x2} & k^{(e)_2}_{22_{3x3}} & \mathbf{0}_{3x1} & \mathbf{0}_{3x2} & k^{(e)_2}_{23_{3x3}} & \mathbf{0}_{3x1} \\ \mathbf{0}_{1x2} & \mathbf{0}_{1x3} & \mathbf{0}_{1x1} & \mathbf{0}_{1x2} & \mathbf{0}_{1x3} & \mathbf{0}_{1x1} & \mathbf{0}_{1x2} & \mathbf{0}_{1x3} & \mathbf{0}_{1x1} \\ k^{(e)_1}_{31_{2x2}} & \mathbf{0}_{2x3} & \mathbf{0}_{2x1} & k^{(e)_1}_{32_{2x2}} & \mathbf{0}_{2x3} & \mathbf{0}_{2x1} & k^{(e)_1}_{33_{2x2}} & \mathbf{0}_{2x3} & \mathbf{0}_{2x1} \\ \mathbf{0}_{3x2} & k^{(e)_2}_{31_{3x3}} & \mathbf{0}_{3x1} & \mathbf{0}_{3x2} & k^{(e)_2}_{32_{3x3}} & \mathbf{0}_{3x1} & \mathbf{0}_{3x2} & k^{(e)_2}_{33_{3x3}} & \mathbf{0}_{3x1} \\ \mathbf{0}_{1x2} & \mathbf{0}_{1x3} & \mathbf{0}_{1x1} & \mathbf{0}_{1x2} & \mathbf{0}_{1x3} & \mathbf{0}_{1x1} & \mathbf{0}_{1x2} & \mathbf{0}_{1x3} & \mathbf{0}_{1x1} \end{bmatrix} \tag{5.63}$$

where, for example, $\mathbf{0}_{1x2}$ corresponds to a zero matrix of 1 row and 2 columns. Deformations corresponding to (5.63) are

$$\mathbf{u}^{\mathbf{s}}_{\mathbf{(e)_{total}}} = \begin{bmatrix} u^s_1 \\ v^s_1 \\ w^s_1 \\ \theta_{x_1} \\ -\theta_{y_1} \\ \theta_{z_1} \\ u^s_2 \\ v^s_2 \\ w^s_2 \\ \theta_{x_2} \\ -\theta_{y_2} \\ \theta_{z_2} \\ u^s_3 \\ v^s_3 \\ w^s_3 \\ \theta_{x_3} \\ -\theta_{y_3} \\ \theta_{z_3} \end{bmatrix} \tag{5.64}$$

The rows and columns of (5.63) that contain only zeros correspond to θ_z, which must be included since each plate is a part of a three dimensional shell. As the matrix is transformed into the global coordinate system this variable will not be zero.

Each node are given a global node-number which determines the position in the global matrix. Before the matrix-components of (5.63) are put into the global stiffness matrix $\mathbf{K}$ the local matrix is transformed into the global coordinates as

$$\mathbf{k}^{(\mathbf{e})} = \lambda^T_{tot} \mathbf{k}^{(\mathbf{e})_{\mathbf{tot}}}_{\mathbf{18x18}} \lambda_{tot} \tag{5.65}$$

where

$$\lambda_{tot} = \begin{bmatrix} \lambda_{6x6} & \mathbf{0}_{6x6} & \mathbf{0}_{6x6} \\ \mathbf{0}_{6x6} & \lambda_{6x6} & \mathbf{0}_{6x6} \\ \mathbf{0}_{6x6} & \mathbf{0}_{6x6} & \lambda_{6x6} \end{bmatrix} \tag{5.66}$$

$$\lambda_{6x6} = \begin{bmatrix} l_{xX} & m_{yX} & n_{zX} & 0 & 0 & 0 \\ l_{xY} & m_{yY} & n_{zY} & 0 & 0 & 0 \\ l_{xZ} & m_{yZ} & n_{zZ} & 0 & 0 & 0 \\ 0 & 0 & 0 & l_{xX} & m_{yX} & n_{zX} \\ 0 & 0 & 0 & l_{xY} & m_{yY} & n_{zY} \\ 0 & 0 & 0 & l_{xZ} & m_{yZ} & n_{zZ} \end{bmatrix} \tag{5.67}$$

The non-zero elements of the matrix λ_{6x6} are the direction-cosines between the local- (x, y, z) and the global-(X, Y, Z)-coordinate systems.

The above assembling procedure also applies to the mass- and damping-matrices.

When all local matrices have been assembled into global matrices the resulting system of equations, is a system of ordinary differential equations with respect to time as

$$\mathbf{M}\frac{\partial^2 \mathbf{u}}{\partial t^2} + \mathbf{C}\frac{\partial \mathbf{u}}{\partial t} + \mathbf{K}\mathbf{u} = \mathbf{F} \tag{5.68}$$

where $\mathbf{M}, \mathbf{C}, \mathbf{K}$ are the global mass-, damping-, and stiffness-matrices, respectively. $\mathbf{u}$ is the global deformation vector, and $\mathbf{F}$ is the global force vector computed from (4.47). Finally, before solving the system of equations the Dirichlet (or essential) boundary conditions are forced to the solution by specification directly in the system matrices.

5.3.4 System of equations solver

The system of ordinary equations (5.68) is re-written as a system of first order time derivatives, and then solved using a combined implicit Euler- and a Gauss-Seidel-scheme (5.18). The implicit (or backward) Euler scheme is given by

$$y_{n+1} = y_n + \Delta t f\left(t_{n+1}, y_{n+1}\right) \tag{5.69}$$

Chapter 6

Summary of Results

This work consists of results partially from computations on different systems of bifurcating pipes, and partially from the evaluation of an Fluid-Structure Interaction (FSI) code. The aim with the FSI-code is to model flow of blood in elastic arteries.

All studies performed have a physiological perspective, since such flows (except the cylinder case) are found in the arterial system of the human body. Such physiological flows are characterized by pulsation and three-dimensional effects such as flow separation, strong secondary motion in the cross-sectional plane, and large temporal- and spatial-variations in the Wall Shear-Stress (WSS). Additionally, the flows are intermittently in the transitional regime, which adds to the complexity.

6.1 Wall Shear Stress Patterns

As the disease of atherosclerosis often is found in the vicinity of bifurcations and in curvatures [8, 42, 121, 133, 173, 205], where the flow is rather unsteady, it has been hypothesized that the mechanical forces due to the flow are involved in the atherosclerotic process. These forces are mainly discussed in terms of the wall shear stress (WSS) [2, 14, 16, 66, 67, 118]. Therefore the dynamics of the WSS have been studied.

The results show large temporal and spatial derivatives of the WSS-components (τ_{xr}, $\tau_{\theta r}$) in the vicinity of the bifurcation. Figures 6.1(a) and 6.1(b) show peaks of the derivatives of τ_{xr} in the first part of the daughter vessel, after a 90-degree bifurcation (see Paper 2).

The outer wall of streamline curvature in the 90-degree bifurcation is often referred to as more "safe", since the flow is more uniform there [14, 15, 72]. However, these results show that due to the pulsating character of the flow, there are temporal variations there as well, including large derivatives of the WSS, as shown for the time derivative in Figure 6.2. It must be remembered that

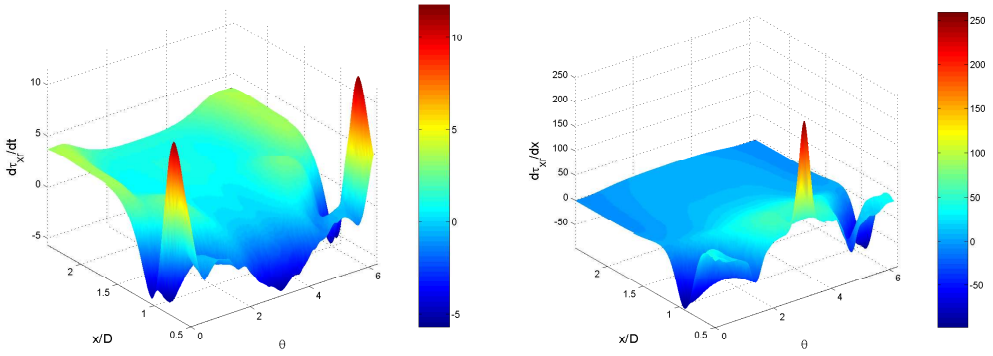

(a) $\frac{\partial \tau_{xr}}{\partial t}$ at $t/T = 0.228$. (b) $\frac{\partial \tau_{xr}}{\partial x}$ at $t/T = 0.228$.

Figure 6.1: Derivatives of axial WSS-component at peak velocity.

atherosclerotic plaques are found also at such locations, although less frequently [42]. Large temporal- and spatial-derivatives of the WSS were found at increased Reynolds- and Womersley-numbers as well.

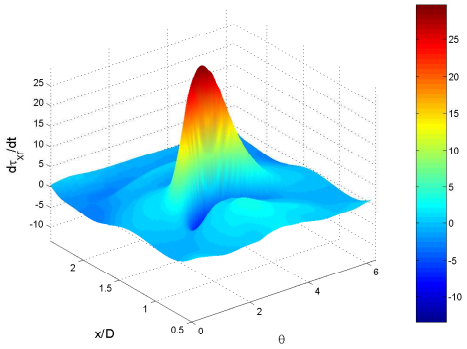

Figure 6.2: $\frac{\partial \tau_{xr}}{\partial t}$ at $t/T = 0.355$.

6.2 Secondary Flows

The characteristics of the WSS described above are due to the dynamics of the surrounding flow, which has also been investigated.

The flow through a 90-degree bifurcation shows similar characteristics as the flow through a 90-degree bent pipe, since the streamlines are curved similarly. These characteristics are secondary vortical flows, as well as possibly regions of separation. The typical vortical pattern in steady flows in bent pipes is a pair of Dean vortices, induced by the centrifugal effect. However, in the case of pulsatile or sinusoidal flows in curved pipes, other secondary patterns are found, such

as multiple vortex structures and secondary motion in the opposite direction as compared to the classical Dean vortices [30, 44, 119, 170, 176, 180]. Similarly, different patterns than the regular Dean vortices are expected in the case of pulsatile flow through a 90-degree bifurcation, which may also explain some of the WSS-patterns previously found.

The results show that the flow field goes through different stages as the driving pressure varies. An increased Reynolds number ($Re = 5800$) keeps the secondary structure as long as transition into turbulence can be avoided, while a higher Womersley number ($\alpha = 11.75$) changes the structure of the secondary flow. Figure 6.3 shows the evolution of the axial flow for the base case ($Re = 1450$ and $\alpha = 6.75$). The axial velocity is represented by contours, where the bold line is the zero contour. The interaction of separation with the secondary flow is found in Figure 6.3. In Figure 6.4 the secondary velocity vectors show multiple-vortex solutions for the base case ((a) and (b)), and for the high Re case (d). In (d) a similar double vortex pattern is found as in (a), although earlier in time, whereas the high α-case (c) only has a single vortex pattern, even though t/T is larger.

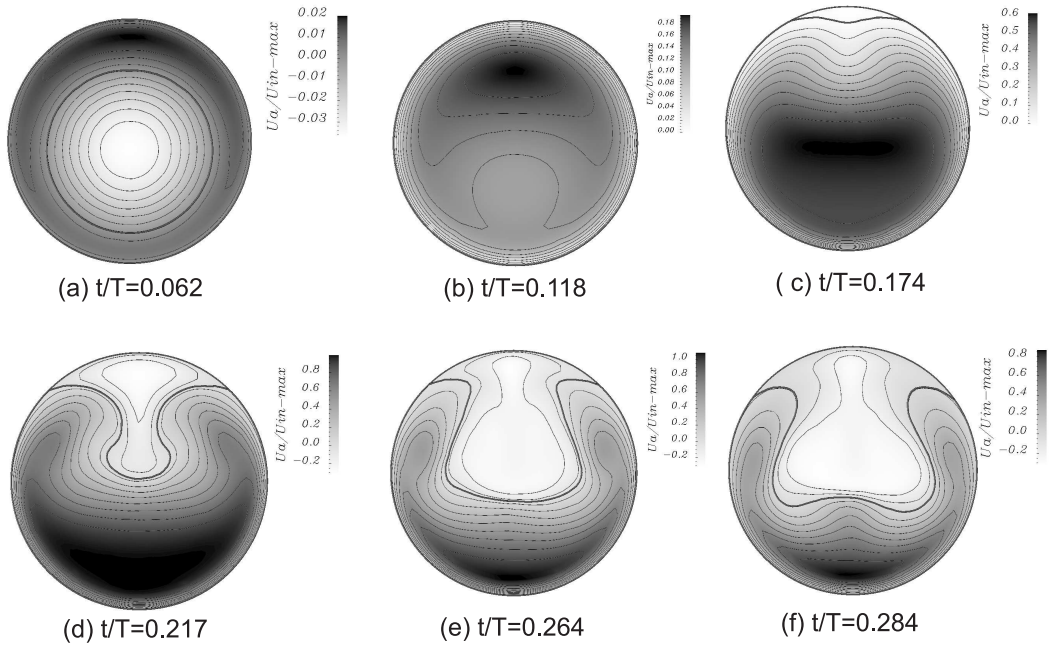

Figure 6.3: Axial contours of the axial velocity in a cross-plane after a 90-degree bifurcation; the bold line is the zero contour.

Further, the formation of multiple secondary vortices is found to cause changes to the separation pattern, and the secondary flow is found to influence the WSS variations.

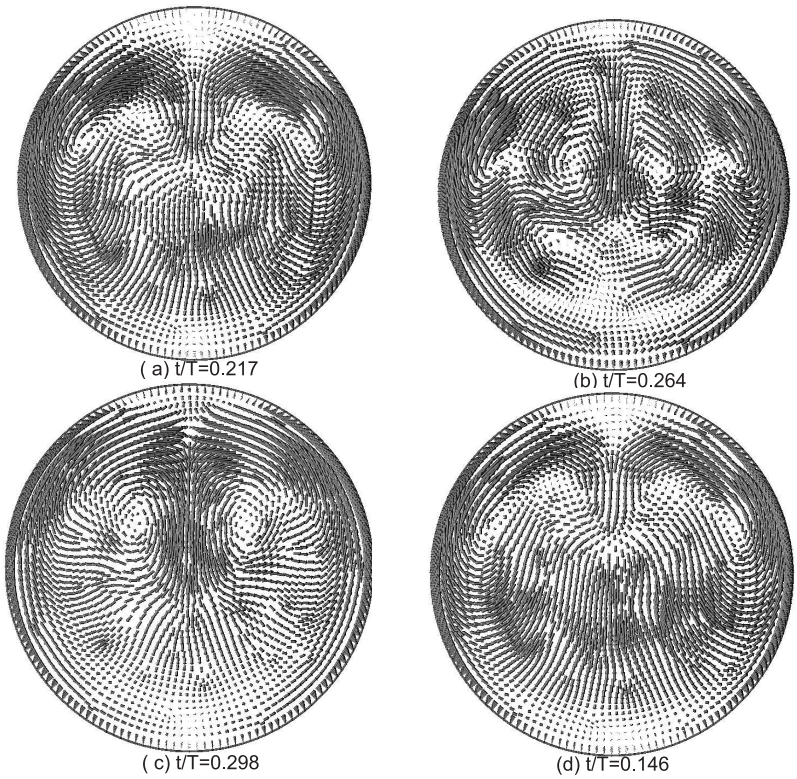

Figure 6.4: Secondary velocity vectors in a cross-plane after a 90-degree bifurcation.

6.3 Numerical Accuracy

The accuracy of a numerical solution depends on the errors that are associated with each of the steps in solving the problem: The accuracy of models used to describe the flow physics, the accuracy of the boundary conditions, the accuracy of the discretizations (grid, boundary, temporal and spatial discretization) and finally, the level of convergence of the iterative procedure. Since the accuracy of each step is not known a priori, most accuracy studies are done a posteriori. The accuracy of the models themselves can be estimated by experiments, given that the accuracy of the rest of the steps listed above is known.

In order to obtain a reliable solution it is important to verify that the discrete solution is a good approximation of the differential problem (so called discretization convergence). Comparing the solution on different grids allows one, if the grids are fine enough, to estimate the error both in approximating the differential problem (i.e. the truncation error), and the error in approximating the differential solution (convergence error). The issues regarding the numerical accuracy of the results are discussed in each paper.

Another important issue necessary for obtaining an accurate solution is that the iterative process of solving the system equations has converged to small

enough levels. Different convergence criteria have been tested in order to assess its effect on the solution.

After discretization and linearization the algebraic system of equations for a variable ϕ is described as

$$a_P \phi_p = \sum_{nb} a_{nb} \phi_{nb} + b \tag{6.1}$$

where a_P is the coefficient of the cell center, a_{nb} are the influence coefficients of the neighboring cells, and b is contributions from sources and boundary conditions. The residual for the momentum equations is defined as the sum over all computational cells P of the imbalance of (6.1). It is then scaled and given by (6.2).

$$R = \frac{\sum_P \left| \sum_{nb} a_{nb} \phi_{nb} + b - a_P \phi_P \right|}{\sum_P |a_P \phi_P|} \tag{6.2}$$

For the continuity equation the scaled residual is defined as

$$R = \frac{R_{iterationN}}{R_{iteration5}} \tag{6.3}$$

where

$$R_{iteration} = \sum_P |\text{Rate Of Mass Creation In Cell P}| \tag{6.4}$$

In (6.3) $R_{iterationN}$ is (6.4) at iteration N and $R_{iteration5}$ is the largest value of (6.4) in the first five iterations. In Figures 6.5 and 6.6 results for the residual convergence criteria of 10^{-3}, 10^{-4}, 10^{-5} and 10^{-6} are compared. The computations were performed on a tetrahedral mesh, at a constant inlet Reynolds number of 1000, in the bifurcation model. Results are presented along two lines at $x/D = 1.97$ into the 90-degree daughter branch. One line crosses the pipe in the vertical direction (Figure 6.5) and the other line is perpendicular to this at the height of the centre of the daughter pipe (Figure 6.6).

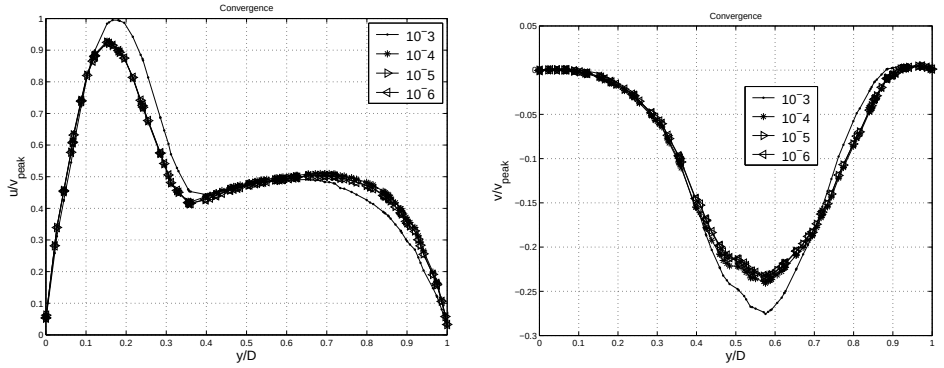

(a) u/v_{peak} (b) v/v_{peak}

Figure 6.5: Velocity profiles at different convergence criteria of a veritcal line in the daughter branch.

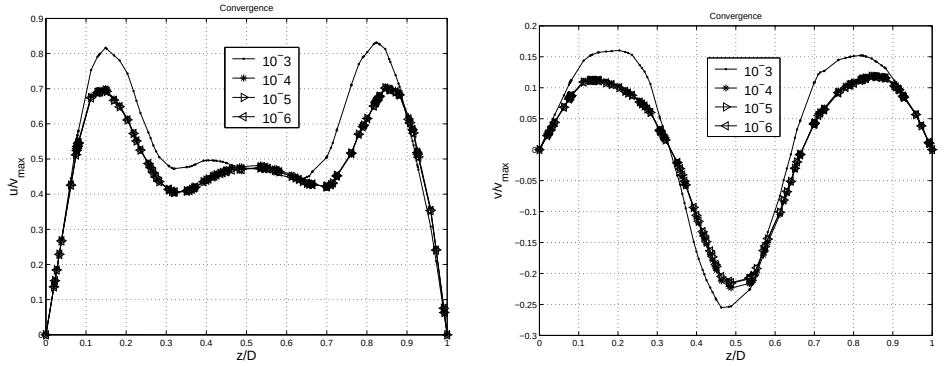

(a) u/v_{peak} (b) v/v_{peak}

Figure 6.6: Velocity profiles at different convergence criteria of a transverse line in the daughter branch.

The Figures 6.5 and 6.6 show that a convergence criteria, according to the residual definition in (6.2) and (6.3), of at least 10^{-4} is required for enough convergence. In the (FVM) calculations showing the results a convergence criteria of at least 10^{-4} has been used, and for each time step convergence up to eight digits or more, of each parameter, has been noted (using double precision).

6.4 Resolution at High Reynolds Number

In the high Reynolds number calculations ($Re = 5800$) typically some relatively fast oscillations are found. In order to determine that these fluctuations are actually resolved, it is necessary to compare them to which frequencies that are possible to resolve, with the chosen spatial and temporal resolution.

The temporal variation is investigated at certain locations of the domain. The points with most fluctuations are located in the separated region of the daughter branch after the 90-degree bifurcation. The three velocity components at one of these points (P1 in Paper 1) are shown in Figure 6.7, along with the frequency spectrum of the fluctuations of each component, respectively.

Before transforming the velocity time histories, using an FFT-algorithm, the large scale motion related directly to the velocity pulse is filtered out, leaving only the fluctuating component. The time resolution is $\Delta t = 0.0005$ s, which means that, according to the Nyqvist sampling theorem [179], frequencies up to $f = \frac{1}{2\Delta t}$ are resolved. That corresponds to a Strouhal number of $St_f = \frac{fD}{v_{inlet}} = 38.8$, given $D = 0.0085\,m$, being the local pipe diameter. However, the spatial resolution also limits what frequencies that can be resolved. A sinusoidal fluctuation requires three nodes in order to be resolved [58]. As seen in Figure 6.7 the frequencies are of order $St_f < 1$, and since $D/\Delta x \approx 17$, the fluctuations are considered well resolved.

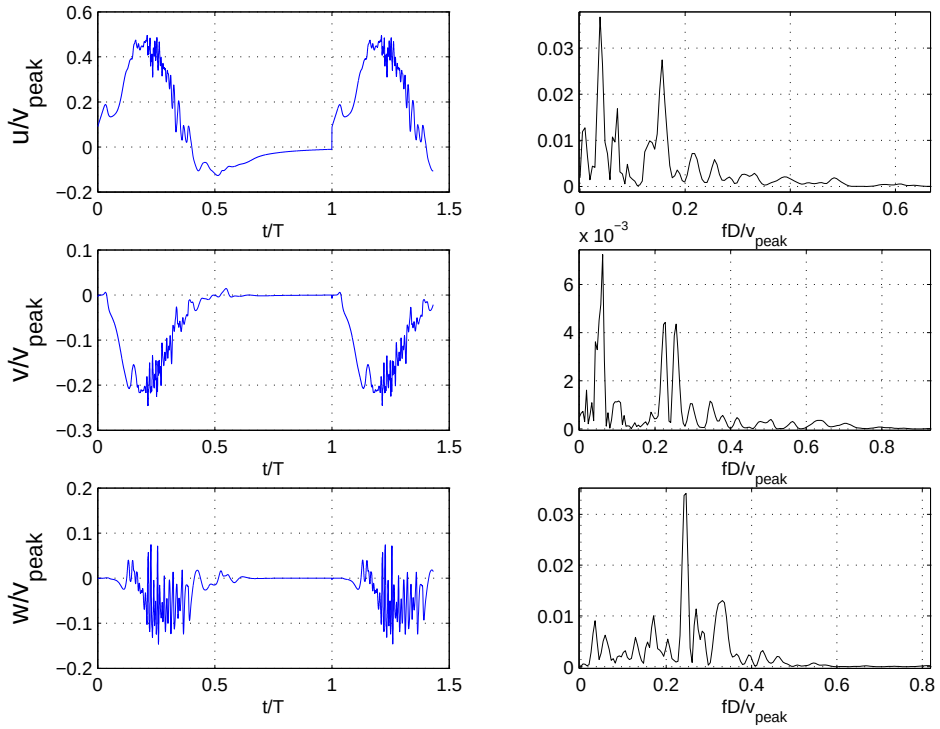

Figure 6.7: Velocity time history for all velocity components at $Re = 5800$ (left), and frequency spectra (right). The data is taken from a point in the separated region after the 90-degree bifurcation (P1 in Paper 1).

6.5 Propagation of Flow Patterns and Scalars

As the flow in systems of bifurcations often goes through several generations of branches, it is relevant to investigate the effects of upstream flow conditions on the downstream flow, i.e. how far down dynamical characteristics propagate through the system before they are diffused, or before the flow is dominated by other effects.

In order to determine that for pulsatile flow, computations have been performed in a three generation asymmetric model of bifurcations (see Paper 4). The first bifurcation is a 90-degree bifurcation followed by symmetric bifurcations with 30-degree bifurcation angles. Additionally, different inlet modules were attached to the inlet in order to mimic different upstream curvature effects, and to determine the sensitivity to those. Also, passive scalars in the range of $Sc = 0.72$–6280 were introduced at the inlet. The flow computations were performed at a peak $Re = 3000$ and $\alpha = 8.26$.

A skewed velocity distribution is found downstream of the 90-degree bifurcation as expected. The inlet-modules affect the early and the late phases in the cycle, whereas in the middle phase of the cycle, separation due to the curvature just before the inlet seems to stop upstream effects from propagating downstream. Two generations down the upstream asymmetric effects do not seem to influence the flow anymore. The velocity decreases for each generation as the total cross-sectional are increases, which gives more time for diffusion. Instead inertial effects caused by the latest curvature dominate the flow field.

The scalar transport is clearly affected by the geometrical asymmetry, as well as the different inlet-modules. Figure 6.8 shows the scalar differential distribution between the scalars of the largest- and the smallest-Schmidt numbers (Sc). Differences are found in the boundary layers, where the small Sc-scalar's concentration is larger. One can also see that the different inlet boundary conditions (Cases 1–4) causes different distributions throughout the cross-section. Cases 1–3 show a negative differential diffusion in the daughter vessel near the lower wall, while Case 4 and the steady case show positive differences there.

In the main branch Cases 1 and 2 show negative values to the left. Case 3 instead has positive concentration differences, whereas Case 4 has a positive concentration difference to the left, and a negative to the right of the main branch. The concentration difference for the steady case is more symmetric, and does not represent a pulsating flow very well. Thus, substances of different diffusivity will be distributed differently in the domain depending on the inflow conditions, and therefore substances of different Sc in blood flow will be affected similarly. The differences in concentrations between these Sc are up to approximately half the level of concentration of the large Sc scalar concentration. Thus, the effect of Sc is significant leading to non-uniform concentration of the substances in the blood in the arterial system.

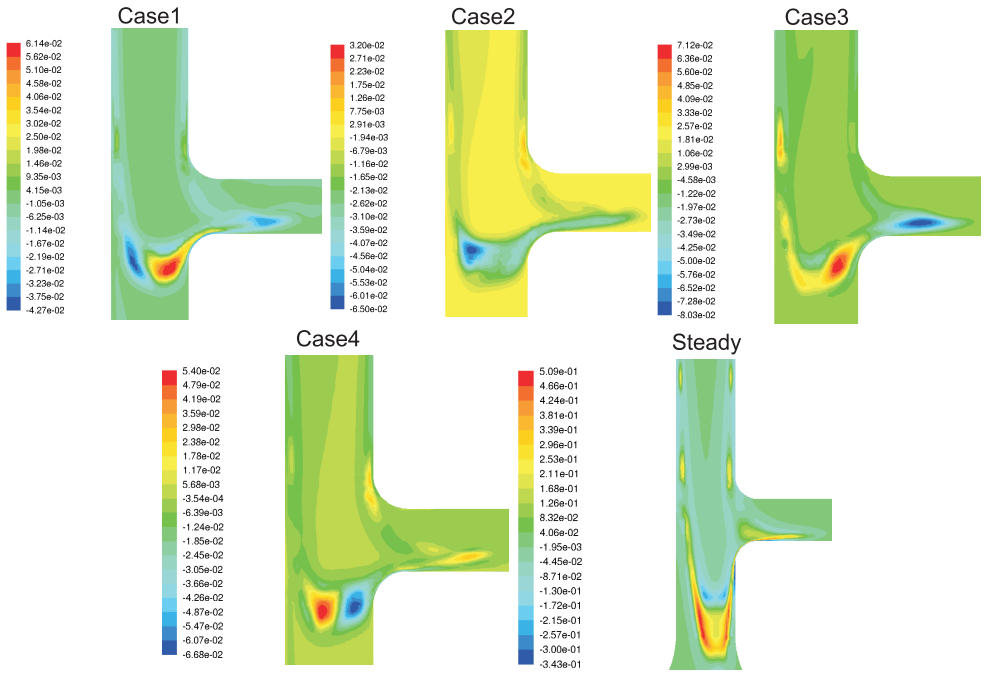

Figure 6.8: Difference between scalars of $Sc = 6280$ and $Sc = 0.72$ at $t/T = 0.24$.

In the lateral plane of the daughter branch (see Paper 4) the scalar distribution is very uneven over the cross-section, as shown in Figure 6.9. The separation near the inner curvature, and the centrifugal effects, distribute the scalar almost exclusively to the outer wall of curvature. That is despite the even distribution at the inlet. The different inlet conditions are shown to give the effect of skewness to the concentration distributions. Case 1 and the steady flow case show symmetric scalar distributions as expected. The steady case has a more flat and spread out high concentration field, as compared to Case 1. The other three cases show skewed concentration profiles. Cases 2 and 4 have scalars skewed towards the lower right wall, where the scalar of Case 4 is also more spread over the cross section. Case 3, on the other hand, has a scalar skewed towards the lower left wall.

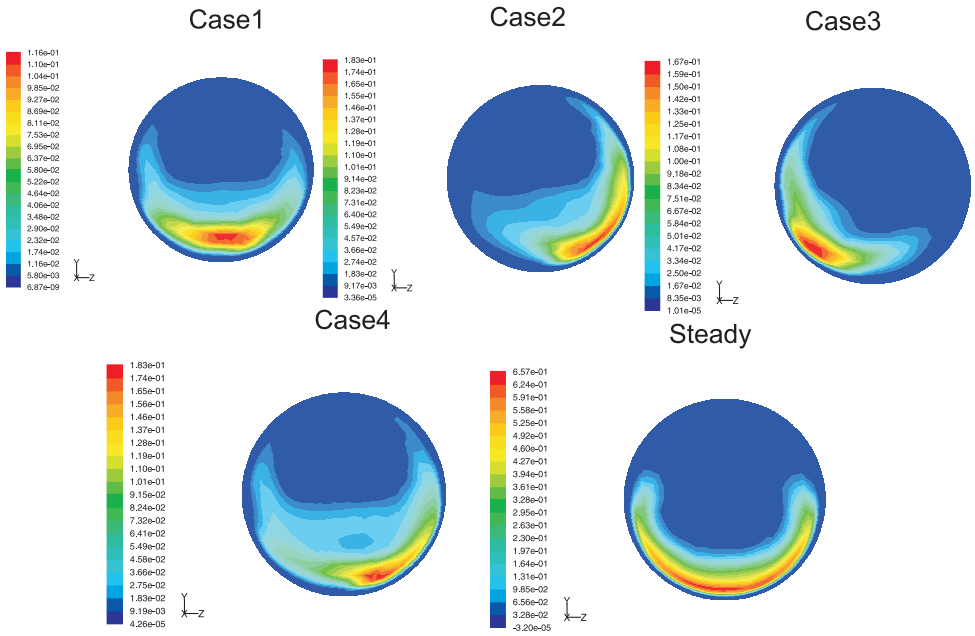

Figure 6.9: Scalar distribution in a lateral plane of the 90-degree daughter branch at $t/T = 0.24$ and $Sc = 6280$.

6.6 Fluid-Structure Interaction

As described above, a Finite Difference (FD) based Immersed-Boundary (IB) method is combined with a structural Finite Element Method (FEM) solver. The aim was to be able to model blood flow in elastic arteries, and investigate these effects on relevant parameters.

In order to validate the structural solver the results are compared to an analytical expression for the deformation of a thin cylindrical shell subject to axisymmetric radial loading.

A cylindrical shell subject to an axisymmetric load, as shown in Figure. 6.10, will through the approximations of thin-walled structures experience a radial deformation according to

$$w^s = \frac{Pe^{-\beta x}}{8\beta^3 D_b}\left(sin\beta x + cos\beta x\right) \tag{6.5}$$

$$\beta = \left(\frac{E^s t}{4R^2 D_b}\right)^{1/4} \tag{6.6}$$

$$D_b = \frac{E^s t^3}{12\left(1-\nu^{s2}\right)} \tag{6.7}$$

where P is the applied force continuously distributed around the cylinder, R is the cylinder radius, D_b is the flexural rigidity of the shell. The derivation of this

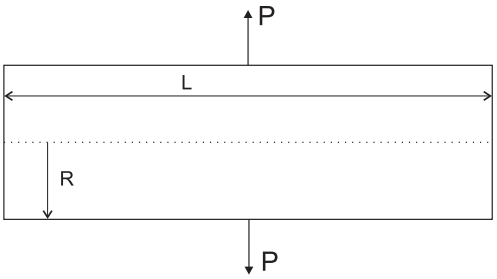

Figure 6.10: Cylinder with applied axisymmetric load.

analytical expression is described by Timoschenko et al. [188] and Vinson [196], amongst others. The formula is symmetrically applied around the circle of the applied load.

Figure 6.11(a) shows the displaced geometry for the finest grid, and Figure 6.11(b) shows the deformations along a line for several different grids, as well as the analytical expression. The element sizes are specified by the legends in the figure. It is clear that the solution converges towards the analytical expression, for an increased number of cells, although the numerical solution has some difficulties in capturing the negative displacements just beside the peak. The cylinder has a length over diameter ratio $L/D = 3.3$, and a thickness $t^s/D = 0.01$. The Poisson ratio is $\nu^s = 0.3$ and Young's modulus $E^s = 5 \cdot 10^9 \ N/m^2$.

In Figure 6.12 the error is plotted against the grid size. As the error is proportional to the leading term of the truncation error, i.e. the element size to the power of the order of the method in use, one would expect a convergence rate of 2. That is because linear (and higher order) polynomials have been used for approximation. However, that is only true if one has reached the asymptotic regime (small enough Δx), so that the higher order terms of the truncation are negligibly small [58]. The slope in the logarithmic plot is ≈ 0.9, which points to first order accuracy in practise.

In the solution procedure the structural deformation is computed for each fluid time-step $\Delta t = 0.01$. However, the time-step of the solid solver is $\Delta t = 0.0001$, and therefore for each fluid time step 100 time steps are computed for the structural solver. The reason is that a first order method in time (implicit Euler method) is used.

For each time step the solid system of equations solution algorithm is broken at $\|q^n - q^{n-1}\|_{max} < 5 \cdot 10^{-4}$, where q^{n-1} is the solution of the previous iteration and q^n is the present iteration.

These settings were found to give reasonable results for external flow around a cylinder (not included in the thesis), however, the studies with respect to the importance of arterial wall elasticity on the flow, are not yet completed.

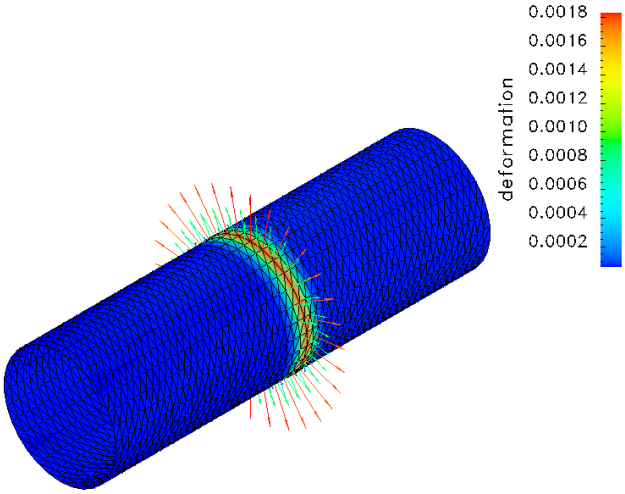

(a) Deformation of cylinder due to radially applied load.

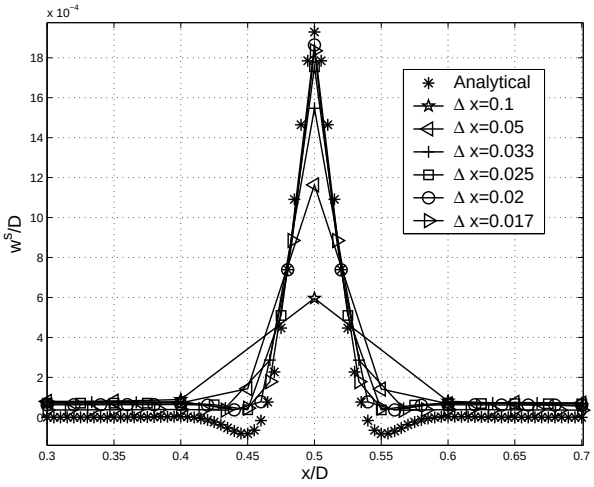

(b) Deformation of a generate line for different grid resolutions.

Figure 6.11: Deformation due to axially symmetric radial load of cylindrical shell.

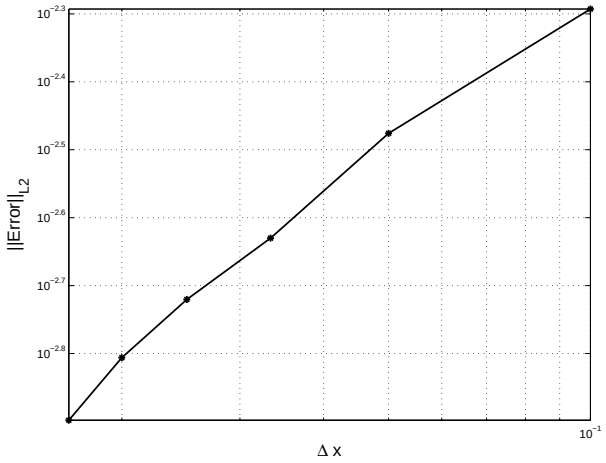

Figure 6.12: L2-norm of error versus element size along a generate line.

Chapter 7

Future Work

The studies presented in this thesis have shown that derivatives of the WSS are significant, also at locations referred to as more "safe". The WSS is affected by the secondary flow that shows character changes both with the Reynolds- and the Womersley-numbers. Also, the effect of bifurcations and curvature is shown to be very significant for the distribution of scalars, affecting them differently depending on the Schmidt number. For improved modeling of physiological flows, and understanding of hemodynamically relevant characteristics, suggestions are:

- The effects of variations in Re and α on the secondary flow have been studied. That study may be extended by investigating the effect of variations in curvature ratio and bifurcation angle on the characteristics of secondary flow (vortical structures), and on WSS variations. These cases are not much investigated for pulsating flow in bifurcations in literature.

- Atheroslcerosis has been related to mass transport of different blood components over the cross-section. As the disease appears at locations, such as near bifurcations and in large curvature, the effect of the flow on the distribution of different components may be significant. As shown above the effect of the flow on passive scalars of different diffusivity is significant. As it is found that different Re and α affects the character of the flow (different secondary vortical structures), these parameters most probably affect the distribution of the scalars. Such comparison would be interesting since the disease is found at various parameter values of Re and α.

- The blood is often considered as being Newtonian, also here, despite its non-Newtonian character. Most often these effects are found to be rather small, however, in some cases they are reported to be of significance. There are various constitutive models that can be implemented, such as Bingham, Casson, Quemada. Another approach would be to simulate the blood cells in the plasma using multiphase models. This would show actual significance of non-Newtonian effects in the flows considered here.

- The effects of extensible walls on flow parameters, such as wall shear stress, are often considered to be small. However, modeling them, using an FSI-model would reveal how small they are here. The wall extension may also influence the secondary flow patterns, and therefore also the distribution of different blood components.

Chapter 8

Summary of Papers

Paper I

Philip Evegren & Laszlo Fuchs, "Pulsatile Flow in Branching Arteries", Presented at the 3:rd IC-SCCE conference, Athens, 2008.

The role of fluid mechanics in relation to the patho-physiological process of atherosclerosis has been investigated over many years. One has observed that morphological manifestations of the disease are found at some well defined locations: certain vessel bifurcations and curvature. The flow in these regions is characterized by separation and unsteadiness. There are several hypotheses relating the flow to atheroslcerosis, which include flow separation, the level of wall shear stress and its spatial and temporal variations. Currently there are no theories that can explain the process since the different components in the process are not fully known nor understood. The problems are related to the complexity of the biological systems involved, and even the fluid mechanical aspects (related to the mechanical effects on the vessel wall and the transport of biological active substances) are not well documented or understood. This paper is aimed at shedding some light on the transitional flow near a bifurcation and on the effects of some relevant parameters (Reynolds number and Womersley number). The results indicate the presence of local regions of strong temporal- and spatial-variations of wall shear stress, even at locations often referred to as "safe". Increased Reynolds number yields transitional behavior close to a separated region, while other parts of the domain show no such behavior. On the other hand an increased Womersley number delays flow separation.

The candidate computed the results and was the main author of the paper.

Paper II

Philip Evegren, Laszlo Fuchs & Johan Revstedt, "Wall Shear Stress Variations in a 90-degree Bifurcation in 3D Pulsating Flows", on revision for publication in Medical Engineering & Physics

The exact role of fluid mechanics in the patho-physiological process of atherosclerosis has been a research topic over many years, yet without clear conclusive result. One has observed that morphological manifestations of the disease are found at some well defined locations: certain vessel bifurcations and in curvatures. The flow in these regions is characterized by unsteadiness and often separation. Currently there are no complete theories that can explain the process since the different components in the process are not fully understood. Here we carry out detailed computations of the unsteady flow in an arterial segment typical to location of early appearance of arterial lesions. We study the wall shear stress (WSS) field variations near a junction with the purpose of identifying fluid-mechanical parameters that can be related to sites of atheroslcerosis. The results show that regions associated with atherosclerosis experience highly elevated temporal- and spatial-derivatives of the WSS, also at less commonly known locations. Thus, large derivatives in time and space do not seem unique for the most common areas of atherosclerosis. Differences in WSS character between these locations are identified as differences in the time period of back flow as well as differences in the magnitude of the WSS derivatives. The data is presented in a way that facilitates understanding of the variations in WSS.

The candidate computed the results and was the main author of the paper.

Paper III

Philip Evegren, Laszlo Fuchs & Johan Revstedt, "On the Secondary Flow Through Bifurcating Pipes", submitted to Physics of Fluids.

The flow through curved and bifurcating pipes induces secondary motion which has been subject to investigation over long time due to the general interest in such flows. In contrast to the flow in a straight pipe curvature leads to the formation of secondary flow which is often unsteady. Streamline curvature occurs also in bifurcating pipes leading to some corresponding secondary, unsteady flow. This paper presents a detailed description on the unsteady flow in the daughter branch after a 90-degree bifurcation at a range of Reynolds- and Womerlsey-numbers. The results show the presence of Dean vortices and additionally new vortical patterns not reported in the literature. Both the streamwise (axial) and the secondary flow components change character at larger Womersley numbers, leading to less complex secondary flow. Also, at larger Reynolds numbers, flow instabilities are observed. The secondary flow may lead to the formation of unsteady separation bubbles. This in turn yields peaks in the wall shear stress components. Such wall shear stress variations have often been related in the literature to the processes that may lead to atherosclerosis.

The candidate computed the results and was the main author of the paper.

Paper IV

Philip Evegren, Johan Revstedt & Laszlo Fuchs, "Pulsating Flow & Mass Transfer in an Asymmetric System of Bifurcations", submitted to Computers and Fluids.

Pulsating flow through bifurcations are of general interest. In the human body such flows are also very common; for example in blood vessels and the respiratory tract. The characteristics of the flow in arteries have been related to the process of atherogenesis, based on the observation that the initial manifestation of the process is observed at certain common locations, i.e. near bifurcations in vessels of certain size. In-spite of these observations there is no direct understanding between the flow itself and the pathological process. In fact, the flow itself is rather complex since it is unsteady and transitional. The flow causes temporal and spatial variations in the Wall Shear Stress (WSS) which is believed to be an important contributing factor for atherosclerosis. The paper considers both unsteady- and steady-flow through a three generation system of (non-symmetric) bifurcations. The geometry consists of a 90-degree bifurcation followed by two sets of consecutive symmetric bifurcations. The aim of the paper is to investigate the effects of the bifurcations on the flow and mass transport in such a geometrical configuration that is often found in physiological situations. Additionally, the effects of different inlet velocity conditions have been considered. The different inlet conditions are aimed at studying the sensitivity to variations of inflow conditions; variations found under normal physiological conditions. The results show that the geometrical asymmetry affects the velocity distribution even after a second bifurcation downstream. Two generations down this asymmetry does not have a significant effect anymore. The different inlet conditions affect the flow to the next generation of branches during different pahses of the flow cycle. At peak flow and further downstream in the system the effects are negligible. It is also found that over a cycle the mass flow distribution through the different branches, given the same outlet pressure level, can be affected by the inlet velocity conditions. The distribution of a passive scalar is not uniform but depends on the inlet conditions and strongly on the Schmidt number (i.e. molecular diffusion). Schmidt number effect can account for as much as 50% deviation in the concentration of scalars with different molecular diffusivities.

The candidate computed the results and was the main author of the paper.

Bibliography

[1] Jr. A.M. Gotto. Lipid lowering, regression, and coronary events: A review of the interdisciplinary council on lipids and cardiovascular risk intervention, seventh council meeting. *Circulation*, 92:646–656, 1995.

[2] T. Asakura and T. Karino. Flow patterns and spatial distribution of atherosclerotic lesions in human coronary arteries. *Circulation Research*, 66:1045–1066, 1990.

[3] F.P.T. Baaijens. A fictitious domain/mortar element method for fluid-structure interaction. *International Journal for Numerical Methods in Fluids*, 35:743–761, 2001.

[4] X.S. Bai, L. Fuchs, and J. Gullbrand. On modeling aspects of swirling stabilized diffusion flames. *35th Aerospace Sciences Meeting & Exhibit, Reno*, AIAA 97-0371, 1997.

[5] I. Balásházy, T. Heistracher, and W. Hofmann. Air flow and particle deposition patterns in bronchial airway bifurcations: The effect of different cfd models and bifurcation geometries. *Journal of Aerosol Medicine*, 9(3):287–301, 1996.

[6] K.A. Barbee, P.F. Davies, and R. Lal. Shear stress-induced reorganization of the surface topography of living endothelial cells imaged by atomic force microscopy. *Circulation Research*, 74:163–171, 1994.

[7] S.N. Barua. On secondary flow in stationary curved pipes. *Quarterly Journal of Mechanics and Applied Mathematics*, 16(1):61–77, 1963.

[8] H.S. Bassiouny, C.K. Zarins, M.H. Kadowaki, and S. Glagov. Hemodynamic stress and experimental aortoiliac atherosclerosis. *Journal of Vascular Surgery*, 19:426–434, 1994.

[9] G.K. Batchelor. *An Introduction to Fluid Dynamics*. Cambridge University Press, 2000.

[10] S.A. Berger and L-D. Jou. Flows in stenotic vessels. *Annual Review of Fluid Mechanics*, 32:347–382, 2000.

[11] B. Berthier, R. Bouzerar, and C. Legallais. Blood flow patterns in an anatomically realistic coronary vessel: Influence of three different reconstruction methods. *Journal of Biomechanics*, 35:1347–1356, 2002.

[12] F. Bertrand, P.A. Tanguy, and F. Thibault. A three-dimensional fictitious domain method for incompressible fluid flow problems. *International Journal for Numerical Methods in Fluids*, 25:719–736, 1997.

[13] B.W.A.M.M. Beulen, M.C.M. Rutten, and F.N. van de Vosse. A time-periodic approach for fluid-structure interaction in distensible vessels. *Journal of Fluids and Structures*, 25:954–966, 2009.

[14] B.K. Bharadvaj, R.F. Mabon, and D.P. Giddens. Steady flow in a model of the human carotid bifurcation. part i–flow visualization. *Journal of Biomechanics*, 15(5):349–362, 1982.

[15] B.K. Bharadvaj, R.F. Mabon, and D.P. Giddens. Steady flow in a model of the human carotid bifurcation. part ii–laser-doppler anemometer measurements. *Journal of Biomechanics*, 15(5):363–378, 1982.

[16] D. Birchall, A. Zaman, J. Hacker, G. Davies, and D. Mendelow. Analysis of haemodynamic disturbance in the atherosclerotic carotid artery using computational fluid dynamics. *European Radiology*, 16:1074–1083, 2006.

[17] O. Boiron, V. Deplano, and R. Pelissier. Experimental and numerical studies on the starting effect on the secondary flow in a bend. *Journal of Fluid Mechanics*, 574:109–129, 2007.

[18] G. Bonfigli. Influence of the discretized order on the accuracy of an immersed-boundary procedure for incompressible flows. *AIAA Computational Fluid Dynamics*, 19, June 2008.

[19] A. Borg. *Experimental and Numerical Studies of Flows Related to the Processes of Atherosclerosis*. Doctoral Thesis, Lund Univeristy, Sweden, 2000.

[20] D.W.A. Brands, G.W.M. Peters, and P.H.M. Bovendeerd. Design and numerical implementation of a 3-d non-linear viscoelastic constitutive model for brain tissue during impact. *Journal of Biomechanics*, 37:127–134, 2004.

[21] A.L. Braun and A.M. Awruch. Finite element simulation of the wind action over bridge sectional models: Application to the guamá river bridge (pará state, brazil). *Finite Element in Analysis and Design*, 44:105–122, 2008.

[22] A.L. Braun and A.M. Awruch. Aerodynamic and aeroelastic analyses on the caarc standard tall building model using numerical simulation. *Computers and Structures*, 87:564–581, 2009.

[23] J.D. Bronzino, editor. *The Biomedical Engineering Handbook*. Boca Raton: CRC Press: Heidelberg: Springer, 2000.

[24] J.D. Bronzino, editor. *The Biomedical Engineering Handbook*. Boca Raton: CRC/Taylor & Francis, third edition, 2006.

[25] D.E. Brooks, J.W. Goodwin, and G.V.F. Seaman. Interactions among erythrocytes under shear. *Journal of Applied Physiology*, 28(2):172–177, 1970.

[26] V.M. Calo, N.F. Brasher, Y. Bazilevs, and T.J.R. Hughes. Multiphysics model for blood flow and drug transport with application to patient-specific coronary artery flow. *Computational Mechanics*, 43:161–177, 2008.

[27] C.G. Caro, J.M. Fitz-Gerald, and R.C. Schroter. Arterial wall shear and distribution of early atheroma in man. *Nature*, 223:1159–1161, 1969.

[28] C.G. Caro, J.M. Fitz-Gerald, and R.C. Schroter. Atheroma and arterial wall shear observation, correlation and proposal of a shear dependent mass transfer mechanism for atherogenesis. *Proceedings of the Royal Society of London. Series B, Biological Sciences*, 177(1046):109–133, 1971.

[29] M.Ö. Çarpinlioğlu and M.Y. Gündoğdu. A critical review on pulsatile pipe flow studies directing towards future research topics. *Flow Measurement and Instrumentation*, 12:163–174, 2001.

[30] L.-J. Chang and J.M. Tarbell. Numerical simulation of fully developed sinusoidal and pulsatile (physiological) flow in curved tubes. *Journal of Fluid Mechanics*, 161:175–198, 1985.

[31] M. Charakida, J.E. Deanfield, and J.P.J. Halcox. The role of nitric oxide in early atherosclerosis. *European Journal of Clinical Pharmacology*, 62:69–78, 2006.

[32] A.Y. Cheer and C.P. van Dam, editors. *Fluid Dynamics in Biology*. American Mathematical Society, 1993.

[33] J. Chen and X. Lu. Numerical investigation of the non-newtonian blood flow in a bifurcation model with a non-planar branch. *Journal of Biomechanics*, 37:1899–1911, 2004.

[34] J. Chen and X. Lu. Numerical investigation of the non-newtonian blood flow ina a bifurcation model with a non-planar branch. *Journal of Biomechanics*, 39:818–832, 2006.

[35] M. Cinthio, Å. Rydèn-Ahlgren, J. Bergkvist, T. Jansson, H.W. Persson, and K. Lindström. Longitudinal movements and resulting shear strain of the arterial wall. *American Journal of Physiology Cell Physiology*, 291(1):394–402, 2006.

[36] C. Clark and D.L. Schultz. Velocity distribution in aortic flow. *Cardiovascular Research*, 7:601–613, 1973.

[37] J.K. Comer, C. Kleinstreuer, and C.S. Kim. Flow structures and particle deposition patterns in double-bifurcation airway models. part 2. aerosol transport and deposition. *Journal of Fluid Mechanics*, 435:55–80, 2001.

[38] J.K. Comer, C. Kleinstreuer, and Z. Zhang. Flow structures and particle deposition patterns in double-bifurcation airway models. part 1. air flow fields. *Journal of Fluid Mechanics*, 435:25–54, 2001.

[39] P. Constantinides. Cause of thrombosis in human atherosclerotic arteries. *American Journal of Cardiology*, 66:37G–40G, 1990.

[40] W.R. Dean. Note on the motion of fluid in a curved pipe. *Philosophical Magazine and Journal of Science*, 4(20):208–223, 1927.

[41] W.R. Dean. The stream-line motion of fluid in a curved pipe. *Philosophical Magazine and Journal of Science*, 5(30):673–695, 1928.

[42] M.E. DeBakey, G.M. Lawrie, and D.H. Glaeser. Patterns of atheroslcerosis and their surgical significans. *Annals of Surgery*, 201(2):115–131, 1985.

[43] J. Degroote, K. Bathe, and J. Vierendeels. Performance of a new partitioned procedure versus a monolithic procedure in fluid-structure interaction. *Computers and Structures*, 87:793–801, 2009.

[44] S.C.R. Dennis and Michael NG. Dual solutions for steady laminar flow through a curved tube. *Quarterly Journal of Mechanics and Applied Mathematics*, 35(3):305–324, 1982.

[45] N. DePaola, Jr M.A. Gimbrone, P.F. Davies, and Jr C.F. Dewey. Vascular endothelium responds to fluid shear stress gradients. *Arteriosclerosis, Thrombosis, and Vascular Biology*, 12:1254–1257, 1992.

[46] J. Donea, S. Giuliani, and J.P. Halleux. An arbitrary lagrangian-eulerian finite element method for transient dynamic fluid-structure interactions. *Computer Methods in Applied Mechanics and Engineering*, 33:689–723, 1982.

[47] F. Durst, S. Ray, B. Ünsal, and O.A. Bayoumi. The development lengths of laminar pipe and channel flows. *Journal of Fluids Engineering*, 127:1154–1160, 2005.

[48] D.M. Eckmann and J.B. Grotberg. Experiments on transition to turbulence in oscillatory pipe flow. *Journal of Fluid Mechanics*, 222:329–350, 1991.

[49] C.P. Ellington and T.J. Pedley, editors. *Biological Fluid Dynamics.* The Company of Biologists Limited, 1995.

[50] P. Evegren, L. Fuchs, and J. Revstedt. On the secondary flow through bifurcating pipes. *submitted to Physics of Fluids*, .:., 2009.

[51] P. Evegren, L. Fuchs, and J. Revstedt. Wall shear stress variations in a 90-degree bifurcation in 3d pulsating flows. *submitted to Medical Engineering & Physics*, .:., 2009.

[52] P. Evegren, J. Revstedt, and L. Fuchs. Pulsating flow & mass transfer in an asymmetric system of bifurcations. *submitted to Computers and Fluids*, .:., 2009.

[53] E.A. Fadlun, R. Verzicco, P. Orlandi, and J. Mohd-Yusof. Combined immersed-boundary finite-difference methods for three-dimensional complex flow simulations. *Journal of Computational Physics*, 161:35–60, 2000.

[54] E. Falk, P.K. Shah, and V. Fuster. Coronary plaque disruption. *Circulation*, 92:657–671, 1995.

[55] J. Fan and T. Watanabe. Inflammatory reactions in the pathogenesis of atherosclerosis. *Journal of Atherosclerosis and Thrombosis*, 10(2):63–71, 2003.

[56] R. Fåhraeus and T. Lindqvist. The viscosity of the blood in narrow capillary tubes. *American Journal of Physiology*, 96:562–568, 1931.

[57] J.M. Fitz-Gerald. Atheroma and arterial wall shear observation, correlation and proposal of a shear dependent mass transfer mechanism for atherogenesis: Appendix. *Proceedings of the Royal Society of London. Series B, Biological Sciences*, 177(1046):133–159, 1971.

[58] C.A.J. Fletcher. *Computational Techniques for Fluid Dynamics, volumes 1 & 2.* Springer-Verlag, Berlin, Heidelberg, New York, second edition, 1991.

[59] Fluent Inc. *Fluent 6.2.16 Users Guide.*

[60] J.A. Fox and A.E. Hugh. Localization of atheroma: A theory based on boundary layer separation. *Brittish Heart Journal*, 28:388–399, 1966.

[61] F.E. Fresconi and A.K. Prasad. Secondary velocity fields in the conducting airways of the human lung. *Journal of Biomechanical Engineering*, 129:722–732, 2007.

[62] M.H. Friedman, O.J. Deters, C.B. Bargeron, G.M. Hutchins, and F.F. Mark. Shear-dependent thickening of the human arterial intima. *Atherosclerosis*, 60:161–171, 1986.

[63] M.H. Friedman, O.J. Deters, F.F. Mark, C.B. Bargeron, and G.M. Hutchins. Arterial geometry affects hemodynamics. *Atherosclerosis*, 46:225–231, 1983.

[64] M.H. Friedman and L.W. Ehrlich. Numerical simulation of aortic bifurcation flows: The effect of flow divider curvature. *Journal of Biomechanics*, 17(12):881–888, 1984.

[65] M.H. Friedman, G.M. Hutchins, C.B. Bargeron, O.J. Deters, and F.F. Mark. Correlation between intimal thickness and fluid shear in human arteries. *Atherosclerosis*, 39:425–436, 1981.

[66] M.H. Friedman, V. O'Brien, and L.W. Ehrlich. Calculations of pulsatile flow through a branch: Implications for the hemodynamics of atherogenesis. *Circulation Research*, 36:277–285, 1975.

[67] D.L. Fry. Acute vascular endothelial changes associated with increased blood velocity gradients. *Circulation Research*, 22:165–197, 1968.

[68] L. Fuchs and H-S. Zhao. Solution of three-dimensional viscous incompressible flows by a multi-grid method. *International Journal of Numerical Methods in Fluids*, 4:539–555, 1984.

[69] T. Fukui, K.H. Parker, Y. Imai, K. Tsubota, T. Ishikawa, S. Wada, and T. Yamaguchi. Effect of wall motion on arterial wall shear stress. *Journal of Biomechanical Science and Engineering*, 2(2):58–68, 2007.

[70] Y.C. Fung. *Biomechanics: Mechanical Properties of Living Tissues.* Springer–Verlag New York, Inc., second edition, 1993.

[71] Y.C. Fung. *Biomechanics: Circulation.* Springer–Verlag New York, Inc., second edition, 1997.

[72] V. Gambillara, G. Montorzi, C. Haziza-Pigeon, N. Stergiopulos, and P. Silacci. Arterial wall response to ex vivo exposure to oscillatory shear stress. *Journal of Vascular Research*, 42:535–544, 2005.

[73] S.D. Gertz and W.C. Roberts. Hemodynamic shear force in rupture of coronary arterial atherosclerotic plaques. *The American Journal of Cardiology*, 66:1368–1372, 1990.

[74] C.M. Gibson, L. Diaz, K. Kandarpa, F.M. Sacks, R.C. Pasternak, T. Sandor, C. Feldman, and P.H. Stone. Relation of vessel wall shear stress to atherosclerosis progression in human coronary arteries. *Arteriosclerosis and Thrombosis*, 13:310–315, 1993.

[75] R. Glowinski, T. Pan, and J. Periaux. A fictitious domain method for dirichlet problem and applications. *Computer Methods in Applied Mechanics and Engineering*, 111:283–303, 1994.

[76] R. Glowinski, T. Pan, and J. Periaux. A fictitious domain method for external incompressible viscous flow modeled by navier-stokes equations. *Computer Methods in Applied Mechanics and Engineering*, 112:133–148, 1994.

[77] D. Goldstein, R. Handler, and L. Sirovich. Modeling a no-slip flow boundary with an external force field. *Journal of Computational Physics*, 105:354–366, 1993.

[78] J. Gullbrand, X.S. Bai, and L. Fuchs. High-order cartesian grid method for calculation of incompressible turbulent flows. *International Journal for Numerical Methods in Fluids*, 36:687–709, 2001.

[79] G.H.L. Hagen. Uber die bewegung des wassers in engen cylindrischen röhren. *Poggendorf's Annalen der Physik und Chemie*, 46:423–442, 1839.

[80] P. Hall and K. Parker. The stability of the decaying flow in a suddenly blocked channel. *Journal of Fluid Mechanics*, 75:305–314, 1976.

[81] C.C. Hamakiotes and S.A. Berger. Periodic flows through curved tubes: the effect of the frequency parameter. *Journal of Fluid Mechanics*, 210:353–370, 1990.

[82] W. Harvey. *On the Motion of the Heart and Blood in Animals (translated by R. Willis in 1993)*. Prometheus Books, 1628.

[83] M.T. Heath. *Scientific Computing: An Introductory Survey*. McGraw-Hill, second edition, 2002.

[84] M. Heil, A.L. Hazel, and J. Boyle. Solver for large-displacement fluid-structure interaction problems: Segregated versus monolithic approaches. *Computational Mechanics*, 43:91–101, 2008.

[85] M. Hino, M. Sawamoto, and S. Takasu. Experiments on transition to turbulence in an oscillatory pipe flow. *Journal of Fluid Mechanics*, 75:193–207, 1976.

[86] C.W. Hirt, A.A. Amsden, and J.L. Cook. An arbitrary lagrangian-eulerian computing method for all flow speeds. *Journal of Computational Physics*, 14:227–253, 1974.

[87] J.H. Horlock. Some experiments on the secondary flow in pipe bends. *Proceedings of the Royal Society of London. Series A.*, 234(1198):335–346, 1956.

[88] B. Hübner, E. Walhorn, and D. Dinkler. A monolithic approach to fluid-structure interaction using space-time finite elements. *Computer Methods in Applied Mechanics and Engineering*, 193:2087–2104, 2004.

[89] J.D. Humphrey. Ch 7, biological soft tissue. In W.N. Sharpe, editor, *Springer Handbook of Experimental Solid Mechanics*. Springer Science+Business Media, LLC New York, 2008.

[90] T. Ikeno and T. Kajishima. Finite-difference immersed boundary method consistent with wall conditions for incompressible turbulent flow simulations. *Journal of Computational Physics*, 226:1485–1508, 2007.

[91] A. Iserles. *A First Course in the Numerical Analysis of Differential Equations*. Cambridge University Press, 2003.

[92] D. Ishihara and S. Yoshimura. A monolithic approach for interaction of incompressible viscous fluid and an elastic body based on fluid pressure poisson equation. *International Journal for Numerical Methods in Engineering*, 64:167–203, 2005.

[93] Jr. J.E. Moore, C. Xu, S. Glagov, C.K. Zarins, and D.N. Ku. Fluid wall shear stress measurements in a model of the human abdominal aorta: Oscillatory behaviour and relationship to atherosclerosis. *Atherosclerosis*, 110:225–240, 1994.

[94] L.D. Jou and S.A. Berger. Numerical simulation of the flow in the carotid bifurcation. *Theoretical and Computational Fluid Dynamics*, 10:239–248, 1998.

[95] E. Järvinen, P. Råback, M. Lyly, and J. Salenius. A method for partitioned fluid-structure interaction computation of flow in arteries. *Medical Engineering & Physics*, 30:917–923, 2008.

[96] J. Jung, R.W. Lyczkowski, C.B. Panchal, and A. Hassanein. Multiphase hemodynamic simulation of pulsatile flow in a coronary artery. *Journal of Biomechanics*, 39:2064–2073, 2006.

[97] R. Kamakoti and W. Shyy. Fluid-structure interaction for aeroelastic applications. *Progress in Aerospace Sciences*, 40:535–558, 2004.

[98] D. Kim and H. Choi. Immersed boundary method for flow around an arbitrarily moving body. *Journal of Computational Physics*, 212:662–680, 2006.

[99] J. Kim, D. Kim, and H. Choi. An immersed-boundary finite-volume method for simulation of flow in complex geometries. *Journal of Computational Physics*, 171:132–150, 2001.

[100] S. Kirpekar and D.B. Bogy. Computing the aeroelastic disk vibrations in a hard disk drive. *Journal of Fluids and Structures*, 24:75–95, 2008.

[101] S.A. Kock, J.V. Nygaard, N. Eldrup, E. Fründ, A. Klærke, W.P. Paaske, E. Falk, and Y. Kim. Mechanical stresses in carotid plaques using mri-based fluid-structure interaction models. *Journal of Biomechanics*, 41:1651–1658, 2008.

[102] Y. Komai and K. Tanishita. Fully developed intermittent flow in a curved tube. *Journal of Fluid Mechanics*, 347:263–287, 1997.

[103] D.N. Ku. Blood flow in arteries. *Annual Review of Fluid Mechanics*, 29:399–434, 1997.

[104] D.N. Ku, D.P. Giddens, C.K. Zarins, and S. Glagov. Pulsatile flow and atherosclerosis in the human carotid bifurcation. positive correlation between plaque location and low and oscillating shear stress. *Arteriosclerosis, Thrombosis, and Vascular Biology*, 5:293–302, 1985.

[105] B.R. Kwak, P. Silacci, N. Stergiopulos, D. Hayoz, and P. Meda. Shear stress and cyclic circumferential stretch, but not pressure, alter connexin43 expression in endothelial cells. *Cell Communication and Adhesion*, 12:261–270, 2005.

[106] W.M. Lai, D. Rubin, and E. Krempl. *Introduction to Continuum Mechanics*. Butterworth–Heinemann, third edition, 1999.

[107] D. Lee and J.J. Chiu. Intimal thickening under shear in a carotid bifurcation–a numerical study. *Journal of Biomechanics*, 29(1):1–11, 1996.

[108] P.J. Lefebvre. Further experiments on transition to turbulence in constant-acceleration pipe flow. *Journal of Fluids Engineering*, 113:223–227, 1991.

[109] J.R. Levick. *An Introduction to Cardiovascular Physiology.* Arnold, fourth edition, 2003.

[110] H.S. Lew and Y.C. Fung. Entry flow into blood vessels at arbitrary reynolds number. *Journal of Biomechanics*, 3:23–38, 1970.

[111] Z. Li and M. Lai. The immersed interface method for the navier-stokes equations with singular forces. *Journal of Computational Physics*, 171:822–842, 2001.

[112] J. Lighthill. *Waves in Fluids.* Cambridge University Press, 1978.

[113] M.J. Lighthill. Physiological fluid dynamics: A survey. *Journal of Fluid Mechanics*, 52:475–497, 1972.

[114] F. Lindgärde, T. Thulin, and J. Östergren. *Kärlsjukdomar.* Studentlitteratur, 2006.

[115] M.N. Linnick and H.F. Fasel. A high-order immersed interface method for simulating unsteady incompressible flows in irregular domains. *Journal of Computational Physics*, 204:157–192, 2005.

[116] Y. Liu, Y. Lai, A. Nagaraj, B. Kane, A. Hamilton, R. Greene, D.D. McPherson, and K.B. Chandran. Pulsatile flow simulation in arterial vascular segments with intravascular ultrasound images. *Medical Engineering & Physics*, 23:583–595, 2001.

[117] C.R. Lodahl, B.M. Sumer, and J. Fredsœ. Turbulent combined oscillatory flow and current in a pipe. *Journal of Fluid Mechanics*, 373:313–348, 1998.

[118] R.J. Lutz, J.N. Cannon, K.B. Bischoff, R.L. Dedrick, R.K. Stiles, and D.L. Fry. Wall shear stress distribution in a model canine artery during steady flow. *Circulation Research*, 41:391–399, 1977.

[119] W.H. Lyne. Unsteady viscous flow in a curved pipe. *Journal of Fluid Mechanics*, 45:13–32, 1971.

[120] Rosenfeld M., Avrahami I., and Einav S. Unsteady effects on the flow across tilting disc valves. *Journal of Biomechanical Engineering*, 124:21–29, 2002.

[121] Jr. M.A. Gimbrone, J.N. Topper, T. Nagel, K.R. Anderson, and G. Garcia-Cardena. Endothelial dysfunction, hemodynamic forces, and atherogenesis. *Annals of the New York Academy of Sciences*, 902:230–240, 2000.

[122] H.G. Matthies and J. Steindorf. Partitioned strong coupling algorithms for fluid-structure interaction. *Computers and Structures*, 81:805–812, 2003.

[123] D.A. McDonald. *Blood Flow in Arteries*. Edward Arnold, 1960.

[124] R. Melchionna, D. Porcelli, A. Mangoni, D. Carlini, G. Liuzzo, G. Spinetti, A. Antonini, M.C. Capogrossi, and M. Napolitano. Laminar shear stress inhibits cxcr4 expression on endothelial cells: Functional consequences for atherogenesis. *The FASEB Journal*, 19:629–631, 2005.

[125] J. Milei, J.C. Parodi, M. Ferreira, A. Barrone, D.R. Grana, and L. Matturri. Atherosclerotic plaque rupture and intraplaque hemorrhage do not correlate with symptoms in carotid artery stenosis. *Journal of Vascular Surgery*, 38:1241–1247, 2003.

[126] J. Mohd-Yusof. Combined immersed-boundary/b-spline methods for simulations of flow in complex geometries. *Center for Turbulence Research: Annual Research Briefs*, pages 317–327, 1997.

[127] M. Motomiya and T. Karino. Flow patterns in the human carotid artery bifurcation. *Stroke*, 15:50–56, 1984.

[128] K.R. Moyle, L. Antiga, and D.A. Steinman. Inlet conditions for image-based cfd models of the carotid bifurcation: is it reasonable to assume fully developed flow. *Journal of Biomechanical Engineering*, 128:371–379, 2006.

[129] R.M. Nerem, J.A. Rumberger, Jr. D.R. Gross, R.L. Hamlin, and G.L. Geiger. Hot-film anemometer velocity measurements of arterial blood flow in horses. *Circulation Research*, 34:193–203, 1974.

[130] R.M. Nerem and W.A. Seed. An in vivo study of aortic flow disturbances. *Cardiovascular Research*, 6:1–14, 1972.

[131] R.M. Nerem, W.A. Seed, and N.B. Wood. An experimental study of the velocity distribution and transition to turbulence in the aorta. *Journal of Fluid Mechanics*, 52(1):137–160, 1972.

[132] F.H. Netter. *Atlas of Human Anatomy*. CIBA-GEIGY Corporation, Ardsley, USA, 1989.

[133] W.W. Nichols and M.F. O'Rourke. *McDonald's Blood Flow in Arteries: Theoretical Experimental and Clinical Principles*. Hodder Arnold, fifth edition, 2005.

[134] L.B. Nielsen. Transfer of low density lipoprotein into the arterial wall and risk of atherosclerosis. *Atherosclerosis*, 123:1–15, 1996.

[135] N.M. Nikolaidis and D.S. Mathioulakis. Axial and secondary flow study in a 90 deg bifurcation under pulsating conditions using piv. *Journal of Fluids Engineering*, 124:505–511, 2002.

[136] S. O'Callaghan, M. Walsh, and T. McGloughlin. Numerical modelling of newtonian and non-newtonian representation of blood in a distal end-to-side vascular bypass graft anastomosis. *Medical Engineering and Physics*, 28:70–74, 2006.

[137] H.N. Oscuii, M.T. Shadpour, and F. Ghalichi. Flow characteristics in elastic arteries using a fluid-structure interaction model. *American Journal of Applied Sciences*, 4(8):516–524, 2007.

[138] N. Ottosen and H. Petersson. *Introduction to the Finite Element Method*. Prentice Hall Europe, 1992.

[139] T.J. Pedley. Pulmonary fluid dynamics. *Annual Review of Fluid Mechanics*, 9:229–274, 1977.

[140] T.J. Pedley. *The Fluid Mechanics of Large Blood Vessels*. Cambridge, 1980.

[141] C. Pellieux, A. Desgeorges, C.H. Pigeon, C. Chambaz, H. Yin, D. Hayoz, and P. Silacci. Cap g, a gelsolin family protein modulating protective effects of unidirectional shear stress. *The Journal of Biological Chemistry*, 278(31):29136–29144, 2003.

[142] K. Perktold and G. Rappitsch. Computer simulation of local blood flow and vessel mechanics in a compliant carotid artery bifurcation model. *Journal of Biomechanics*, 28(7):845–856, 1995.

[143] C.S. Peskin. Numerical analysis of blood flow in the heart. *Journal of Computational Physics*, 25:220–252, 1977.

[144] S. Piperno, C. Farhat, and B. Larrouturou. Partitioned procedures for the transient solution of coupled aeroelastic problems. part i: Model problem, theory and two-dimensional application. *Computer Methods in Applied Mechanics and Engineering*, 124:79–112, 1995.

[145] I.V. Pivkin, P.D. Richardson, D.H. Laidlaw, and G.E. Karniadakis. Combined effects of pulsatile flow and dynamic curvature on wall shear stress in a coronary artery bifurcation model. *Journal of Biomechanics*, 38:1283–1290, 2005.

[146] G.E. Plante. Depression and cardiovascular disease: A reciprocal relationship. *Metabolism Clinical and Experimental*, 54(1):45–48, 2005.

[147] J.L.M. Poiseuille. Recherches experimentales sur le mouvement des liquides dans les tubes de tres petits diametres. *Comtes Rendus*, 11:961–967,1041–1048, 1840.

[148] J.L.M. Poiseuille. Recherches experimentales sur le mouvement des liquides dans les tubes de tres petits diametres. *Comtes Rendus*, 12:112–115, 1841.

[149] S.B. Pope. *Turbulent Flows*. Cambridge University Press, 2001.

[150] M.M. Rai and P. Moin. Direct simulation of turbulent flow using finite difference schemes. *Journal of Computational Physics*, 96:15–53, 1991.

[151] A. Ramgard. *Vektoranalys*. Teknisk högskolelitteratur, Stockholm AB, third edition, 2000.

[152] S.S. Rao. *The Finite Element Method in Engineering*. Butterworth-Heinemann, third edition, 1999.

[153] J. Revstedt. A virtual boundary method with improved computational efficiency using a multi-grid method. *International Journal for Numerical Methods in Fluids*, 45:775–795, 2004.

[154] J. Revstedt and L. Fuchs. Handling complex boundaries on a cartesian grid using surface singularities. *International Journal for Numerical Methods in Fluids*, 35:125–150, 2001.

[155] O. Reynolds. An experimental investigation of the circumstances which determine whether the motion of water shall be direct or sinuous, and the law of resistance in parallel channels. *Philosphical Transactions of the Royal Society of London, Ser. A*, 174:935–982, 1883.

[156] O. Reynolds. On the dynamical theory of incompressible viscous fluids and the determination of the criterion. *Philosphical Transactions of the Royal Society of London, Ser. A*, 186:123–164, 1895.

[157] P.D. Richardson, M.J. Davies, and G.V.R. Born. Influence of plaque configuration and stress distribution on fissuring of coronary atherosclerotic plaques. *The Lancet*, 334:941–944, 1989.

[158] C.C.M. Rindt, A.A. van Steenhoven, J.D. Janssen, and G. Vossers. Unsteady entrance flow in a 90^o curved tube. *Journal of Fluid Mechanics*, 226:445–474, 1991.

[159] R. Ross. The pathogenesis of atherosclerosis: a perspective for the 1990s. *Nature*, 362:801–809, 1993.

[160] R. Ross. Atherosclerosis – an inflammatory disease. *The New England Journal of Medicine*, 340(2):115–126, 1999.

[161] P.G. Saffmann. On the motion of small spheroidal particles in a viscous liquid. *Journal of Fluid Mechanics*, 1:540–553, 1956.

[162] P.G. Saffmann. The lift on a small sphere in a slow shear flow. *Journal of Fluid Mechanics*, 22(2):385–400, 1965.

[163] E.M. Saiki and S. Biringen. Numerical simulation of a cylinder in uniform flow: Application of a virtual boundary method. *Journal of Computational Physics*, 123:450–465, 1996.

[164] A. Samagaio and N.S. Vlachos. Calculation of three-dimensional laminar flows in t-shaped junctions. *Computer Methods in Applied Mechanics and Engineering*, 75:393–407, 1989.

[165] T. Sarpkaya. Experimental determination of the critical reynolds number for pulsating poiseuille flow. *ASME Journal of Basic Engineering*, 88:589–598, 1966.

[166] D. Schinas and D.S. Mathioulakis. Pulsating flow in a 90 degree bifurcation. *Journal of Fluids Engineering*, 122:569–575, 2000.

[167] H. Schlichting. *Boundary-Layer Theory.* McGraw-Hill, seventh edition, 1979.

[168] J.H. Siggers and S.L. Waters. Unsteady flows in pipes with finite curvature. *Journal of Fluid Mechanics*, 600:133–165, 2008.

[169] A.L.F.L.E. Silva, A. Silveira-Neto, and J.J.R. Damasceno. Numerical simulation of two-dimensional flows over a circular cylinder using the immersed boundary method. *Journal of Computational Physics*, 189:351–370, 2003.

[170] F.T. Smith. Pulsatile flow in curved pipes. *Journal of Fluid Mechanics*, 71:15–42, 1975.

[171] B. Snyder, J.R. Hammersley, and D.E. Olson. The axial skew of flow in curved pipes. *Journal of Fluid Mechanics*, 161:281–294, 1985.

[172] J.V. Soulis, T.M. Farmakis, G.D. Giannoglou, and G.E. Louridas. Wall shear stress in normal left coronary artery tree. *Journal of Biomechanics*, 39:742–749, 2006.

[173] H.C. Stary, D.H. Blankenhorn, A.B. Chandler, S. Glagov, Jr. W. Insull, M. Richardson, M.E. Rosenfeld, S.A. Schaffer, C.J. Schwartz, and W.D. Wagner. A definition of the intima of human arteries and of its atherosclerosis-prone regions. a report from the commitee on vascular lesions of the council on arteriosclerosis, american heart association. *Circulation*, 85:391–405, 1992.

[174] H.C. Stary, A.B. Chandler, S. Glagov, J.R. Guyton, Jr. W. Insull, M.E. Rosenfeld, S.A. Schaffer, C.J. Schwartz, W.D. Wagner, and R.W. Wissler. A definition of initial, fatty streak, and intermediate lesions of atherosclerosis. a report from the commitee on vascular lesions of the council on atherosclerosis, american heart association. *Circulation*, 89:2462–2478, 1994.

[175] G.G. Stokes. On the theories of the internal friction of fluids in motion, and of the equilibrium and motion of elastic solids. *Transaction of Cambride Philosophical Society*, 8:287–305, 1845.

[176] K. Sudo, M. Sumida, and R. Yamane. Secondary motion of fully developed oscillatory flow in a curved pipe. *Journal of Fluid Mechanics*, 237:189–208, 1992.

[177] B. Sundström, editor. *Handbok och Formelsamling i Hållfasthetslära.* Institutionen för Hållfasthetslära KTH, Stockholm, 1998.

[178] S.P. Sutera. The history of poiseuille's law. *Annual Review of Fluid Mechanics*, 25:1–19, 1993.

[179] A. Svärdström. *Signaler och System.* Studentlitteratur AB, 1999.

[180] S. Tada, S. Oshima, and R. Yamane. Classification of pulsating flow patterns in curved pipes. *Journal of Biomechanical Engineering*, 118:311–317, 1996.

[181] M. Tadjfar. Flow in arterial branch model. *Journal of Engineering Mathematics*, 54:359–374, 2006.

[182] L. Talbot and K.O. Gong. Pulsatile entrance flow in a curved pipe. *Journal of Fluid Mechanics*, 127:1–26, 1983.

[183] J.C. Tannehill, D.A. Anderson, and R.H. Pletcher. *Computational Fluid Mechanics and Heat Transfer.* Taylor & Francis, second edition, 1997.

[184] J.M. Tarbell. Mass transport in arteries and the localization of atherosclerosis. *Annual Review of Biomedical Engineering*, 5:79–118, 2003.

[185] C.A. Taylor and M.T. Draney. Experimental and computational methods in cardiovascular fluid mechanics. *Annual Review of Fluid Mechanics*, 36:197–231, 2004.

[186] G.I. Taylor. The criterion for turbulence in curved pipes. *Proceedings of the Royal Society of London. Series A.*, 124(794):243–249, 1929.

[187] M. Texon. A hemodynamic concept of atherosclerosis, with particular reference to coronary occlusion. *Archives of Internal Medicine*, 99:418–427, 1957.

[188] S. Timoshenko and S. Woinowsky-Krieger. *Theory of Plates and Shells*. McGraw-Hill Book Company, Inc., second edition, 1959.

[189] G.J. Tortora and B. Derrickson. *Principles of Anatomy and Physilogy*. John Wiley & Sons Inc., eleventh edition, 2006.

[190] Y. Tseng and J.H. Ferziger. A ghost-cell immersed boundary method for flow in complex geometry. *Journal of Computational Physics*, 192:593–623, 2003.

[191] J.Y. Tu and L. Fuchs. Overlapping grids and multigrid methods for three-dimensional unsteady flow calculations in ic engines. *International Journal for Numerical Methods in Fluids*, 15:693–714, 1992.

[192] R. Tuzi and P. Blondeaux. Intermittent turbulence in a pulsating pipe flow. *Journal of Fluid Mechanics*, 599:51–79, 2008.

[193] A. Valencia and M. Villanueva. Unsteady flow and mass transfer in models of stenotic arteries considering fluid-structure interaction. *International Communications in Heat and Mass Transfer*, 33:966–975, 2006.

[194] R. van Loon, P.D. Anderson, F.N. van de Vosse, and S.J. Sherwin. Comparison of various fluid-structure interaction methods for deformable bodies. *Computers and Structures*, 85:833–843, 2007.

[195] J. Vierendeels, K. Dumont, and P.R. Verdonck. A partitioned strongly coupled fluid-structure interaction method to model heart valve dynamics. *Journal of Computational and Applied Mathematics*, 215:602–609, 2008.

[196] J.R. Vinson. *The Behavior of Thin Walled Structures: Beams, Plates, and Shells*. Kluwer Academic Publishers, 1989.

[197] P.E.J. Vos, R. van Loon, and S.J. Sherwin. A comparison of fictitious domain methods appropriate for spectral/hp element discretisations. *Computer Methods in Applied Mechanics and Engineering*, 197:2275–2289, 2008.

[198] X. Wang and W.K. Liu. Extended immersed boundary method using fem and rkpm. *Computer Methods in Applied Mechanics and Engineering*, 193:1305–1321, 2004.

[199] A.J. Ward-Smith. *Internal Fluid Flow*. Oxford University Press, New York, 1980.

[200] H. Wayland. Rheology and the microcirculation. *Gastroenterology*, 52(2):342–355, 1967.

[201] J.J. Wentzel, F.J.H. Gijsen, J.C.H. Schuurbiers, R. Krams, P.W. Serruys, P.J. De Feyter, and C.J. Slager. Geometry guided data averaging enables the interpretation of shear stress related plaque development in human coronary arteries. *Journal of Biomechanics*, 38:1551–1555, 2005.

[202] C.M. White. Streamline flow through curved pipes. *Proceedings of the Royal Society of London. Series A.*, 123(792):645–663, 1929.

[203] F.M. White. *Fluid Mechanics*. McGraw-Hill, fifth edition, 2003.

[204] F.M. White. *Viscous Fluid Flow*. McGraw-Hill, third edition, 2006.

[205] R.W. Wissler, J.P. Strong, and PDAY Research Group. Risk factors and progression of atherosclerosis in youth. *American Journal of Pathology*, 153(4):1023–1033, 1998.

[206] J.R. Womersley. Method for the calculation of velocity, rate of flow and viscous drag in arteries when the pressure gradient is known. *Journal of Physiology*, 127:553–563, 1955.

[207] C. Wood, A.J. Gil, O. Hassan, and J. Bonet. A partitioned coupling approach for dynamic fluid-structure interaction with applications to biological membranes. *International Journal for Numerical Methods in Fluids*, 57:555–581, 2008.

[208] D.M. Wootton and D.N. Ku. Fluid mechanics of vascular systems, diseases, and thrombosis. *Annual Review of Biomedical Engineering*, 1:299–329, 1999.

[209] E.L. Yellin. Laminar-turbulent transition process in pulsatile flow. *Circulation Research*, 19:791–804, 1966.

[210] A.P. Yoganathan, K.B. Chandran, and F. Sotiropoulos. Flow in prosthetic heart valves: State-of-the-art and future directions. *Annals of Biomedical Engineering*, 33(12):1689–1694, 2005.

[211] Z. Yu. A DLM/FD method for fluid/flexible-body interactions. *Journal of Computational Physics*, 207:1–27, 2005.

[212] M. Zamir. *The Physics of Pulsatile Flow*. Springer-Verlag, New York, Inc., 2000.

[213] C.K. Zarins, D.P. Giddens, B.K. Bharadvaj, V.S. Sottiurai, R.F. Mabon, and S. Glagov. Carotid bifurcation atherosclerosis. quantitative correlation of plaque localization with flow velocity profile and wall shear stress. *Circulation Research*, 53:502–514, 1983.

[214] C.H. Zhang, Y. Liu, R.M.C. So, and N. Phan-Thien. The influence of inlet velocity profile on three-dimensional three-generation bifurcating flows. *Computational Mechanics*, 29:422–429, 2002.

[215] J. Zhang, B. Gellman, A. Koert, K.A. Dasse, R.J. Gilbert, B.P. Griffith, and Z.J. Wu. Computational and experimental evulation of the fluid dynamics and hemocompatibility of the centrimag blood pump. *Artificial Organs*, 30(3):168–177, 2006.

[216] J. Zhang, G.L. Niebur, and T.C. Ovaert. Mechanical property determination of bone through nano- and micro-indentation testing and finite element simulation. *Journal of Biomechanics*, 41:267–275, 2008.

[217] L. Zhang, A. Gerstenberger, X. Wang, and W.K. Liu. Immersed finite element method. *Computer Methods in Applied Mechanics and Engineering*, 193:2051–2067, 2004.

[218] Q. Zhang and T. Hisada. Studies of the strong coupling and weak coupling methods in fsi analysis. *International Journal for Numerical Methods in Engineering*, 60:2013–2029, 2004.

[219] Z. Zhang, C. Kleinstreuer, and C.S. Kim. Effects of curved inlet tubes on air flow and particle deposition in bifurcating lung models. *Journal of Biomechanics*, 34:659–669, 2001.

[220] H. Zhao, J.B. Freund, and R.D. Moser. A fixed-mesh method for incompressible flow-structure systems with finite solid deformations. *Journal of Computational Physics*, 227:3114–3140, 2008.